STRUCTURE-PROPERTY RELATIONSHIPS IN INDIUM AND ZINC BASED OXIDES FOR TRANSPARENT CONDUCTIVE AND PHOTOCATALYTIC APPLICATIONS

Arreerat Jiamprasertboon

A Thesis Submitted in Partial Fulfillment of the Requirements for the

Degree of Doctor of Philosophy in Chemistry

Suranaree University of Technology

Academic Year 2017

ความสัมพันธ์ระหว่างโครงสร้างและสมบัติของสารประกอบออกไซด์ของอินเดียมและซิงค์สำหรับการประยุกต์ใช้เป็นตัวนำไฟฟ้าโปร่งใสและตัวเร่งปฏิกิริยาเชิงแสง

นางสาวอารีรัตน์ เจียมประเสริฐบุญ

วิทยานิพนธ์นี้เป็นส่วนหนึ่งของการศึกษาตามหลักสูตรปริญญาวิทยาศาสตรดุษฎีบัณฑิต
สาขาวิชาเคมี
มหาวิทยาลัยเทคโนโลยีสุรนารี
ปีการศึกษา 2560

STRUCTURE-PROPERTY RELATIONSHIPS IN INDIUM AND ZINC BASED OXIDES FOR TRANSPARENT CONDUCTIVE AND PHOTOCATALYTIC APPLICATIONS

Suranaree University of Technology has approved this thesis submitted in partial fulfillment of the requirements for the Degree of Doctor of Philosophy.

Thesis Examining Committee

(Prof. Dr. James R.Ketudat-Cairns)

Chairperson

Theeranun Siritanon

(Asst. Prof. Dr. Theeranun Siritanon)

Member (Thesis Advisor)

(Prof. Dr. Jatuporn Wittayakun)

Member

Rapee Utke

(Assoc. Prof. Dr. Rapee Utke)

Member

Narong Chanlek

(Dr. Narong Chanlek)

Member

(Prof. Dr. Santi Maensiri)
Vice Rector for Academic Affairs
and Internationalization

(Asst. Prof. Dr. Worawat Meevasana)
Dean of Institute of Science

อารีรัตน์ เจียมประเสริฐบุญ : ความสัมพันธ์ระหว่างโครงสร้างและสมบัติของสารประกอบออกไซด์ของอินเดียมและซิงค์สำหรับการประยุกต์ใช้เป็นตัวนำไฟฟ้าโปร่งใสและ ตัวเร่งปฏิกิริยาเชิงแสง (STRUCTURE-PROPERTY RELATIONSHIPS IN INDIUM AND ZINC BASED OXIDES FOR TRANSPARENT CONDUCTIVE AND PHOTOCATALYTIC APPLICATIONS) อาจารย์ที่ปรึกษา : ผู้ช่วยศาสตราจารย์ ดร.ธีรนันท์ ศิริตานนท์, 162 หน้า.

วิทยานิพนธ์เล่มนี้มุ่งศึกษาความสัมพันธ์ระหว่างโครงสร้างและสมบัติในสารประกอบออกไซด์ของอินเดียมและซิงค์ โดยศึกษาสารประกอบสามกลุ่ม ได้แก่ สารประกอบอินเดียมเทลลูเลตที่เจือด้วย แกลเลียม บิสมัท และแลนทานัม สารประกอบอินเดียมสแทนเนตที่เจือด้วยไนโอเบียมและแทนทาลัม และสารประกอบซิงค์ออกไซด์ที่เจือด้วยคลอรีน

สารประกอบอินเดียมเทลลูเลตที่เจือด้วยแกลเลียม (Ga$^{3+}_{0-0.4}$) บิสมัท (Bi$^{3+}_{0-0.5}$) และแลนทานัม (La$^{3+}_{0-0.2}$) ได้ถูกสังเคราะห์โดยปฏิกิริยาสถานะของแข็ง ถึงแม้ว่าการแทนที่อินเดียม ด้วยแกลเลียม บิสมัท และแลนทานัม จะไม่สามารถปรับปรุงความนำไฟฟ้าของสาร ให้ดีขึ้นได้ แต่การศึกษาอย่างละเอียดในที่นี้ทำให้เกิดความเข้าใจเกี่ยวกับโครงสร้างผลึก โครงสร้างอิเล็กทรอนิกส์และสมบัติเชิงแสงของสาร ข้อมูลเชิงผลึก ได้แก่ ความยาวพันธะและมุมพันธะบ่งชี้ว่า ไม่มีการบิดเบี้ยวอย่างมีนัยสำคัญของรูปทรงแปดหน้า (M-O$_6$) สำหรับทุกตัวอย่างที่มี การแทนที่ อย่างไรก็ตาม คู่อิเล็กตรอนโดดเดี่ยวในออบิทัล 6s^2 ที่มีความเป็นสเตอริโอแอคทีฟในบิสมัท ทำให้ไอออนบวกอินเดียมหรือบิสมัทในทรงแปดหน้า (In/Bi-O$_6$) เลื่อนไปยังขอบด้านหนึ่งของ ทรงแปดหน้าการคำนวณโครงสร้างอิเล็กทรอนิกส์ แสดงให้เห็นชัดเจนว่าช่องว่างระหว่างแถบ พลังงานพื้นฐานของทุกตัวอย่าง มีต้นกำเนิดมาจากการเปลี่ยนแปลงแบบไดเร็กอะลาวทรานสิชัน เป็นที่น่าสนใจอย่างมากกว่าบิสมัทมีอิทธิพลอย่างมากต่อการกระจายตัวของแถบตัวนำ และระดับ ออบิทัล 6s ของบิสมัทได้มีส่วนร่วมเพิ่มเติมที่แถบเวเลนซ์สูงสุด ในขณะที่แถบเวเลนซ์ของ ตัวอย่างที่เจือด้วยไอออนบวกอื่น และที่ไม่มีการเจือมีลักษณะของออบิทัลพีของออกซิเจน (O 2p) และออบิทัลดีของอินเดียม (In 4d) เป็นหลัก

สารปะกอบอินเดียมสแทนเนตที่เจือด้วยไนโอเบียม (Nb$^{5+}_{0.5}$) และแทนทาลัม (Ta$^{5+}_{0.5}$) ได้ถูกสังเคราะห์โดยปฏิกิริยาสถานะของแข็ง การแทนที่ของไนโอเบียม/แทนทาลัมเพิ่มอัตราส่วนโมลของอินเดียม/ทิน และดังนั้นจึงขยายพารามิเตอร์เซลล์ อีกทั้งค่า ความต้านทานไฟฟ้าที่ได้ สูงกว่าสารประกอบที่ไม่มีการเจือ การศึกษาเชิงคำนวณบ่งชี้ว่าการเจือไม่ส่งผลต่อโครงสร้างอิเล็กทรอนิกส์อย่างมีนัยสำคัญ ถึงแม้ว่าความสามารถในการเคลื่อนที่ของตัวนำจะต่ำลงเล็กน้อยเมื่อ พิจารณาผลการศึกษาทั้งจากการทดลองและการคำนวณ จึงเสนอกลไกในการนำไฟฟ้าของสารประกอบกลุ่มนี้ว่าเกิดจากช่องว่างของออกซิเจนซึ่งทำให้เกิดตัวนำไฟฟ้าเพิ่มขึ้นในสาร

ฟิล์มบางซิงค์ออกไซด์ที่เจือด้วยคลอรีน 0-15 เปอร์เซ็นต์โมลได้ถูกสังเคราะห์โดยการสะสมไอเคมีที่มีละอองลอยเป็นตัวช่วย การเจือด้วยคลอรีนมีผลกระทบอย่างมีนัยสำคัญต่อ สัณฐานวิทยาของฟิล์มที่ได้ และส่งผลให้มีการปรับปรุงค่าความส่องผ่านแสงขาว และลดค่าความต้านทานไฟฟ้า เมื่อ 7 เปอร์เซ็นต์โมลของเฟอริกคลอไรด์ ($FeCl_3$) ถูกใช้ พบว่าได้ค่า ความส่องผ่าน (%T) 85% และค่าความต้านทานไฟฟ้าของฟิล์มในระดับ 10^{-2} Ω.cm สมบัติ การทำความสะอาดตัวเองซึ่งถูกศึกษาโดยใช้การสลายตัวเมื่อถูกเร่งปฏิกิริยาเชิงแสงของกรดสเตียริก ภายใต้แสงยูวีเอมีค่าสูงสุดด้วยค่าประสิทธิภาพควอนตัม (FQE) สูงสุดเท่ากับ $3.0 \pm 0.1 \times 10^{-4}$ โมเลกุล/โฟตอน เมื่อใช้ 10 เปอร์เซ็นต์โมลของเฟอริกคลอไรด์ ($FeCl_3$)

สาขาวิชาเคมี
ปีการศึกษา 2560

ลายมือชื่อนักศึกษา อรีรัตน์ เสี่ยมประเสริฐบุญ
ลายมือชื่ออาจารย์ที่ปรึกษา ธีรนันท์ ศิริตานนท์

ARREERAT JIAMPRASERTBOON : STRUCTURE-PROPERTY
RELATIONSHIPS IN INDIUM AND ZINC BASED OXIDES FOR
TRANSPARENT CONDUCTIVE AND PHOTOCATALYTIC APPLICATIONS.
THESIS ADVISOR : ASST. PROF. THEERANUN SIRITANON, Ph.D. 162 PP.

OXIDES/STRUCTURE-PROPERTY RELATIONSHIPS/TRANSPARENT CONDUCTING OXIDES/PHOTOCATALYST

This thesis focuses on structure-property relationships in indium and zinc-based oxides, including (Ga, Bi and La)-doped In_2TeO_6, (Nb and Ta)-doped $In_4Sn_3O_{12}$ and Cl-doped ZnO for applications in transparent conductors and photocatalysis.

$In_{2-x}M_xTeO_6$ (M = $Ga^{3+}_{0-0.4}$, $Bi^{3+}_{0-0.5}$ and $La^{3+}_{0-0.2}$) were successfully synthesised by solid state reactions. While substituting In with Bi^{3+}, Ga^{3+} and La^{3+} fails to improve the electronic conductivity of In_2TeO_6, detailed investigations have led to more understanding on crystal structure, electronic structure and optical properties of the compound. Crystallographic data, including bond lengths and bond angles, suggest no significant distortion of M-O_6 octahedra for all doped samples; however, the stereoactive $6s^2$ lone-pair electrons in Bi cause the In/Bi cation in In/Bi-O_6 octahedra to shift toward one edge of the octahedra. The band structure calculation clarified that the fundamental band gap energies of all samples originate from the direct allowed transition. Interestingly, Bi greatly influences the conduction band dispersion and Bi 6s state additionally contributes at the valence band maximum, while the valence band of other M-doped and un-doped samples are mainly O 2p and In 4d in character.

$In_{4+x}Sn_{3-2x}M_xO_{12}$) M_x = $Nb^{5+}_{0.5}$ and $Ta^{5+}_{0.5}$ (were also successfully synthesised by

solid state reactions. The substitution of Nb/Ta increases the In/Sn mol ratio and thus enlarges the cell parameters. The obtained electrical resistivities are higherin doped samples. Band structure calculations suggest that the substitution does not significantly affect the electronic structure, though the carrier mobility is slightly reduced. Based on both experimental and computational results, it is proposed that the origin of conduction in this system is the presence of oxygen vacancies which create extra charge carriers.

$Zn_{1-x}Cl_xO$ ($x = 0$-0.15) thin films were synthesised by aerosol assisted chemical vapour deposition. Cl doping has significant effects on the morphology of the obtained films and results in an improvement in the visible light transmission and lower electrical resistivities. The transmittance (%T) of 85% with the typical resistivities in the order of 10^{-2} Ω.cm was obtained when 7 mol% $FeCl_3$ was used. The self-cleaning properties determined by using the photocatalytic degradation of stearic acid under UVA irradiation were maximised with the highest formal quantum efficiency (FQE) of $3.0 \pm 0.1 \times 10^{-4}$ molecule/photon by the use of 10 mol% $FeCl_3$.

School of Chemistry Student's Signature อภิรัตน์ เจียมประเสริฐบุญ

Academic Year 2017 Advisor's Signature ธีรนันท์ ศิริตานนท์

ACKNOWLEDGEMENTS

I believe I have learned and experienced many things as a Ph.D. student. In that regard, I would like to express my sincere thanks to many people who help me complete my thesis, thereby allowing me to reach my goal achieving a Ph.D.

Asst. Prof. Dr. Theeranun Siritanon is acknowledged as a wonderful advisor. She was kindly advising and helping me along with my thesis. Under her supervision, I feel like I'm a bird that can fly with freedom, as she guided me in the direction but did not controls my wings. So, I never called her as a boss; I believe she is a real advisor and a good model. I am always happy making a scientific discussion as well as all stories with her. Her encouragement and support are greatly appreciated. I'm actually not the best student, but I got much improved and felt so proud of this under her supervision. I like the way she thinks: reasonable and positive. I believe the way she treated a student was like watering and giving fertilizer to be a beautiful flower. Moreover, she is well known as a kind person for everyone, not only with me. Due to all of the above, I feel like she is an angel and I'm blissful working with her.

Prof. Claire J. Carmalt is acknowledged as a marvelous advisor during my study at the Department of Chemistry, University College London (UCL), England. I would like to thank Asst. Prof. Dr. Theeranun again for giving me the chance to work with her. It was my fortune and honor to have a great opportunity in my life. I found what I love to do. I am always blessed working with her; discussion and sharing research experience with her were fantastic. I also appreciate her kindness and support. Moreover, I found I fell in love with English culture. I will adopt it to improve myself and suggest to others.

I am grateful to colleagues in both solid state chemistry research group at SUT and materials chemistry research group at UCL: Anurak Waehayee, Prapaiporn Pornsuksawang, Sebastian C. Dixon, Yao Lu, Sanjayan Sathasivam, etc. Their assistance and friendship were really precious. I love spending time with them. I also would like to thank people from the School of Chemistry, the School of Physics, the Center for Scientific and Technological Equipment (CSTE) and the Synchrotron Light Research Institute (SLRI). With their help and support, my working became smoother.

I am thankful to Dr. Suwit Suthirakul, Mr. Thanundorn Kongnok and Assoc. Prof. Dr. Sirichok Jungthawan for their valuable time on the calculations for my work and kind suggestions. I would like to acknowledge Dr. Xiaodong Wang (Bruker, Singapore) and Assoc. Prof. Dr. Nonglak Meethong (Khon Kaen University) for their valuable guidance and discussion on structure refinement. I also would like to thank the thesis defense committee for their valuable time giving research suggestions and discussion.

Essentially, the Development and Promotion of Science and Technology Talent Project (DPST) is acknowledged for financial support and especially providing a variety of opportunities to become a good scientist.

Last, but not least, I cherish my family and Tanachat Eknapakul, for being beside me. Their endless love, unconditional encouragement and support are indeed invaluable.

Arreerat Jiamprasertboon

CONTENTS

Page

ABSTRACT IN THAI I

ABSTRACT IN ENGLISH III

ACKNOWLEDGEMENTS V

CONTENTS VII

LIST OF TABLES XI

LIST OF FIGURES XII

CHAPTER

I INTRODUCTION 1

1.1 Significant of the study 1

1.1.1 Transparent Conducting Oxides (TCOs)..1

1.1.2 Photocatalyst 2

1.2 Background of the study 3

1.2.1 Crystal structure 3

1.2.1.1 Structure containing stereochemically active

lone-pair electrons 3

1.2.1.2 Structure refinement 6

1.2.2 Optical properties 9

1.2.2.1 Interactions of UV-Visible light and solids.........................9

1.2.2.2 Luminescence spectroscopy 14

CONTENTS (Continued)

Page

1.2.3 Electrical properties and band structures..16

1.3 Transparent Conducting Oxides (TCOs) 22

1.4 Photocatalysis...24

1.5 Material syntheses 27

1.5.1 Solid State reaction..27

1.5.2 Aerosol Assisted Chemical Vapour Deposition (AACVD).............28

1.6 Scope and limitations of the study 30

1.7 References 31

II **LITERATURE REVIEWS**..41

2.1 In_2TeO_6-based oxides...41

2.2 $In_4Sn_3O_{12}$-based oxides 43

2.3 ZnO-based oxides 47

2.4 References...51

III **INVESTIGATION ON CRYSTAL STRUCTURES, OPTICAL PROPERTIES AND BAND STRUCTURE CALCULATIONS OF $In_{2-x}M_xTeO_6$ (M = Ga, Bi, La)** 57

3.1 Abstract 57

3.2 Introduction 58

3.3 Experimental 60

3.4 Results and discussion 62

CONTENTS (Continued)

Page

3.4.1 Crystal structure 62

3.4.2 Optical properties and band structure calculation 79

3.5 Conclusions 84

3.6 References 85

IV UNDERSTANDING STRUCTURES, OPTICAL AND ELECTRICAL PROPERTIES OF M-DOPED $In_4Sn_3O_{12}$ (M = Nb, Ta) 93

4.1 Abstract 93

4.2 Introduction 94

4.3 Experimental 95

4.4 Calculation details 96

4.5 Results and discussion 98

4.5.1 Crystal structure 98

4.5.2 Optical properties 105

4.5.3 Electrical properties 107

4.5.4 Calculation studies 108

4.6 Conclusions 111

4.7 References 112

V PHOTOCATALYTIC AND ELECTRICALLY CONDUCTIVE TRANSPARENT Cl-DOPED ZnO THIN FILMS *via* AEROSOL ASSISTED CHEMICAL VAPOUR DEPOSITION (AACVD) 118

CONTENTS (Continued)

Page

5.1 Abstract 118

5.2 Introduction 119

5.3 Experimental 122

5.3.1 Film synthesis 122

5.3.2 Film characterisations 123

5.4 Results and discussion 125

5.4.1 Film synthesis 125

5.4.2 Elemental analysis 126

5.4.3 Crystal structure 129

5.4.4 Surface morphology 131

5.4.5 Surface topology 133

5.4.6 Functional properties 134

5.4.6.1 Photocatalytic properties 134

5.4.6.2 Transparent conducting oxide (TCO) properties 135

5.5 Conclusions 141

5.6 References 142

VI CONCLUSION 153

APPENDICES 155

APPENDIX A XPS ANALYSIS OF Cl-DOPED ZnO FILMS 156

APPENDIX B STEARIC ACID DEGRADATION TEST 159

CURRICULUM VITAE 162

LIST OF TABLES

Table **Page**

3.1 Rietveld refinement parameters of $In_{2-x}Ga_xTeO_6$ (x = 0, 0.20, 0.40), $In_{2-x}Bi_xTeO_6$ (x = 0, 0.10, 0.30, 0.50) and $In_{2-x}La_xTeO_6$ (x = 0, 0.10, 0.20) 70

3.2 Crystallographic data of $In_{2-x}Ga_xTeO_6$ (x = 0, 0.20, 0.40), $In_{2-x}Bi_xTeO_6$ (x = 0, 0.10, 0.30, 0.50) and $In_{2-x}La_xTeO_6$ (x = 0, 0.10, 0.20)......................... 70

3.3 Bond lengths and average bond lengths of In-O and Te-O 71

4.1 Rietveld refinement parameters of $In_4Sn_3O_{12}$ and $In_{4+x}Sn_{3-2x}M_xO_{12}$ ($M_x = Nb_{0.5}, Ta_{0.5}$) 102

4.2 Crystallographic data of $In_4Sn_3O_{12}$ and $In_{4+x}Sn_{3-2x}M_xO_{12}$ ($M_x = Nb_{0.5}, Ta_{0.5}$) 103

4.3 Electrical resistivity of $In_4Sn_3O_{12}$ and $In_{4+x}Sn_{3-2x}M_xO_{12}$ ($M_x = Nb_{0.5}, Ta_{0.5}$) before and after N_2 annealing at 900 °C for 3 hours. 108

5.1 Cell parameters *a*, *c*, cell volume *V*, crystallite size and film thickness......... 131

5.2 Functional properties: photocatalytic properties and TCO properties, which includes electrical properties and optical properties 140

LIST OF FIGURES

Figure **Page**

1.1 The structure and cation environment of (a) β-SnWO$_4$ and (b) Scheelite PbWO$_4$, where the black spheres, the dark grey spheres and the light-grey spheres represent transition metal ions, oxygen ions and the p-block cations, respectively 6

1.2 Schematic diagram demonstrating the obtained sample and structural information relating to XRD data 7

1.3 The interactions between the incident light and solids 10

1.4 Absorption (a) and spontaneous emission (b) of light radiation 10

1.5 Diagram explaining the effect of Moss-Burstein shift in degenerately doped semiconductors 13

1.6 The corrected Tauc plot method for degenerately doped semiconductors. The band gap is obtained from the broadening parameter $\pi\Gamma/4$ added to the x axis 14

1.7 The energy level diagram coupled with absorption and emission spectra 15

1.8 The band structure of metals 16

1.9 The plots of conductivity vs. 1/T for metals, semiconductors and insulators ... 17

1.10 The band structures of (a) intrinsic and extrinsic semiconductors of (b) n-type and (c) p-type 18

LIST OF FIGURES (Continued)

Figure **Page**

1.11 The band structure of insulators 19

1.12 One-dimensional band structure resulted from bonding and antibonding of M-O 20

1.13 (a) The electronic band structure of RuO_2 (b) the first Brillouin zone for tetragonal rutile lattice of RuO_2 displaying different ***k***-space 21

1.14 The calculated density of states of RuO_2 for total contribution and from atomic orbitals contribution of Ru *4d* and O *2p* 21

1.15 Band gap types: (a) direct and (b) indirect 22

1.16 The simple band structures of (a) stoichiometric In_2O_3, (b) slightly doped In_2O_3 and (c) heavily doped In_2O_3 23

1.17 A schematic diagram of a photocatalytic process........ 25

1.18 The schematic diagram of Aerosol Assisted Chemical Vapour Deposition (AACVD) 30

2.1 (a) The structure of In_2TeO_6 where In^{3+} and Te^{6+} octahedra are represented in turquoise and black, respectively (b) Corner shared octahedral network of $In^{3+}O_6$........ 41

2.2 (a) The structure of M_7O_{12} when black and blue areas are octahedra and seven-fold unit, respectively (b) Shaded space represents octahedra and non-shaded one is seven-coordinated polyhedral 43

2.3 The calculated electronic band structure and (b) DOS of $In_4Sn_3O_{12}$........ 47

LIST OF FIGURES (Continued)

Figure **Page**

2.4 Crystal structures of ZnO: (a) hexagonal wurtzite, (b) cubic zinc blende and (c) cubic rocksalt ... 48

2.5 Band structure of ZnO calculated using HSE hybrid functional ... 49

2.6 The proposed photocatalytic mechanism by (a) a cation and (b) an anion dopant on ZnO surface ... 50

3.1 Crystal structure of ideal In_2TeO_6 ... 62

3.2 X-ray diffraction patterns of (a) $In_{2-x}Ga_xTeO_6$ (x = 0-0.40), (b) $In_{2-x}Bi_xTeO_6$ (x = 0-0.50) and (c) $In_{2-x}La_xTeO_6$ (x = 0-0.20) ... 63

3.3 Cell parameters *a*, *c* and cell volume of $In_{2-x}Ga_xTeO_6$ (red circle), $In_{2-x}Bi_xTeO_6$ (black square) and $In_{2-x}La_xTeO_6$ (blue triangle) ... 65

3.4 SEM image of $In_{1.90}Bi_{0.10}TeO_6$ ... 66

3.5 Rietveld refinement plots of (a) In_2TeO_6, (b) $In_{1.60}Ga_{0.40}TeO_6$, (c) $In_{1.50}Bi_{0.50}TeO_6$ and (d) $In_{1.80}La_{0.20}TeO_6$ ... 68

3.6 Schematic diagram of an $M\text{-}O_6$ octahedron for $In_{2-x}M_xTeO_6$ when M_x = $Ga_{0.40}$, $Bi_{0.50}$ and $La_{0.20}$ ... 73

3.7 (a) Normalized Bi M_5-edge XANES spectra and (b) Pre-edge region of Bi M_5-edge XANES spectra of $In_{2-x}Bi_xTeO_6$ (x = 0.06, 0.10, 0.30 and 0.50) ... 75

3.8 Normalized Te L_3-edge XANES spectra of $In_{2-x}Bi_xTeO_6$ (x = 0.06, 0.10, 0.30 and 0.50) ... 77

LIST OF FIGURES (Continued)

Figure **Page**

3.9 XPS spectra of (a) Bi $4f_{7/2}$, (b) Te $3d_{5/2}$ and (c) O 1*s* for $In_{2-x}Bi_xTeO_6$ series (x = 0.06, 0.10, 0.30 and 0.50) 78

3.10 Absorbance UV-Visible spectra (a) and Kubelka-Munk plots (b) of $In_{2-x}M_xTeO_6$ when $M_x = Ga_{0.2}$, $Ga_{0.4}$, $Bi_{0.1}$, $Bi_{0.3}$, $Bi_{0.5}$, $La_{0.1}$ and $La_{0.2}$ according to direct allowed transition 80

3.11 The calculated orbital-projected electronic structures of In_2TeO_6, $In_{1.58}TeO_6Ga_{0.42}$, $In_{1.75}TeO_6La_{0.25}$ and $In_{1.5}TeO_6Bi_{0.5}$ along Γ-M-K-Γ-A high symmetry directions. The *s, p and d*-band characters are indicated by red (black), blue (grey) and dark blue (dark grey), respectively. The thickness of bands indicates the spectral weight. The spectrum of $|\langle\psi_c|\nabla|\psi_v\rangle|^2$ (see text) for all compounds is shown next to corresponding band structure plot and their magnitudes are given in arbitrary units. The transition strength contributed to prominent peaks is highlighted by yellow (white) dot on the band structure plot 82

3.12 Photoluminescence spectra of $In_{2-x}M_xTeO_6$ ($M_x = Ga_{0.2}$, $Ga_{0.4}$, $Bi_{0.1}$, $Bi_{0.3}$, $Bi_{0.5}$, $La_{0.1}$ and $La_{0.2}$) 83

LIST OF FIGURES (Continued)

Figure **Page**

4.1 Unit cell of a) pure $In_4Sn_3O_{12}$ and b) metal (Nb, Ta) doped $In_4Sn_3O_{12}$. Pink, grey and red spheres represent In, Sn and O ions, respectively. The green sphere denotes the position of the doping ions (Nb or Ta)............. 98

4.2 Crystal structure of ideal $In_4Sn_3O_{12}$.. 99

4.3 XRD patterns of $In_4Sn_3O_{12}$ and $In_{4+x}Sn_{3-2x}M_xO_{12}$ (M = $Nb_{0.5}$, $Ta_{0.5}$)............... 99

4.4 Rietveld refinement plots of (a) $In_4Sn_3O_{12}$, (b) $In_{4.5}Sn_2Nb_{0.5}O_{12}$ and (c) $In_{4.5}Sn_2Ta_{0.5}O_{12}$.. 101

4.5 High-resolution XPS spectra of (a) In $3d_{5/2}$, (b) Sn $3d_{5/2}$, (c) O 1s, (d) Nb $3d_{5/2}$ and (e) Ta $4f_{7/2}$ of $In_4Sn_3O_{12}$, $In_{4.5}Sn_2Nb_{0.5}O_{12}$ and $In_{4.5}Sn_2Ta_{0.5}O_{12}$... 104

4.6 UV-Vis absorption spectra (a) and Kubelka-Munk plots (b) of $In_4Sn_3O_{12}$ and $In_{4+x}Sn_{3-2x}M_xO_{12}$ (M = $Nb_{0.5}$, $Ta_{0.5}$) 106

4.7 Photoluminescence spectra of $In_4Sn_3O_{12}$ and $In_{4+x}Sn_{3-2x}M_xO_{12}$ (M = $Nb_{0.5}$, $Ta_{0.5}$) 107

4.8 Calculated band structures along the high symmetry points in the Brillouin zone of a) pure, b) Nb-doped and c) Ta-doped $In_4Sn_3O_{12}$.. 109

4.9 Calculated total and projected density of states of a) pure, b) Nb-doped and c) Ta-doped $In_4Sn_3O_{12}$ 110

5.1 Cl-doped ZnO films, grown via aerosol-assisted CVD, are shown to have potential application as both TCOs and photocatalysts................................. 119

LIST OF FIGURES (Continued)

Figure **Page**

5.2 The schematic illustration of aerosol assist chemical vapour deposition (AACVD) apparatus 123

5.3 Photograph of bare glass (left) and 7 mol% $FeCl_3$ loaded ZnO film (right) .. 126

5.4 High-resolution XPS spectra of (a) Zn $2p_{3/2}$ (b) O 1s of the Cl-doped ZnO film formed from 10mol% $FeCl_3$ and (c) Cl 2p for all films 128

5.5 XRD patterns of simulated bulk ZnO (ICSD #82028), undoped and Cl-doped ZnO thin films 130

5.6 Variation of cell parameters *a*, *c* and cell volume of the films with a change of mol% $FeCl_3$ added to the precursor solution 130

5.7 Top-down and side-on (inset) SEM images of ZnO and Cl-doped ZnO films with mol% $FeCl_3$ loading of (a) 0, (b) 1, (c) 3, (d) 5, (e) 7, (f) 10 and (g) 15 132

5.8 AFM images of (a) undoped ZnO, (b) 10 mol% $FeCl_3$ doped ZnO films as well as their 3D images of the same area (c) and (d) 133

5.9 The formal quantum efficiency (FQE) for the degradation of stearic acid on undoped and Cl-doped ZnO films under UVA illumination. Pilkington *Activ* glass is used as reference 134

5.10 Transmittance (a) and reflectance spectra (b) of all films and the spectrum of bare glass was collected as reference. 136

LIST OF FIGURES (Continued)

Figure **Page**

5.11 Tauc plots of ZnO films (a) and the corrected Tauc plot of ZnO:Cl films with 1 mol% (b), 3 mol% (c), 5 mol% (d), 7 mol% (e) and 10 mol% $FeCl_3$ (f). A broadening parameter $^{\pi}/_{4}\Gamma$ is obtained from the separation of extrapolations along the edge of α (black) and α^2 (blue) plots against $h\nu$, then the parameter is added to the uncorrected band gap to obtain a corrected estimate, as discussed by Dolgonos *et al*. (2016). The extrapolated lines on x-axis show band gap energy (E_g)......................... 138

CHAPTER I

INTRODUCTION

1.1 Significance of the study

Oxide materials play a crucial role in human's lives as they have been used extensively in various aspects, e.g., electronic, magnetic, optical and catalytic applications. A variety of specific uses are attractive such as energy-related, energy storage, dielectric, ferroelectric, optoelectronic, piezoelectric, spintronic and bio-medical materials. The oxide materials can function by their one or more inherent properties, which is versatile for a variety of applications. Two applications are the main focuses of this work: transparent conductors and photocatalysts.

1.1.1 Transparent Conducting Oxides (TCOs)

In this modern day, new age electronic devices, for example, liquid crystal displays (LCDs), touch panel screens, E-papers, defrosting windows, electrochromic windows and mirrors, photovoltaics, flexible electronics and invisible security circuits, play an essential role in our daily life (Gordon, 2000; Ginley and Perkins, 2011). Their essential component is made of materials called transparent conductors (TCs). TCs have been studied extensively as their demand is rapidly increasing every day. TC materials show the unique coexistent properties of optical transparency and electrical conductivity that contribute to these applications. In case those TCs are made of oxides, it can be called transparent conducting oxides or TCOs. Sn-doped In_2O_3, which is known as 'ITO', is one of the most famous TCOs and has been used commercially in the thin-film form because it has good electrical properties (ρ ~10^{-4} Ω.cm) (Gordon, 2000) with excellent transparency (>80%) (Granqvist and Hultåker, 2002).

Besides the optical and electronic properties, other factors, e.g., physical, chemical and thermal durability, toxicity and cost, are crucial and should be taken into account to produce good TCOs as well. Although ITO has good TCO properties and has been widely used, other doped oxides of binary systems such as ZnO, SnO_2, CdO and ternary systems such as $In_4Sn_3O_{12}$, $Zn_2In_2O_5$ and Zn_2SnO_4 are also investigated as they are expected to be alternative materials for TCOs (Minami, 2008). A significant number of oxides with a variety of structures and compositions have been studied widely to meet the requirements for real applications.

1.1.2 Photocatalysts

Concerning environmental issues, photocatalysis plays an important role in many aspects because the solar light is a plentiful and green energy source in the reaction. Photocatalysts can degrade hazardous pollutants especially in sewage water and produce H_2 fuel by water splitting (Pawar and Lee, 2015).

Tremendous reports on photocatalysis have made a relatively long history. TiO_2 is the most well-known photocatalytic oxide because of its many advantages, such as chemical stability, low toxicity, water insolubility, hydrophilicity and low cost (Hernández-Ramírez and Medina-Ramírez, 2015). Moreover, outstanding photocatalytic properties are also discovered in some other metal oxides such as ZnO, Fe_2O_3, Nb_2O_5 and Ta_2O_5 (Candal and Martínes-de la Cruz, 2015).

Research on oxides has resulted in various improved properties as well as more detailed understandings. Various methods are utilised to approach better photocatalytic activity, catalytic kinetics and catalyst stability. Furthermore, many works aim to clarify reaction mechanisms, electronic band structures and other properties such as photoluminescence relating to the photocatalytic performance. Further development of photocatalytic oxides is still crucial in the field of materials science.

1.2 Background of the study

This thesis focuses on investigation of the synthesised materials for transparent conductive and photocatalytic applications. Understanding the relationship between structure and the obtained properties is a key point of the study. The background of structure refinement is crucial to obtain crystal structure of solids. Optical and electrical properties are important to consider materials as TCOs. Photocatalytic properties are used to display self-cleaning properties of thin films.

1.2.1 Crystal structure

1.2.1.1 Structure containing stereochemically active lone-pair electrons

Lone-pair electrons profoundly influence the stereochemistry of inorganic compounds. They cause the structure to be different from that containing bond pairs (Wells, 1974; Hyde and Andersson, 1988). Sidgwick and Powell presented the simple electrostatic theory, which explains that electron-pair repulsions, will be minimised in the most stable shape. Thus, the exact shape of the molecule can be approximated (Sidgwick and Powell, 1940). The geometrical arrangement of many small molecules, e.g., H_2O, NH_3, SF_4, $SnCl_2$, was successfully explained by this theory, which is called Valence Shell Electron Pair Repulsion (VSEPR) (Gillespie and Nyholm, 1957). In many solid oxides, the bond angle is distorted in the presence of lone pair electrons and cations with the lone pair electrons are often off-centered in the polyhedra (Hyde and Andersson, 1988).

The lone pair will be stereochemically active when *s* and *p* orbital of cations are hybridised. Even though their parities are different, sufficient energy can induce the hybridisation and break the symmetry (Orgel, 1959). For example, β-$SnWO_4$ with active lone pair electrons of Sn^{2+} has the strong Sn 5*s*-O 2*p* bonding characteristic which destabilises the structure symmetry. It results in the asymmetric Sn^{2+} environment which appears as an off-centering cation (Figure 1.1(a)). Subsequently, Sn 5*p* orbitals are additionally mixed and the band originates from Sn 5*s*, Sn 5*p* and O 2*p* hybridisation is generated. In some cases, it further creates the dipole moment associating with the non-centrosymmetric crystal structure (Stoltzfus *et al.*, 2007). The lone-pair $6s^2$ electrons of Te^{4+} are also active in generating asymmetric cation environment in some compounds (Halasyamani, 2004). Furthermore, the bonding strength of the anion is reported as the factor affecting the structural symmetry in Tl-containing compounds. The change of Tl^+ environment from closely ideal ($TlNO_3$) to highly distorted (Tl_3BO_3) is responsible for the change of structure from highest to the lowest symmetry (Brown, 2002). An unshared electron pair is not always active if a cationic *s* state is too narrow and not likely to admix with an anionic *p* orbital. This effect is called 'inert pair'. It was suggested that heavier cations or anions reduce the overlap efficiency of cationic *s* orbitals and anionic *p* orbitals (Waghmare *et al.*, 2003). Pb^{2+} in Scheelite-type $PbWO_4$ (Figure 1.1(b) (Stolzfus *et al.*, 2007)) and other ternary oxides are examples of inert lone pair system (Vegard and Refsum, 1927; Stoltzfus *et al.*, 2007). The interaction of Pb 6*s* orbitals to oxygen is reduced by the relativistic effect of Pb; consequently, the structure is stabilised at high symmetry and electron lone pairs are inactive (Stoltzfus *et al.*, 2007).

The lone pair of Pb^{2+} in PbO, however, is apparently active (Leciejewicz, 1961; Hill, 1985). Bi^{3+} in $BiVO_4$ behaves differently depending on the structure, fergusonite or scheelite. Fergusonite phase is found at room temperature and it is transformed to scheelite phase above 566 K. For fergusonite structure, Bi^{3+} site adopts lower symmetry because of the strong Bi 6*s*-O 2*p* interaction. The hybridisation of Bi 6*s* and 6*p* orbitals are allowed; correspondingly, lone-pair electrons become stereochemically active and Bi^{3+} is then off-centered. In contrast, symmetric Bi^{3+} site of the scheelite-type structure is obtained because the Bi 6*s* states are thermodynamically stabilised by weak Bi-O bonding. The cation-anion bonding interaction, which is frequently cation n*s*-O 2*p* character, implies that the cation environment symmetry is the key to consideration of lone pair behavior (Stoltzfus *et al.*, 2007). The effects of these stereoactive lone-pair cations influence the electronic band structure, specifically the position of conduction band and valence band and thus band gap energy.

The off-centered cations with stereoactive electron pairs or the compounds with ns^2np^0 cationic electron configuration commonly exhibit novel properties. They have significant impacts for extensive interesting applications, such as ferroelectric, piezoelectric, multiferroic materials, actuators, non-linear optical materials, ionic conductors and high-refractive index materials (Sidgwick and Powell, 1940; Gillespie and Nyholm, 1957; Orgel, 1959; Walsh *et al.*, 2011). For example, the distorted structures of Tl^+ and Pb^{2+} compounds are accompanied by large dielectric constant (Orgel, 1959). Multiferroics can be found in ABO_3 perovskite (Atou *et al.*, 1999; Seshadri and Hill, 2001) such as $BiMnO_3$ (Baettig *et al.*, 2007). In this case, Bi has active lone-pairs and Mn is magnetic which show ferroelectricity and ferromagnetism, respectively.

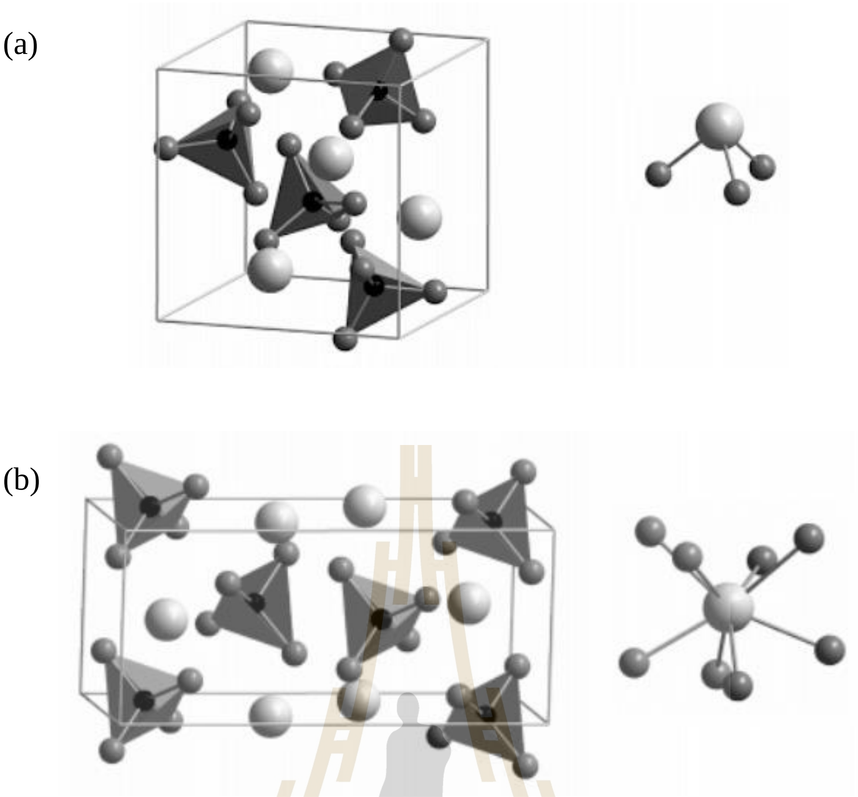

Figure 1.1 The structure and cation environment of (a) β-$SnWO_4$ and (b) Scheelite $PbWO_4$, where the black spheres, the dark grey spheres and the light-grey spheres represent transition metal ions, oxygen ions and the p-block cations, respectively (Stoltzfus *et al*., 2007).

1.2.1.2 Structure refinement

Structural refinement is a method used to determine the crystallographic information, e.g., atomic coordinates, atomic occupancy, lattice parameters, bond length and bond angle, from XRD patterns. The technique allows us to gain an understanding of structural details of the synthesised materials.

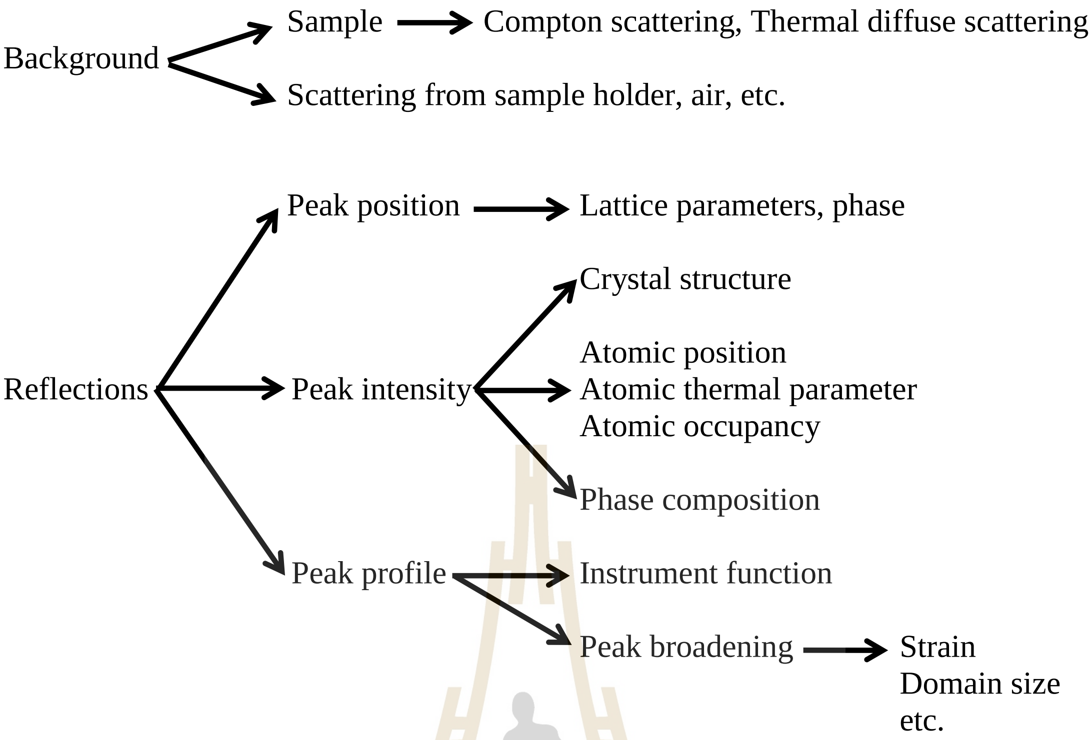

Figure 1.2 Schematic diagram demonstrating the obtained sample and structural information relating to XRD data (adapted from Dinnebier, 2001).

Structure refinement approaches, which are in common usage at the present, include ‘Rietveld refinement’ and ‘Le Bail refinement’. Rietveld refinement is also called ‘whole-profile refinement’ (Rietveld, 1969). Le Bail refinement is sometimes called a ‘structure-free approach’ (Le Bail *et al.*, 1988). For the Le Bail method, the refinement deals with peak position using only hkl or space group giving lattice parameters. The Rietveld method is applied to deal with all structural parameters, which mainly include space group, atomic positions, thermal or atomic displacement parameter, atomic occupancy, peak intensity and peak profile (peak shape, FWHM). Full structural details are obtained beyond lattice parameters, for example, bond length and angle.

The principle of refinement is based on least square method. The equation used to explain is as follow:

$$S_y = \sum_i w_i [y_i(obs) - y_i(calc)]^2 \qquad [1]$$

where S_y is the weight difference between the observed intensity $[y_i(obs)]$ and calculated intensity $[y_i(calc)]$ at step *i* of a diffraction pattern and $w_i = 1/y_i$.

The process is to achieve a best fit between raw pattern and calculated pattern derived from structural model with the convergence approach. The structural model generally used is crystallographic information file (CIF). The optimum match observed when S_y is minimised. This can be evaluated by a parameter called the weight-profile R value or R_{wp}, which is defined as:

$$R_{wp} = \{\sum_i w_i [y_i(obs) - y_i(calc)]^2 / \sum_i w_i [y_i(obs)]^2\}^{1/2} \qquad [2]$$

Another important term is R_{exp}, which is the value reflecting the quality of original data collected from XRD, i.e., the counting statistics. The high quality XRD pattern is obtained by collecting a good number of data points gradually to overcome errors from counting statistics. R_{exp} is described as:

$$R_{exp} = [(N - P) / \sum_i^N w_i y_i(obs)^2]^{1/2} \qquad [3]$$

where N and P is the number of observation and parameters, respectively. R_{wp} is ideally required to be equal to R_{exp}, which is explained in term of GOF (goodness of fit) or chi-square (χ^2) as:

$$\chi^2 = R_{wp}/R_{exp} \qquad [4]$$

(McCusker *et al.*, 1999).

Both free and licensed softwares for structure refinement are available. Examples of widely used freeware are GSAS (Generalized Structure Analysis System) (Larson and Dreele, 2004), Fullprof (Rodriguez-Carvajal, 1993) and RIETAN

(Li *et al.*, 2010). In case of licensed software, Expert High Score Plus is commonly used. Recently, another attractive refinement package is TOPAS from Bruker. It is a graphical based profile analysis program, which supports both graphical user interface (GUI) and launch modes. The program has the advantage of convenient use with the stable, fast and accurate operation, and many powerful features are added. Moreover, quantitative analysis is supported to provide phase composition; the precision of processing has led it to becoming the industrial standard for industrial areas, such as the cement and mining industries (Bruker AXS, 2008).

1.2.2 Optical properties

1.2.2.1 Interactions of UV-Visible light and solids

The interactions between UV-Visible light and solids can be absorption, emission, scattering and reflection (Figure 1.3). Solids usually reflect light on their surfaces and with no energy loss, this phenomenon is called ‘diffuse reflection’ (West, 2014). Diffuse reflectance spectra of solid materials are obtained from the interaction of light with a flat surface of specimen (Dann, 2000). The color of many solids mainly originates from both absorption and emission. Materials absorb the specific energy range of the electromagnetic spectrum corresponding to the band gap energy. At the same time, the emission and the reflectance of the residual energy range generate the emitted visible light (West, 2014).

The interaction of light and atoms is used to investigate the optical properties of solids (Tilley, 2013). The energy in UV-Visible causes the excitation of valence electrons, which can be between sub-levels of partially-filled bands or valence band and conduction band and thus gives the electronic transition details (Cox, 1987). If the photon energy equal to or greater than the energy gap between filled and empty levels, the photon will be absorbed (Figure 1.4(a)). Otherwise, it may be scattered. At the excited state, the excited electrons may go back to the ground state by releasing the absorbed photons. This step is called 'spontaneous emission' (Figure 1.4(b)). The color is observed in the case of the allowed transition within the energy separation such as d-d transition (Tilley, 2013). The starting point in the absorption spectra could be used to simply estimate band gap energy according to the band structure (Cox, 1987). The quantitative analysis can be obtained from the intensity, which attributes to the probability of the transition (Atkins et al., 2014).

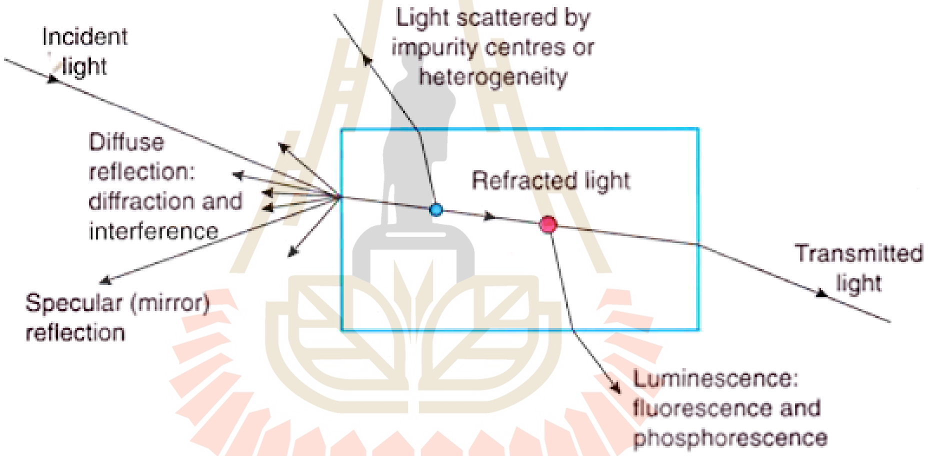

Figure 1.3 The interactions between the incident light and solids (West, 2014).

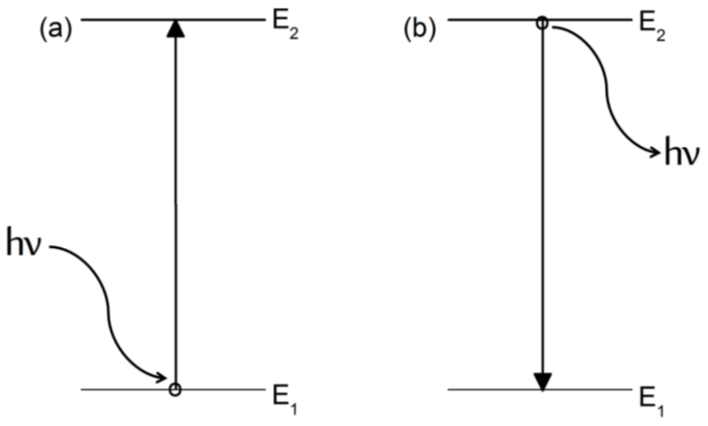

Figure 1.4 Absorption (a) and spontaneous emission (b) of light radiation (Tilley, 2013).

As mentioned earlier, the band gap energy is significant to determine the electronic and optical properties. The diffuse reflectance UV-Vis spectra obtained from solids can be used to extract band gap energy (Gibbs *et al*., 2013; Dolgonos *et al*., 2014) using the theory proposed by Kubelka and Munk (Kubelka and Munk, 1931). The model originates from the concept of light traveling inside a light-scattering specimen. In a real situation, however, the particle size of most samples is higher than the wavelength of incident light. The Kubelka-Munk (K-M) equation [5] is applied to an infinite-thick sample at any wavelength.

$$\frac{K}{S} = \frac{(1-R_\infty)^2}{2R_\infty} \equiv F(R_\infty) \qquad [5]$$

where R = reflectance, $R_\infty = R_{sample}/R_{standard}$, $F(R_\infty)$ is a K-M function, K and S are the absorption and scattering coefficients, respectively (Torrent and Barrón, 2002). In the band structure, bandgap and absorption coefficient are related (Smith, 1978) and thus the K-M function is expressed as equation [6]:

$$[F(R_\infty)h\nu]^{1/n} = C(h\nu - E_g) \qquad [6]$$

where C is a proportionality constant and n = 1/2 and 2 for direct and indirect allowed transition, respectively and E_g is band gap energy. The extrapolation of the highest slope on the horizontal axis in the plot of $[F(R_\infty)h\nu]^{1/n}$ with the corresponding n against $h\nu$ gives the estimated band gap energy (Pal *et al*., 2012].

Another technique widely used to extract band gap energy is Tauc method (Tauc, 1968). The principle is based on absorption or transmission phenomena. This method is rather standard in thin films (Hamberg and Granqvist, 1986; Amanullah *et al*., 1995; Granqvist and Hultåker, 2002; Torkaman *et al*., 2010). The transmission spectra are used to produce band gap energy with the following relation (Tauc, 1974):

$$(\alpha h\nu)^{1/n} = \beta\left(h\nu - E_g\right) \qquad [7].$$

β is a constant value called band tailing parameter. n is valued corresponding to the type of transition similarly mentioned above in K-M relation. α is absorption coefficient, which can be calculated from %transmission (%T). %T must be converted to absorbance (A) by the equation: $A = 2 - \log_{10}\%T$. The absorption coefficient α is then calculated from $\alpha = A/t$ where t is thickness (metre, SI unit for length). Thickness is a crucial factor used to determine band gap energy in thin films as thicker films are more strongly absorbing due to bulk absorbance. Finally, band gap energy can be obtained by using the extrapolation on the steepest section of the curve onto *x* axis from the plot between $(\alpha h\nu)^{1/n}$ and $h\nu$.

On the other hand, the accuracy of band gap determination of degenerately doped semiconductor has been recently addressed by Dolnogos *et al.* (2016). Doping produces electron-electron and electron-impurity scattering, which narrow a fundamental band gap as a result of the fundamental band gap renormalisation (ΔE_g^{RN}) (Berggren and Sernelius, 1981). In contrast, band gap can be widened by Moss-Burstein shift (ΔE_g^{BM}) (Moss, 1954; Burstein, 1954). With heavily doping, electron carrier density surpasses conduction band edge density of state-leads to the raise of Fermi level (E_F) to higher energy level lying inside the conduction band. Band gap energy is then referred to the energy difference between the top of valence band and the unoccupied energy states in the conduction band (Figure 1.5). Therefore, the consideration for several band alterations is critical.

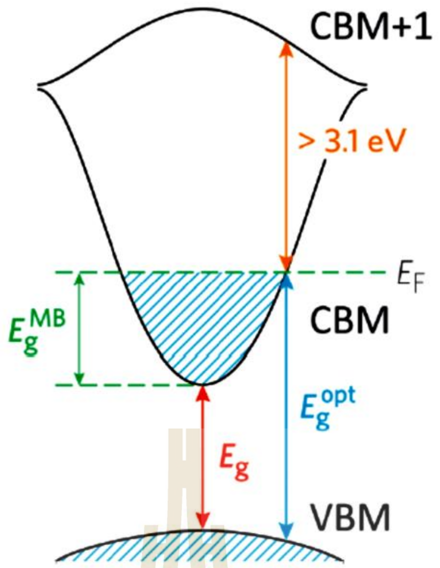

Figure 1.5 Diagram explaining the effect of Moss-Burstein shift in degenerately doped semiconductors (Dixon *et al.*, 2016).

The corrected Tauc plot was proposed to get accurate band gap energy (Dolnogos *et al.*, 2016). In degenerately doped materials, high electron density leads to increased collision and therefore scattering of electrons in both the initial and final stages of photon absorption. This can be quantified by broadening parameter Γ in the following relationship:

$$\alpha^2 \propto 1 - \frac{\pi\Gamma}{4}\left(E_g - h\nu\right) \qquad [8]$$

However, this method is applicable only for direct band gap while it is still a matter of uncertainty to correct indirect band gap.

In oxides of cations containing d orbitals, the electronic structures can be explained primarily based on the ‘crystal-field’ theory and the applied molecular orbital theory, ‘ligand-filed’ theory. Ligand-field splitting parameter and valence electrons are the factors determining the energy of electronic transition hence the color of those metal oxides (Atkin *et al.*, 2014).

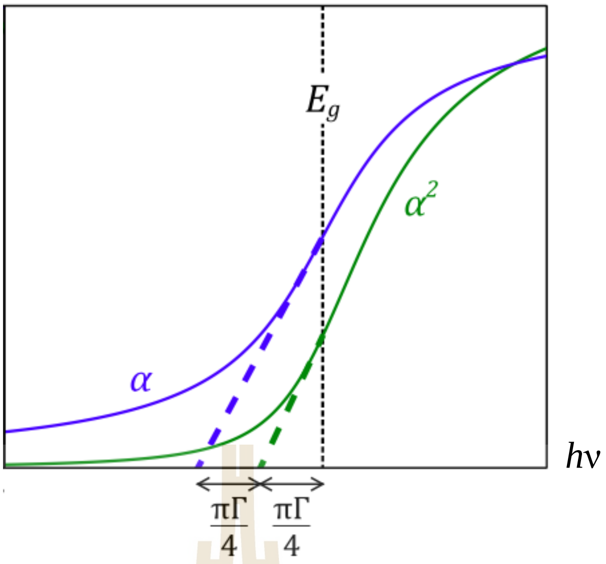

Figure 1.6 The corrected Tauc plot method for degenerately doped semiconductors. The band gap is obtained from the broadening parameter πΓ/4 added to the *x* axis (Dolnogos *et al*., 2016).

1.2.2.2 Luminescence spectroscopy

Solids can illuminate by the emission of radiation after the energy absorption (Figure 1.7). The materials that show luminescence property are known as phosphors. The main components of the phosphor are host and activator. Activator is the ion that can absorb and emit light at a specific wavelength. In oxides, doping ions are an activator. Besides, extra dopants can be added to function as a sensitiser (Atkins *et al*., 2014; Ronda, 2008) when the activators have weak absorption because of some reasons; for example, the transition is forbidden. The sensitiser acts as the photon acceptor and later transfers the energy to the activator (Ronda, 2008).

The phenomena can be divided based on spin multiplicity and timescale. Fluorescence occurs when the excited and ground state have the same spin thus it is fast to radiate with the delay time less than 10^{-8} s. Conversely, phosphorescence has the spin forbidden mechanism. It requires the flip of spin during a radiative decay process. This can happen via intersystem crossing with the occurrence of spin-orbit coupling but it takes longer time. Typically, the emitted energy is lower because of non-radiative relaxation like thermal vibration (Atkins *et al*., 2014). The shift to lower energy of emission peaks or red shift, which is called ‘Strokes shift’, is due to ‘Frank-Condon’ effect. The amount of absorbed energy is slightly less than band gap energy; therefore, the highest-energy luminescent peak is often referred to ‘near band-edge emission’. Nonetheless, the shift to higher energy or blue shift may happen through two possible phenomena: the non-radiative relaxation of the extra energy caused by some vibrational energy absorptions in the lattice and the multiple photon absorptions called ‘up-conversion’ (Kitai, 2008; Shinde *et al*, 2013).

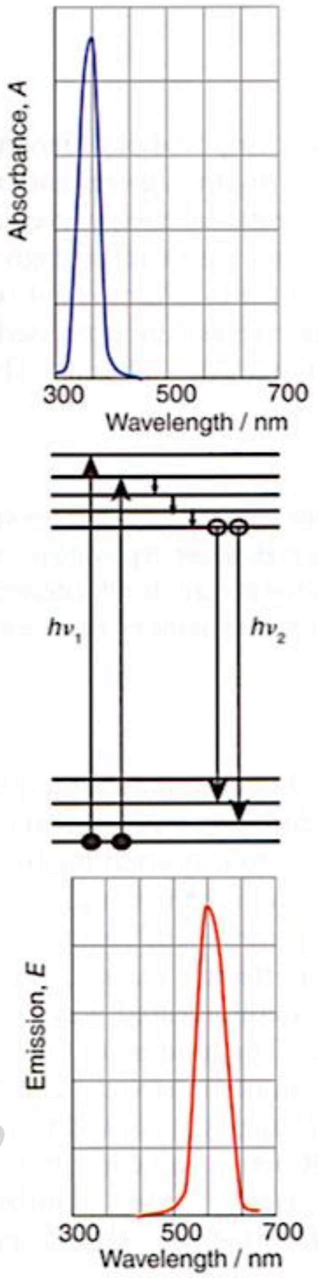

Figure 1.7 The energy level diagram coupled with absorption and emission spectra (Atkins *et al*., 2014).

The luminescence can be specifically named regarding the source of energy. When light is the source of energy, it is called photoluminescence; Luminescence with electricity and electron beams as the source would name electro-luminescence and cathodoluminescence, respectively. In general, photoluminescence of solids is the absorption of photons usually in UV region and the emission in the visible region (Atkins *et al*., 2014).

1.2.3 Electrical properties and band structures

In any solid, a band structure is built of frontier atomic orbitals. The degree of overlap affects the bandwidth as well as the band gap; the better atomic overlap, the wider band and band gap. The band gap energy, which is generally the separation between valence band and conduction band, determines the electrical properties of solids: metals, semiconductors and insulators (Atkins *et al.*, 2014; West, 2014). It refers to the energy required for electrons to move from valence band to conduction band (West, 2014). The filling level of electrons in the band also predicts the electronic properties (Dann, 2000). The highest occupied energy level at T = 0 K, which is defined as Fermi level, is another crucial component in the band structure. The density of states (DOS) is defined from the concentration of states within the band (Atkins *et al.*, 2014).

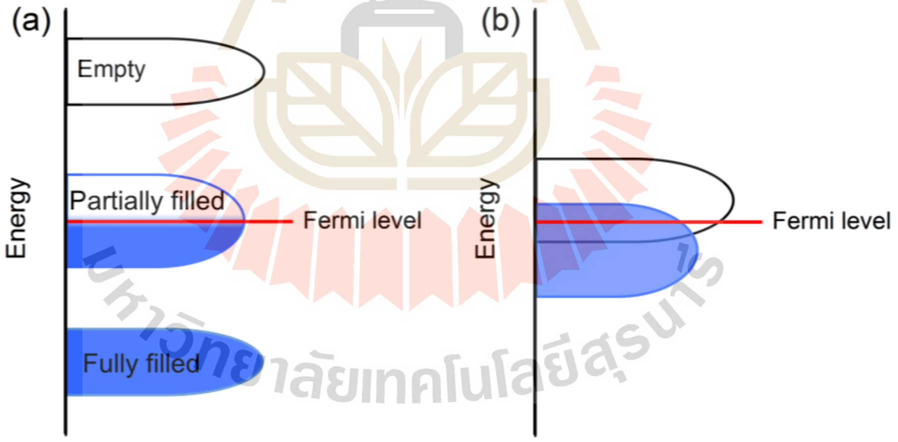

Figure 1.8 The band structure of metals (Atkins *et al.*, 2014; Dann, 2000).

Materials can be divided into three types based on their electronic properties. In metals, electrons are partially filled in the band (Figure 1.8(a)) hence they need minimal energy to move to higher energy level. As a consequence, metals are conducting and the conductivity is greater than semiconductors and insulators but the conductivity decreases with increasing temperature (Figure 1.9) (Atkins *et al*., 2014; Dann, 2000). As the temperature increases, the electron-phonon collisions play a role to obstruct the electrons movement and suppress the conductivity (West, 2014). The band structure of metals can also be illustrated as shown in Figure 1.8(b) when the energy levels of the bands are very close thus they start to overlap (Dann, 2000). The main attractive point of metals is that most electrons are delocalised and move freely for the entire structure (West, 2014).

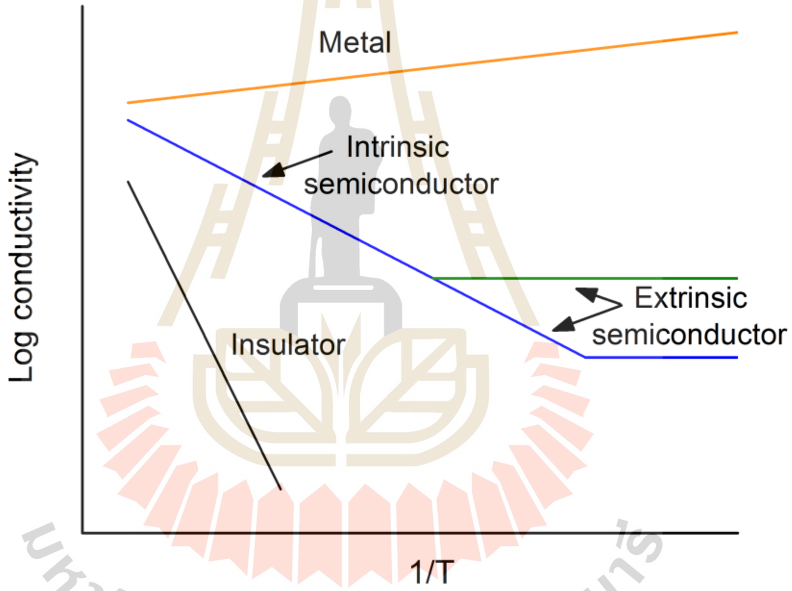

Figure 1.9 The plots of conductivity vs. 1/T for metals, semiconductors and insulators (West, 2014).

The band structure of semiconductors can be differentiated depending on the related behavior, intrinsic or extrinsic type. An intrinsic or natural semiconductor (Figure 1.10(a)) has small thermal activation energy; therefore, some electrons can be promoted to the next conduction band level leaving holes in the valence band. The conduction comes from both electrons and holes and the thermal energy raises the conductivity (Atkins *et al*., 2014). The substitution using other heterovalent atoms to introduce excess carriers of electrons or holes produces extrinsic semiconductors. The semiconductivity is divided into n- and p-type, when n and p correspond to the negative and positive charge carriers, respectively. Their band structures show the presence of extra bands; filled donor bands lay below the conduction band (n-type) (Figure 1.10(b)) whereas empty acceptor bands lay over the valence band (p-type) (Figure 1.10(c)) (Atkins *et al*., 2014). The materials are insulating or have a small conductivity at low temperature. They can electrically conduct when the temperature is high enough to meet the minimum energy (band gap energy) required for electrons to jump across the gap to the conduction band. The electrical conductivity is a function of temperature (Figure 1.9) (Atkins *et al*., 2014; Dann, 2000) as can be explained by the Arrhenius equation [9]:

$$\sigma = \sigma_0 e^{-E_a/kT} \qquad [9]$$

when $\sigma = ne\mu$ where n = carrier concentration, e = electrical charge and μ = carrier mobility. E_a is defined as the activation energy of mobile carriers which is equal to the energy gap between the donor levels and the conduction band (or valence band to acceptor levels) (West, 2014).

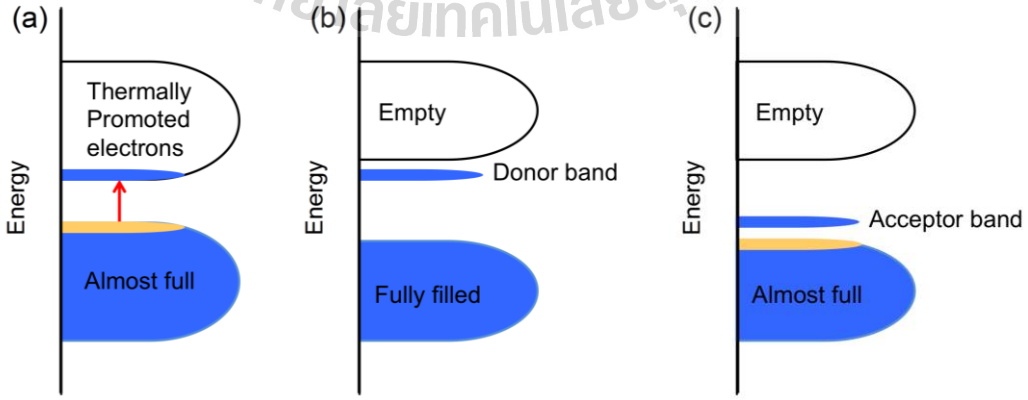

Figure 1.10 The band structures of (a) intrinsic and extrinsic semiconductors of (b) n-type and (c) p-type (Atkins *et al*., 2014).

In case that electrons are filled in the valence band and the band gap is large, the band structure is of insulators (Figure 1.11) (Atkins *et al*., 2014). Their electronic behaviors (Figure 1.9) are similar to that of semiconductors but the gap energy needed for conducting is much greater (Dann, 2000). Few electrons in valence band can be promoted to conduction band; therefore, minimal conductivity is observed for insulators (West, 2014).

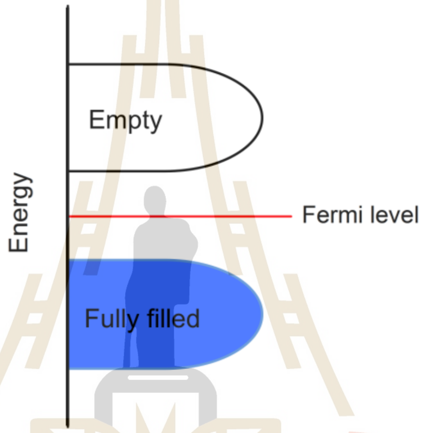

Figure 1.11 The band structure of insulators (Atkins *et al*., 2014).

In metal oxides, M *d* orbitals and O 2*p* orbitals usually overlap and generate bonding and antibonding molecular orbitals (Figure 1.12). The energy change of bands as a function of wavevector (*k*), called a 'band dispersion', depends on the bond interaction. Large dispersion is a result of strong bonding interaction. In a real situation, a three-dimensional model is applicable and the direction of electrons is considered. The band structure of RuO_2 is displayed as an example in Figure 1.13(a). The *x*-axis is the label of '***k*** vector' or '***k***-space'. For example, Γ stands for the position ***k*** = (0,0,0). Figure 1.13(b) presents different ***k***-space in the first Brillouin zone, which is the primitive cell in the reciprocal lattice (Cox, 2010). On the other hand, the band structure calculation is commonly performed by the augmented plane wave (APW) method when Schrödinger's equation is numerically integrated to produce crystal orbitals. Example of the calculated density of states (DOS or N(E)) is shown in Figure 1.14 (Cox, 2010).

Besides, the calculated electronic band structure can distinguish the type of band gap (Figure 1.15). If the conduction band minimum and the valence band maximum are at the same position in ***k***-space, the transition is direct and the band gap is called 'direct band gap energy'. In case these two positions are different, the momentum change is needed in the transition and the band gap is called 'indirect band gap energy' (Cox, 1987). In summary, the band structure gives information for the analysis of bonding interaction, the type of band gap and finally the electronic properties (Cox, 1987; Cox, 2010).

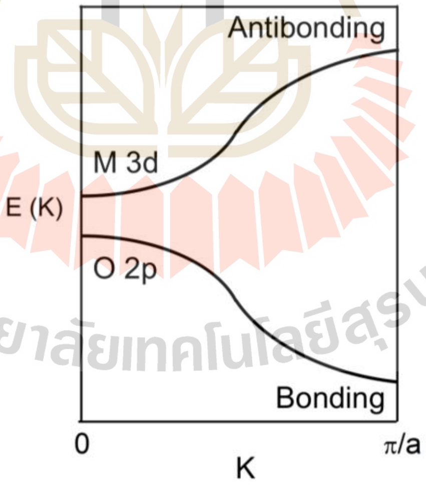

Figure 1.12 One-dimensional band structure resulted from bonding and antibonding of M-O (Cox, 2010).

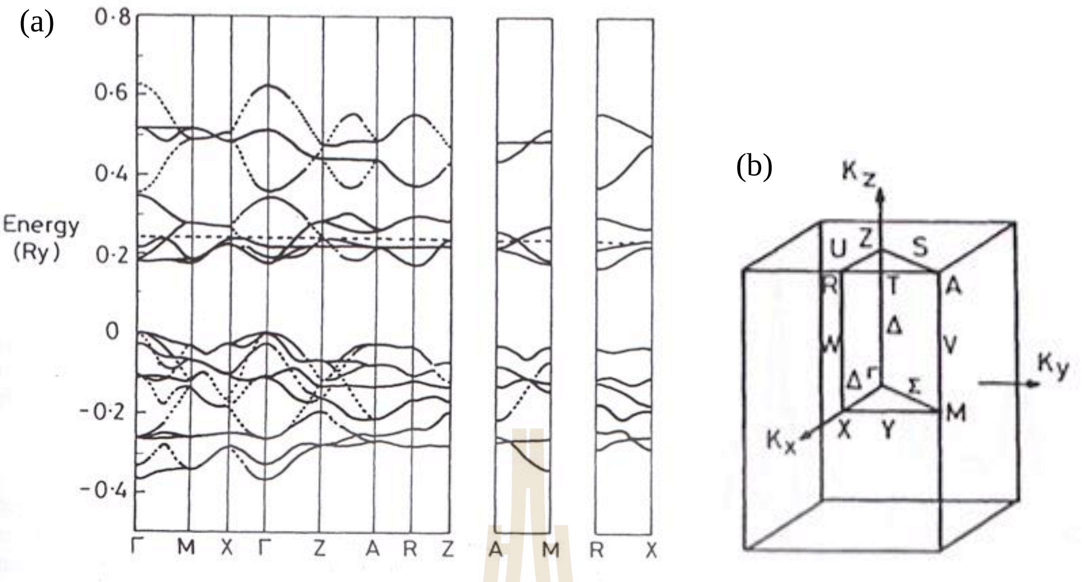

Figure 1.13 (a) The electronic band structure of RuO_2 (b) the first Brillouin zone for tetragonal rutile lattice of RuO_2 displaying different ***k***-space (Cox, 2010).

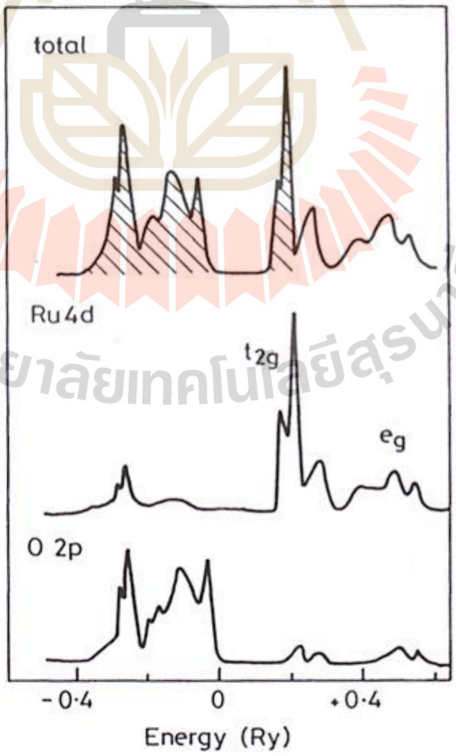

Figure 1.14 The calculated density of states of RuO_2 for total contribution and from atomic orbitals contribution of Ru *4d* and O *2p* (Cox, 2010).

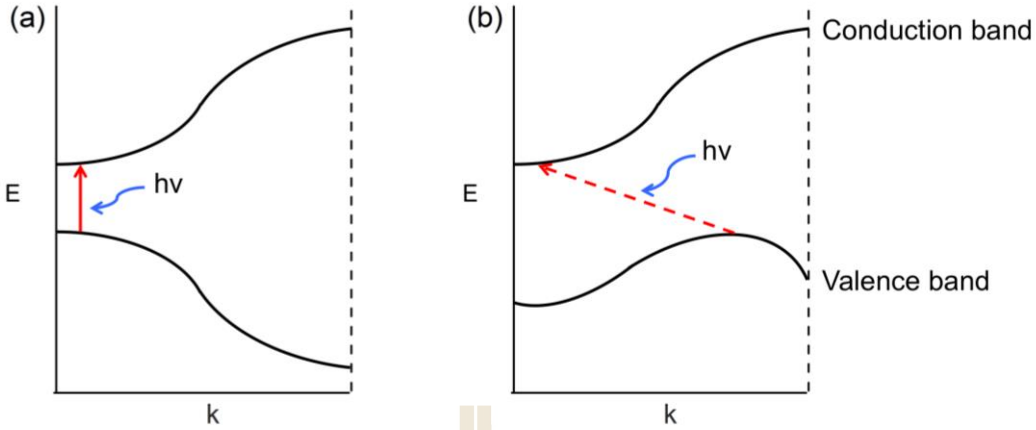

Figure 1.15 Band gap types: (a) direct and (b) indirect (Cox, 1987).

1.3 Transparent Conducting Oxides (TCOs)

TCOs have the extraordinary feature of simultaneous transparency and conductivity. TCOs are generally defined as heavily doped wide band gap oxides (Sleight, 2010). Large band gap energy, which is defined as greater than 3 eV (Hautier *et al*., 2014), is desirable in oxide host materials in order to have no or weak visible light absorption. The ability to be doped to generate low resistivity (<10^{-2} Ω.cm) are required for TCO properties (Dixon *et al*., 2016). The strategies to improve the electrical properties are to enhance carrier concentration and mobility. Doping is a strategy to introduce carrier density into the parent oxide materials. However, doping always cause some optical absorption. This can be understood from the relationship between absorption coefficient (α) and the density of free electrons (*n*) as:

$$\alpha = \sigma n \qquad [10]$$

where σ = the absorption cross section. The optical absorption could be observable with heavily doping which causes the number of free electrons (Peelaers *et al*., 2012). Good TCOs are then further achieved by the high carrier mobility where high conductivity can be obtained with maximum transparency (Sleight, 2010). In addition, carrier mobility is considered as an important factor to improve conductivity when carrier density is low compared with that in metals (Shanthi et al., 1999). The band produced by *s* orbitals, called *s* band, has high carrier mobility or low effective mass (Sleight, 2010). In the band structure, these conduction band will have large dispersion and high curvature (Ganose and Scanlon, 2016; Edwards *et al.*, 2004). Conduction band minimum made of *s*-character orbitals thereby normally create n-type TCOs. Conversely, it is challenging to produce p-type TCOs as valence band is scarcely made of *s* band and high mobility is not obtained in other bands such as *d* bands (Sleight, 2010). Furthermore, open *d*-shell transition metals are an inappropriate choice of TCOs as the d-d transition often generates color materials (Sleight, 2010).

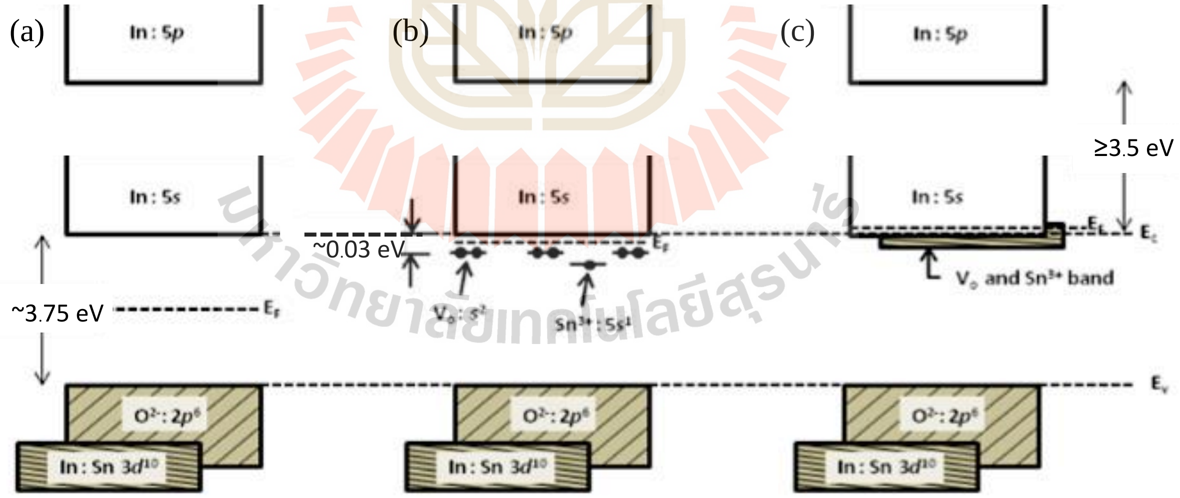

Figure 1.16 The simple band structures of (a) stoichiometric In_2O_3, (b) slightly doped In_2O_3 and (c) heavily doped In_2O_3 (Fan and Goodenough, 1977).

The most famous TCOs is Sn-doped In_2O_3 which is well known as ‘ITO’. ITO’s simple band structure is a good example to understand the TCO properties (Figure 1.16).

Stoichiometric In_2O_3 is an insulator with large band gap energy (E_g ~3.75 eV) (Figure 1.16(a)). The introduction of defects, usually either Sn (heterovalent atom) and/or oxygen vacancy, into the host lattice can be viewed as the insertion of donor states into the band structure (Figure 1.16(b)). This reduces the activation energy hence the conductivity of the doped In_2O_{3-x} is raised. At the point where the defect content is high enough, their impurity levels can overlap and form the impurity bands below the conduction band (Figure 1.16(c)). If this extra band is wide enough to overlap with the conduction band, the final conduction band covers the energy range where the Fermi level lies and the compound becomes metallic. Eventually, the doped In_2O_{3-x} can electrically conduct while the transparency is maintained because band gap energy is still larger than the visible light energy (Fan and Goodenough, 1977).

1.4 Photocatalysis

Photocatalysis is composed of two processes: photoreaction and catalysis. Catalysis is the process to accelerate reactions where a catalyst participates in but is not consumed. The catalyst has an important role in reducing the activation energy by modifying the reaction pathway and enhancing the rate of reaction. Therefore, photocatalysis is the photoreaction containing the catalyst called ‘photocatalyst’ (Ohtani, 2011). The classification of the photocatalysts is the same as that of general catalysts. If the phase of reactants and photocatalysts are the same, the reaction is known as ‘homogeneous photocatalysis’. In contrast, ‘heterogeneous photocatalysis’ is used when they have different phases.

The reaction occurs on the surface of catalysts as depicted in Figure 1.17 (Aditya *et al*., 2015). The UV and/or visible light with the energy equal to or higher than bandgap ($h\nu \geq E_g$) initiates the excitation of electrons and then electrons (e^-) and holes

(h^+) are generated as the pairs of electron-hole. The redox reaction is further progressed otherwise the recombination of electrons and holes will take place. The competition between these two events implies the photocatalytic efficiency. The photocatalytic activity is defined as the capability of created electron-hole pairs participated in the redox reaction (Pawar and Lee, 2015).

Semiconducting metal oxides have promising photocatalytic properties as they can create charge carriers. Here, applications of photocatalysts for pollutant degradation are discussed.

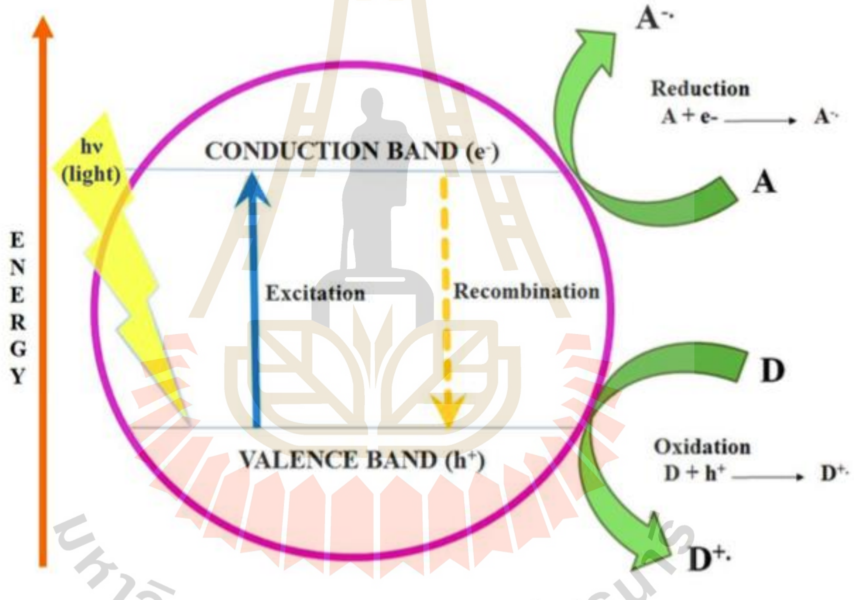

Figure 1.17 A schematic diagram of a photocatalytic process (Aditya *et al*., 2015).

In photocatalytic reactions, electrons and/or holes generated by the photocatalysts react through the reduction and/or oxidation process with the target chemicals. In pollutant degradation, O_2 is reduced to O_2^- anions while OH^- anions are oxidised and transformed to •OH radicals. Thus, electrons and holes act as a reducing and oxidising agent, respectively. The •OH radicals and O_2^- anions then react with pollutants to decompose or transform them to less-toxic byproducts. The details of the mechanism are proposed as follows (Pawar and Lee, 2015).

Semiconductor + $h\nu \rightarrow h^+ + e^-$ [11]

$h^+ + H_2O \rightarrow \bullet OH + H^+$ [12]

h^+ + pollutant $\rightarrow$ (pollutant)$^+$ [13]

$e^- + O_2 \rightarrow \bullet O_2^-$ [14]

$\bullet O_2^- + H^+ \rightarrow \bullet OOH$ [15]

$\bullet OOH \rightarrow O_2 + H_2O_2$ [16]

$H_2O_2 + \bullet O_2^- \rightarrow \bullet OH + OH^- + O_2$ [17]

$H_2O_2 + h\nu \rightarrow 2(\bullet OH)$ [18]

Pollutant + ($\bullet OH$, h^+, $\bullet OOH$ or O_2^-) $\rightarrow$ pollutant degradation [19]

In the redox reaction, the generated electrons and holes participate in reduction and/or oxidation depending on the band edge potential of conduction band and valence band comparing to that of reaction (Ohtani, 2011). Reduction can occur in case the reactant is anionic species such as methyl orange (MO) (Wang *et al.*, 2007), Eosin yellow (EY) (Laid *et al.*, 2015) and nitrophenol (Aditya *et al.*, 2015) while cationic species such as methylene blue (MB) (Houas *et al.*, 2001; Xiang *et al.*, 2013; Fan *et al.*, 2011), Malachite green oxalate (MG) (Laid *et al.*, 2015) and RhodamineB (RhB) (Xing *et al.*, 2016) acts as a reactant in oxidation.

In case of film application, the photocatalytic degradation of stearic acid was purposed as an example of dirt or pollutant. The efficiency was investigated in terms of formal quantum efficiency (FQE), which is the number of stearic acid molecules degraded per incident photon. The photocatalytic degradation reaction can be described as: $CH_3(CH_2)_{16}CO_2H + 26O_2 \xrightarrow{(h\nu \geq Eg)} 18CO_2 + 18H_2O$ [20]

1.5 Material syntheses

1.5.1 Solid State reaction

Solid state reaction has high potential to prepare a wide range of materials including oxides, sulfides, nitrides, etc. Primarily, it is the basis of the most frequently used procedures for preparing oxides in a great number of industries because of ease and low cost of production and apparatus. None or fewer solvents and residual left after the reaction greatly benefit for reducing the time and cost to remove byproducts or waste, which make the method environmentally friendly.

The solid state reaction is defined as the reaction between two or more solids. The preparation can be done by mixing all powder reactants according to stoichiometric ratio and then thoroughly grinding to achieve a homogeneous mixture of reactants. For manual mixing of small quantities, usually an agate mortar and pestle are employed. Sufficient amount of some volatile organic liquid, such as acetone or alcohol, is sometimes added to the mixture to aid homogenisation. In case of a large portion of precursors (> 20 g), a grinder called ball mill was used for preparation. The well-mixed powder is sometimes pressed into pellets or some other shapes such as bar and then heated in a furnace to assist subsequent chemical reaction. According to Tamman's rule, the optimal reaction temperature is suggested to be two-thirds of the melting point of lower melting precursors. Commonly, the obtained pellets are reground and reheated for several times to complete the reaction of all precursors.

The solid state reaction can proceed well or not depending on some factors. First, contact area between reacting solids is considered as one important factor. The use of high surface area precursors or making a pellet of mixed precursors increases intimate contact between crystallites. Second, diffusion rate is another crucial factor, which can be increased by increasing reaction temperature or using reactants that decomposed easily either before or during reaction such as nitrates and carbonates. Third, using the starting reagents that have the crystal structure similar to that of the product can maximise nucleation rate of product phase. This is described as ‘topotactic transformation’, which means the lattice in the initial and final state are related (West, 2014).

1.5.2 Aerosol Assisted Chemical Vapour Deposition (AACVD)

Chemical vapour deposition (CVD) is a solid film fabrication process with the principle of use of volatile precursors to deposit on the solid substrate via inert carrier gas or vacuum. CVD is useful for wide variety of applications such as glass/steel coating and small-scale coating, i.e., microelectronics (Jones and M. L. Hitchman, 2009). This technique benefits good quality of films: pure, uniform, high-dense, excellent-coverage, well-adhered and robust film, which are desirable for production in industrial scale (Marchand *et al*., 2013; Choy, 2003).

Aerosol Assisted CVD is the expansion of classical CVD that based on the solution precursors. The advantages of AACVD are addressed in many points. The most important benefit is that it enlarges the number of choice of precursors other than volatile precursors and thus a film material by use of solvent-soluble precursors. It is possible to reduce the cost production of a film by using other starting materials rather than volatile precursors (Hou and Choy, 2006). The precursor delivery process of aerosol from a precursor solution is simple and inexpensive, which is a crucial consideration for material production in industrial scale (Hou and Choy, 2006). Mass transport rate of precursors by aerosol route is high (Choy, 2003) compared to classical CVD providing a high deposition rate (Hou and Choy, 2006) Furthermore, AACVD can be conducted under low/atmospheric pressure or open atmosphere, which simplifies and lowers the cost of film deposition process (Choy, 2003; Marchand *et al*., 2013). Interestingly, crystal structure and film morphology can be controlled by deposition condition such as deposition temperature and rate (Jones and Hitchman, 2009; Choy, 2003), types of precursors, solvents, substrates, growth period and additives (Marchand *et al*., 2013).

The AACVD process can be described in Figure 1.18. First, (a) the 'aerosol' is produced from soluble precursors in solvents by an aerosol generator such as ultrasonicator via the atomisation/vapourisation process. Then, they are transported to the CVD reactor by use of an inert carrier gas such as nitrogen or argon. Second, (b) the aerosol precursors diffuse over the heated substrate, the solvents are evaporated and the precursors are vapourised leaving gas-phase reactant. Third, (c) weak physisorption of gas molecules onto substrate occurs which leads to film deposition (including nucleation and film growth) via heterogeneous reaction. In some cases, gas-phase intermediates are formed prior to the adsorption. Finally, (d) byproducts and solvents are removed out of the reactor through exhaust by the gas flow. Another possible reaction, often in case the substrate temperature is too high, is homogeneous reaction occurred in the vapour phase giving fine solid particle and if they are adsorbed on the substrate, porous films are produced (Choy, 2003; Hou and Choy, 2006).

Some factors are needed to take into an account to get the optimum film deposition, e.g., precursors, solvents and carrier gas. Starting materials can be varied from a liquid or a solid dissolved in a suitable solvent, which has a low vapour pressure, low viscosity and yields high solubility of solid in solution precursors (Hubert-Pfalzgraf and Guillon, 1998). A carrier gas is necessary to assist aerosol to have enough pressure and is transported to the reaction chamber. The gas flow rate has to be optimised to maximise the deposition rate (Marchand *et al*., 2013). Nitrogen and argon are the most common inert carrier gas used. Some gases can be functioned as both carrier and synthesis gas: compressed air is used to deposit oxide films and H_2 can be acted as reducing agent. Sometimes H_2 is introduced together with an inert gas like argon to assist the reaction (Hou and Choy, 2006; Glerup *et al*., 2003).

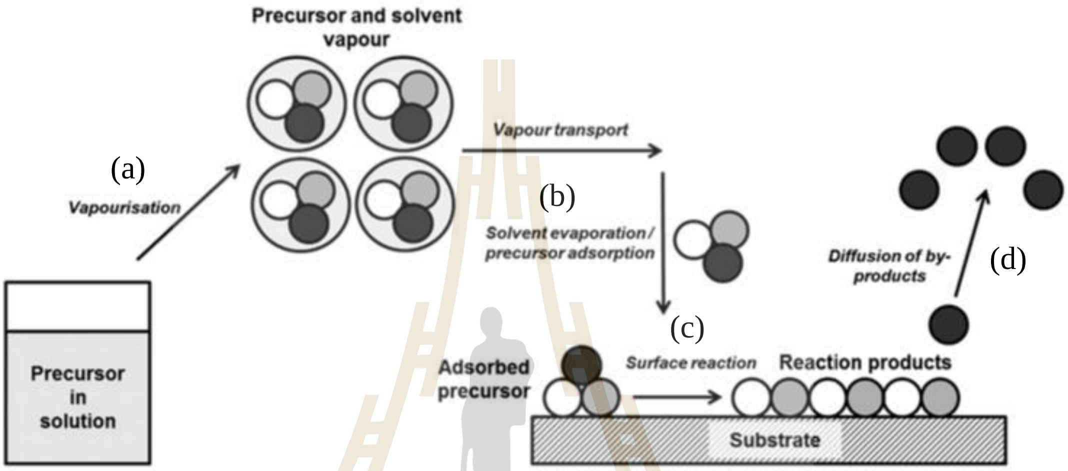

Figure 1.18 The schematic diagram of Aerosol Assisted Chemical Vapour Deposition (AACVD) (Marchand *et al*., 2013).

1.6 Scope and limitations of the study

This thesis focuses on Indium-based oxides (In_2TeO_6 and $In_4Sn_3O_{12}$) and Zinc oxide (ZnO). Solid state synthesis was used to synthesise $In_{2-x}M_xTeO_6$ (M = Ga, Bi, La) and $In_{4+x}Sn_{3-2x}M_xO_{12}$ (M_x = $Nb_{0.5}$, $Ta_{0.5}$) polycrystalline powders. Aerosol assisted chemical vapour deposition was used to prepare Cl-doped ZnO thin films.

Various techniques were utilised to characterise synthesised materials. To identify the phase purity, X-ray diffraction (XRD) was used. Both Rietveld refinement using TOPAS software and Le Bail refinement using GSAS were utilised to gain crystallographic information of synthesised materials. To get the chemical composition, X-ray photoelectron spectroscopy (XPS), X-ray absorption near-edge spectroscopy (XANES) and Energy dispersive spectroscopy (EDS) were used. To obtain surface morphology and topology, Scanning electron microscopy (SEM) and Atomic force spectroscopy (AFM) were used, respectively. To determine the optical properties, UV-Vis spectrometer and photoluminescence (PL) measurement were used. DFT calculation was performed to provide band structure, which is useful to understand optical and electrical properties.

To investigate the electrical properties, four-probe point method and Hall effect measurement were used. Transparent conducting oxides (TCO) properties including optical and electrical properties are studied in term of transparency and conductivity (or resistivity). The degradation of stearic acid under UVA light is used to determine the photocatalytic performance of materials.

1.7 References

Aditya, T., Pal, A. and Pal, T. (2015). Nitroarene Reduction: A Trusted Model Reaction to Test Nanoparticle Catalyst. **Chemical Communications.** 51: 9410-9431.

Amanullah, F. M., Pratap, K. J. and Hari Babu, V. (1995). Characterization of Isochronally and Isothermally Annealed Indium Tin Oxide Thin Films. **Thin Solid Films.** 254: 28-32.

Atkins, P. W., Overton, T. L., Rourke, J. P., Weller, M. T. and Armstrong, F. A. (2014). **Inorganic Chemistry**, 6th eds. Oxford University Press. 2014.

Atou, T., Chiba, H., Ohoyama, K., Yamaguchi, Y. and Syono, Y. (1999). Structure Determination of Ferromagnetic Perovskite $BiMnO_3$. **Journal of Solid State Chemistry.** 145: 639-642.

Baettig, P., Seshadri, R. and Spaldin, N. A. (2007). Anti-Polarity in Ideal $BiMnO_3$. **Journal of the American Chemical Society.** 129: 9854-9855.

Berggren, K. -F. and Sernelius, B. E. (1981). Band-gap narrowing in heavily doped many- valley semiconductors. **Physical Review B.** 24: 1971-1986.

Brown, I. D. (2002). **The Chemical Bond in Inorganic Chemistry; IUCr Monographs on Crystallography, Vol. 12.** Oxford University Press, New York.

Bruker AXS (2008). TOPAS V4: General Profile and Structure Analysis Software for Powder Diffraction Data. User's Manual, Bruker AXS, Karlsruhe, Germany.

Burstein, E. (1954). Anomalous Optical Absorption Limit in InSb. **Physical Review Journals Archive.** 93: 632.

Candal, R. and Martínes-de la Cruz, A. (2015). Chapter 2 New Visible-Light Active Semiconductors in **Photocatalytic Semiconductors: Synthesis, Characterization and Environmental Applications.** Springer Cham Heidelberg New York Dordrecht London.

Choy, K. L. (2003). Chemical Vapour Deposition of Coatings. **Progress in Materials Science.** 48: 57-170.

Cox, P. A. (1987). **The Electronic Structure and Chemistry of Solids.** Oxford Science Publications.

Cox, P. A. (2010). **Transition Metal Oxides: An Introduction to their Electronic Structure and Properties**, Republished. Oxford University Press.

Dann, S. E. (2000). **Reactions and Characterization of Solids.** Royal Society of Chemistry.

Dinnebier, R. (2001). Newsletter no. 26 of International Union of Crystallography. Commission on Powder Diffraction.

Dixon, S. C., Scanlon, D. O., Carmalt, C. J. and Parkin, I. P. (2016). n-Type Doped Transparent Conducting Binary Oxides: An Overview. **Journal of Materials Chemistry C.** 4: 6946-6961.

Dolgonos, A., Lam, K., Poeppelmeier, K. R., Freeman, A. J. and Mason, T. O. (2014). Electronic and Optical Properties of $Ga_{3-x}In_{5+x}Sn_2O_{16}$: An Experimental and Theoretical Study. **Journal of Applied Physics.** 115: 013703.

Dolgonos, A., Mason, T. O. and Poeppelmeier, K. R. (2016). Direct optical band gap measurement in polycrystalline semiconductors: A critical look at the Tauc method. **Journal of Solid State Chemistry**. 240: 43-48.

Dryden, N. H., Shapter, J. G., Coatsworth, L. L., North, P. R. and Puddephatt, R. J. (1992). [$CF_3Au(C{\equiv}NMe)$.] As A Precursor for CVD of Gold. **Chemistry of Materials.** 4: 979-981.

Edwards, P. P., Porch, A., Jones, M. O., Morgan, D. V. and Perks, R. M. (2004). Basic Materials Physics of Transparent Conducting Oxides. **Dalton Transaction.** 2004, 0: 2995-3002.

Fan, J. C. C. and Goodenough, J. B. (1977). X-ray Photoemission Spectroscopy Studies of Sn-Doped Indium-Oxide Films. **Journal of Applied Physics.** 48: 3524-3531.

Fan, G., Sun, W., Wang, H. and Li, F. (2011). Visible-Light-Induced Heterostructured Zn-Al-In Mixed Metal Oxide Nanocomposite Photocatalysts Derived from A Single Precursor. **Chemical Engineering Journal.** 174: 467-474.

Ganose, A. M. and Scanlon, D. O. (2016). Band Gap and Work Function Tailoring of SnO_2 for Improved Transparent Conducting Ability in Photovoltaics. **Journal of Materials Chemistry C.** 4: 1467-1475.

Gibbs, Z. M., Lalonde, A. and Snyder, G. J. (2013). Optical band gap and the Burstein-Moss effect in iodine doped PbTe using diffuse reflectance infrared Fourier trans- form spectroscopy. **New Journal of Physics.** 15: 075020.

Gillespie, R. J. and Nyholm, R. S. (1957). Inorganic Stereochemistry. **Quarterly Reviews (London).** 11: 339-380.

Ginley, D. S. and Perkins, J. D. (2010). **Handbook of Transparent Conductors.** Springer New York Heidelberg Dordrecht London.

Glerup, M., Kanzow, H., Almairac, R., Castignolles, M. and Bernier, P. (2003). Synthesis of Multi-Walled Carbon Nanotubes and Nano-Fibres using the Aerosol Method with Metal-Ions as the Catalyst Precursors. **Chemical Physics Letters.** 377: 293-298.

Gordon, R. G. (2000). Criteria for Choosing Transparent Conductors. **MRS Bulletin**. 25: 52-57.

Granqvist, G. C. and Hultåker, A. (2002). Transparent and Conducting ITO Films: New Developments and Applications. **Thin Solid Films.** 411: 1-5.

Granqvist, G. C., Azens, A., Heszler, P., Kish, L. B. and Österlund, L. (2007).. Nanomaterials for Benign Indoor Environments: Electrochromics for “Smart Windows”, Sensors for Air Quality and Photo-Catalysts for Air Cleaning. **Solar Energy Materials & Solar Cells.** 91: 355-365.

Hamberg, I. and Granqvist, C. G. (1986). Evaporated Sn-doped In_2O_3 Films Basic Optical Properties and Applications to Energy-Efficient Windows. **Journal of Applied Physics.** 60: R123-R159.

Halasyamani, P. S. (2004). Asymmetric Cation Coordination in Oxide Materials: Influence of Lone-pair Cations on The Intra-Octahedral Distortion in d^0 Transition Metals. **Chemistry of Materials.** 16: 3586-3592.

Hernández-Ramírez, A. and Medina-Ramírez, I. (2015). Chapter 1 Semiconducting Materials in **Photocatalytic Semiconductors: Synthesis, Characterization and Environmental Applications.** Springer Cham Heidelberg New York Dordrecht London.

Hill, R. J. (1985). Refinement of the Structure of Orthorhombic PbO (massicot) by Rietveld Analysis of Neutron Powder Diffraction Data. **Acta Crystallographica Section C.** C41, 1281.

Hou, X. and Choy, K.-L. (2006). Processing and Applications of Aerosol-Assisted Chemical Vapor Deposition. **Chemical Vapor Deposition.** 12: 583-596.

Houas, A., Lachheb, H., Ksibi, M., Elaloui, E., Guillard, C. and Herrmann, J.-M. (2001). Photocatalytic Degradation Pathway of Methylene Blue in Water. **Applied Catalysis B: Environmental.** 31: 145-157.

Hubert-Pfalzgraf, L. G. and Guillon, H. (1998). Trends in Precursor Design for Conventional and Aerosol-Assisted CVD of High-T_c Superconductors. **Applied Organometallic Chemistry.** 12: 221-236.

Hyde, B. G. and Andersson, S. (1988). **Inorganic Crystal Structures.** Wiley, New York.

Jones, A. C. and Hitchman M. L. (2009). **Chemical Vapour Deposition: Precursors, Processes and Applications.** RSC Publishing.

Kitai, A. **Luminescent Materials and Applications.** John Wiley & Sons, Ltd. 2008.

Krishna, R. M., Hayes, T. C., Krementz, D., Weeks, G., Torres, A. M., Brinkman, K. and Mandal, K. C. (2012). Characterization of Transparent Conducting Oxide Thin Films Deposited on Ceramic Substrates. **Materials Letters.** 66: 233-235.

Kubelka, P. and Munk, F. (1931). Ein Beitrag zur Optik der Farbanstriche. **Zeitschrift fur Technische Physik.** 12: 593-601.

Laid, N., Bouanimba, N., Zouaghi, R. and Sehili, T. (2015). Comparative Study on Photocatalytic Decolorization of An Anionic and A Cationic Dye using Different TiO_2 Photocatalysts. **Desalination and Water Treatment.** 57: 19357-19373.

Larson, A. C. and Von Dreele, R. B. (2004). General Structure Analysis System (GSAS)'. Los Alamos National Laboratory Report LAUR, 86-748.

Le Bail, A., Duroy, H. and Fourquet, J. L. (1988). Ab-Initio Structure Determination of $LiSbWO_6$ by X-ray Powder Diffraction. **Materials Ressearch Bulletin.** 23: 447-452.

Leciejewicz, J. (1961). On the Crystal Structure of Tetragonal (red) PbO. **Acta Crystallographica.** 14: 1304.

Li, J., Smith, A. E., Kwong, K.-S., Powell, C., Sleight, A. W. and Subramanian, M. A. (2010). Lattice Crossover and Mixed Valency in the $LaCo_{1-x}Rh_xO_3$ Solid Solution. **Journal of Solid State Chemistry.** 183: 1388-1393.

Marchand P., Hassan I. A., Parkin I. P. and Carmalt, C. J. (2013). Aerosol-Assisted Delivery of Precursors for Chemical Vapour Deposition: Expanding the Scope of CVD for Materials Fabrication. **Dalton Transactions.** 42: 9406-9422.

McCusker, L. B., Von Dreele, R. B., Cox, D. E., Louër, D. and Scardi, P. J. (1999). Appl. Cryst. 32: 36-50.

Minami, T. Takeda, Y., Takata, S. and Kakumu, T. (1997). Preparation of Transparent Conducting $In_4Sn_3O_{12}$ Thin Films by DC Magnetron Sputtering. **Thin Solid Films.** 308-309: 13-18.

Minami, T. (1999). Transparent and Conductive Multicomponent Oxide Films Prepared by Magnetron Sputtering. **Journal of Vacuum Science & Technology A**. 17: 1765-1772.

Minami, T. (2008). Present Status of Transparent Conducting Oxide Thin-Film Development for Indium-Tin-Oxide (ITO) Substitutes. **Thin Solid Films.** 516: 5822-5828.

Moss, T. S. (1954). The Interpretation of the Properties of Indium Antimonide. **Proceedings of the Physical Society of London (Section B).** 76: 775.

Mryasov, O. N. and Freeman, A. J. (2001). Electronic Band Structure of Indium Tin Oxide and Criteria for Transparent Conducting Behavior. **Physical Review B.** 64: 233111.

Ohtani, B. (2011). Photocatalysis by Inorganic Solid Materials: Revisiting Its Definition, Concepts and Experimental Procedures. **Advances in Inorganic Chemistry.** 63: 395-430.

Orgel, L. E. (1959). The Stereochemistry of B Subgroup Metals: Part II, The Inert Pair. **Journal of the Chemical Society (Resumed).** 0: 3815-3819.

Pal, M., Pal, U., Jiménez, J. M. G. Y and Pérez-Rodríguez, F. (2012). Effects of Crystallization and Dopant Concentration on The Emission Behavior of TiO_2: Eu Nanophosphors. **Nanoscale Research Letters.** 7:1-12.

Palgrave, R. G. and Parkin, I. P. (2007). Aerosol Assisted Chemical Vapor Deposition of Gold and Nanocomposite Thin Films from Hydrogen Tetrachloroaurate (III). **Chemistry of Materials.** 19: 4639-4647.

Pawar, R. and Lee, C. S. Chapter 1-Basics of Photocatalysis in **Heterogeneous Nanocomposite-Photocatalysis for Water Purification**. Elsevier. William Andrew. 2015.

Peelaers, H., Kioupakis, E. and Van de Walle, C. G. (2012). Fundamental Limits on Optical Transparency of Transparent Conducting Oxides: Free-Carrier Absorption in SnO_2. **Applied Physics Letters.** 100: 011914.

Rietveld, H. M. (1969). A Profile Refinement Method for Nuclear and Magnetic Structures. **Journal of Applied Crystallography.** 2: 65-71.

Rodriguez-Carvajal, J. (1993). Recent Advances in Magnetic Structure Determination by Neutron Powder Diffraction. **Physica B.** 192: 55-69.

Ronda, C. (2008). **Luminescence from Theory to Applications.** Wiley-VCH, NewYork.

Seshadri, R. and Hill, N. A. (2001). Visualizing the Role of Bi 6s “Lone Pairs” in the Off-Center Distortion in Ferromagnetic $BiMnO_3$. **Chemistry of Materials.** 13: 2829-2899.

Shanthi, S., Subramanian, C. and Ramasamy, P. (1999). Growth and Characterization of Antimony Doped Tin Oxide Thin Films. **Journal of Crystal Growth.** 197: 858-864.

Shinde K. N., Dhoble, S. J., Swart, H. C. and Park, K. (2013). Chapter 2 Basic Mechanism of Photoluminescence (p.41-59) in **Phosphate Phosphors for Solid-State Lighting**. Springer Series in Materials Science, Springer-Verlag Berlin Heidelberg.

Sidgwick, N. V. and Powell, H. M. (1940). **Stereochemical Types and Valency Groups. Proceedings of The Royal Society of London: Series A, Mathematical and Physical Sciences.** 176: 153-180.

Sleight, A. Chapter 9 Chemistry of Band Structure Engineering in **Handbook of Transparent Conductors**. Springer New York Heidelberg Dordrecht London. 2010.

Smith, R. A. (1978). **Semiconductors**, 2nd eds. Cambridge University Press, Cambridge.

Stoltzfus, M. W., Woodward, P. M., Seshadri, R., Klepeis, J.-H. and Bursten, B. (2007). Structure and Bonding in $SnWO_4$, $PbWO_4$ and $BiVO_4$: Lone Pairs vs Inert Pairs. **Inorganic Chemistry.** 46: 3839-3850.

Tauc, J. (1968). Optical Properties and Electronic Structure of Amorphous Ge and Si. **Materials Research Bulletin.** 3: 37-46.

Tauc, J. in: Tauc J. (1974). (Ed.), Amorphous and Liquid Semiconductors, Plenum Press, London and New York.

Tilley, R. J. D. (2013). **Understanding Solids: The Science of Material**s, 2nd eds. John Wiley & Sons, Ltd.

Torkaman, N. M., Ganjkhanlou, Y., Kazemzad, M., Dabaghi, H. H. and Keyanpour-Rad, M. (2010). Crystallographic Parameters and Electro-Optical Constants in ITO Thin Films. **Materials Characterization.** 61: 362-370.

Torrent, J. and Barrón, V. (2002). **Encyclopedia of Surface and Colloid Science.** Marcel Dekker, Inc., New York.

Vegard, L. and Refsum, (1927). **A. Norske Vid. Akad. Skr. Oslo Math. Nat. Kl. (No.2)**.

Waghmare, U., Spaldin, N. A., Kandpal, H. C. and Seshadri, R. (2003). First-Principles Indicators of Metallicity and Cation Off-Centricity in the IV-VI Rocksalt Chalcogenides of Divalent Ge, Sn and Pb. **Physical Review B.** 67: 125111.

Walsh, A., Payne, D. J., Egdell, R. G. and Watson, G. W. (2011). Stereochemistry of Post-Transition Metal Oxides: Revision of the Classical Lone Pair Model. **Chemical Society Reviews.** 40: 4455-4463.

Wang, W.-D., Huang F.-Q., Liu, C.-M., Lin, X.-P. and Shi, J.-L. (2007). Preparation, Electronic Structure and Photocatalytic Activity of the In_2TiO_5 Photocatalyst. **Materials Science and Engineering B.** 139: 74-80.

Wells, A. F. (1974). **Structural Inorganic Chemistry**, 4th eds. Oxford University Press, Oxford.

West, A. R. (2014). **Solid State Chemistry and its Applications**, 2nd eds (Student Edition). John Wiley & Sons, Ltd.

Xiang, X., Xie, L., Li, Z. and Li, F. (2013). Ternary $MgO/ZnO/In_2O_3$ Heterostructured Photocatalysts Derived from A Layered Precursor and Visible-Light-Induced Photocatalytic Activity. **Chemical Engineering Journal.** 221: 222-229.

Xing, Y., Que, W., Yin, X., He, Z., Liu, X., Yang, Y., Shao, J. and Kong, L. B. (2016). $In_2O_3/Bi_2Sn_2O_7$ Heterostructured Nanoparticles with Enhanced Photocatalytic Activity. **Applied Surface Science.** 387: 36-44.

Xu, C., Hampden-Smith, M. J. and Kodas, T. T. (1995). Aerosol-Assisted Chemical Vapor Deposition (AACVD) of Binary Alloy (Ag_xPd_{1-x}, Cu_xPd_{1-x}, Ag_xCu_{1-x}) Films and Studies of Their Compositional Variation. **Chemistry of Materials.** 7: 1539-1546.

CHAPTER II

LITERATURE REVIEWS

2.1 In_2TeO_6-based oxides

In_2TeO_6 has hexagonal Na_2SiF_6-type structure (P_{321}). The structure consists of the three-dimensional corner sharing network of InO_6 octahedra (Figure 2.1). The octahedral units of Te do not connect with each other but connect to InO_6 units by edge-sharing (Redman *et al.*, 1971; Siritanon *et al.*, 2011).

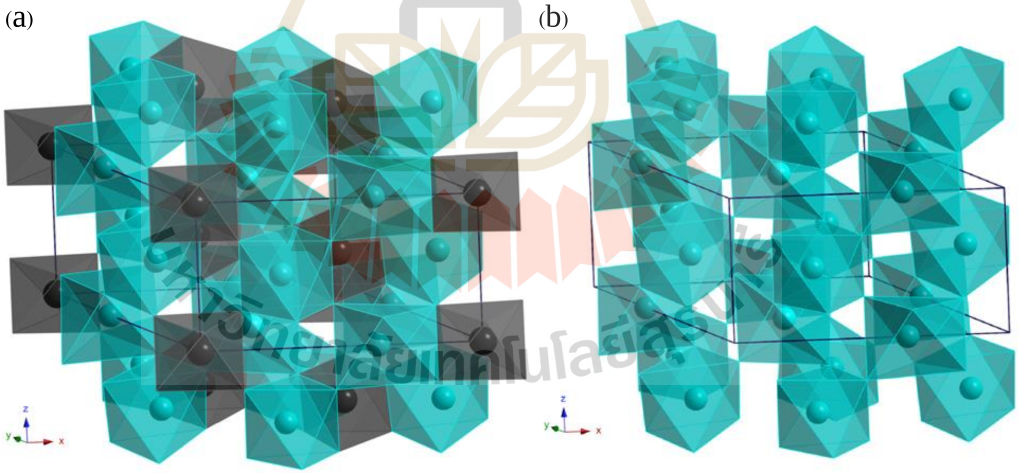

Figure 2.1 (a) The structure of In_2TeO_6 where In^{3+} and Te^{6+} octahedra are represented in turquoise and black, respectively (b) Corner shared octahedral network of $In^{3+}O_6$ (Siritanon *et al.*, 2011).

Indium tellurium oxide was first prepared from In_2O_3 and H_6TeO_6 by solid state reaction (Natansohn, 1968). Redman *et al.* (Redman *et al.*, 1971) later found that

In_2TeO_6 is formed after heating $In_2Te_3O_9$ at a temperature higher than 650 °C in air. Two space groups have been reported for In_2TeO_6; P_{321} (Frit B, 1975) and $P\bar{3}m_1$ (Shannon *et al*., 1977).

There are only a few reports on electronic properties of In_2TeO_6 related compounds. While stoichiometric In_2TeO_6 are an insulator (Shemirani and Koffyberg, 1992), oxygen-deficient In_2TeO_{6-x} behaves as a degenerate semiconductor (Shannon *et al.*, 1977). $In_2Te_{6-x}Re_xO_6$ is also reported to be semiconductor but with lower conductivity (Shannon *et al*., 1977).

Few elements have been used to substitute In in In_2TeO_6 in an attempt to create extrinsic semiconductors. Only Sn and Zr-doped In_2TeO_6 have been reported to show n-type semiconducting behavior. On the other hand, there is no known p-type doped In_2TeO_6 and Zn-doped In_2TeO_6 in insulating (Shemirani and Koffyberg, 1992). After that, compositionally controlled metal-insulator transition was observed in $Tl_{2-x}In_xTe_xO_6$ solid solution (Siritanon et al., 2011).

As the optical band gap of Sn-doped In_2TeO_6 is large (2.93 eV) and some compounds in this family have been reported to show semiconducting behavior, it might be possible to design transparent conductors based on In_2TeO_6.

Recently, the calculation study derived from the density functional theory (DFT) suggests that In_2TeO_6 has the capability to be good n-type TCOs. The overlap of In *s*-character orbital and oxygen generates a wide conduction band which results in highly mobile carriers with low effective mass. This implies that the material could have high conductivity. On the other hand, the band gap enrgy of slightly smaller than 3 eV could result in little absorption in the visible region. Further computational analysis of doped In_2TeO_6 has not been done yet (Hautier *et al*., 2014).

2.2 $In_4Sn_3O_{12}$-based oxides

$In_4Sn_3O_{12}$ adopts a rhombohedral unit cell (hexagonal basis) in a trigonal space group ($R\bar{3}$). The structure (Figure 2.2(a) (Choisnet *et al*., 2007)) consists of two distinct sites of octahedra (3*a*) and seven-fold polyhedra (18*f*) which are labeled as M1 and M2, respectively. One-seventh of M1 cation site is occupied by Sn while the rest of Sn and all In are in the remaining M2 sites (Nadaud *et al*., 1998; Choisnet *et al*., 2007). In another side of view, its structure derives from M_7O_{12}-type oxygen-deficient fluorite structure (Figure 2.2(b)) (Pitschke *et al*., 2000).

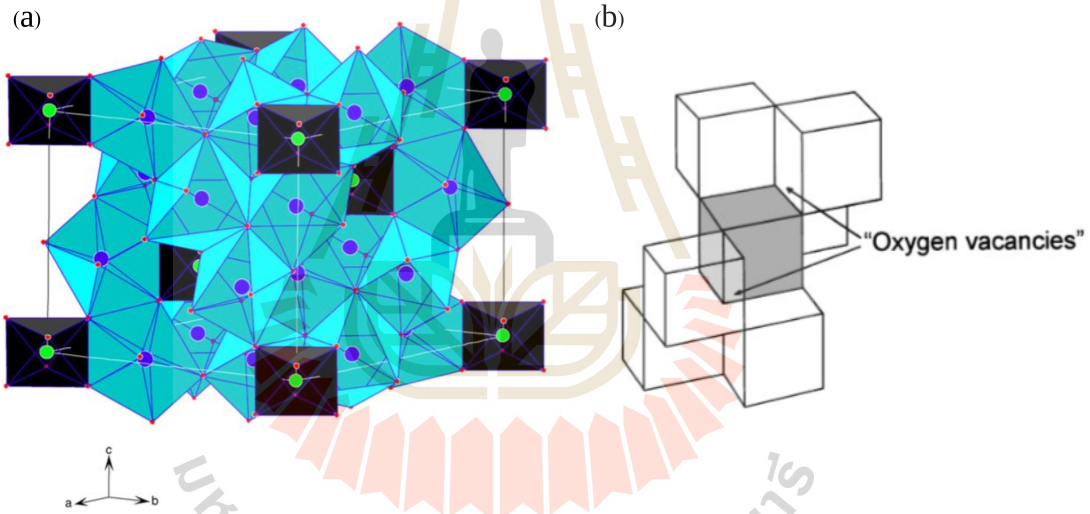

Figure 2.2 (a) The structure of M_7O_{12} when black and blue areas are octahedra and seven-fold unit, respectively (Choisnet *et al*., 2007) (b) Shaded space represents octahedra and non-shaded one is seven-coordinated polyhedral (Pitschke *et al*., 2000).

In 1986, Bates *et al*. first discovered the electrical conductivity of $In_4Sn_3O_{12}$ (120 S/cm at 1200 K) (Bates *et al*., 1986). It was then prepared as the highly conductive transparent thin film as the new TCOs candidate. The film was reported with desirable electronic and optic properties, which are high conductivity in the order of 10^4 S/cm and visible transmittance of greater than 80%. Moreover, the high carrier mobility of 20 $cm^2V^{-1}s^{-1}$ was obtained (Minami *et al*., 1997). The preparation conditions for a thin film such as O_2 partial pressure and location on substrate strongly influence the obtained electrical properties. Besides, the thin film thickness is one of the factors (Minami *et al*., 1997; Minami, 1999). By annealing in Ar, the oxygen-deficient $In_4Sn_3O_{12-\delta}$ was obtained with an n-type degenerate semiconducting behavior (Behr and Krabbes, 1996).

Many researchers found the formation of $In_4Sn_3O_{12}$ phase during the investigation of In_2O_3-SnO_2 solid solution. Nadaud *et al*. revealed the minimum Sn doping content (6 at%) for the synthesis at 1550 °C (Naduad *et al*., 1998). Ohya *et al*. found that a hexagonal phase begins to form at 1335-1345 °C (Ohya *et al*., 2000) which is consistent with the temperature range of 1325-1350 °C reported by Heward and Swenson (Heward and Swenson, 2007). It was suggested that the non-linearity of lattice constant with higher content of Sn in In_2O_3-SnO_2 solid solution may come from two possible reasons; first, the loss of oxygen and second, the reducing atmosphere (Ohya *et al*., 2000). González et al. utilised the Synchrotron-based high-energy XRD as an *in situ* probe to determine the formation kinetics and crystal structure. The phase transformation of In_2O_3 and SnO_2 under the isothermal heat at 1335-1400 °C can be explained using JMAK (Johnson-Mehl-Avrami-Kolmogorov) and JMAK-like models. The first grains began to form at 1345 °C. At 1400 °C, $In_4Sn_3O_{12}$ phase increases while ITO and SnO_2 phases decrease as a function of time (González *et al*., 2008).

The extensive structural details were given and the attempt to explain the relationship between M cations environments and electrical properties was presented. Apart from structure refinement results mentioned above, the M-O bond length in the first shell obtained from EXAFS later supports the crystallographic data (Naduad *et al*., 1998). By considering isoelectronic cations of Sn^{4+}, Sb^{5+} and Te^{6+}, new indium tellurate

In_6TeO_{12} was synthesised to expand the scope of the study and the insight of crystallographic structure and structure-bonding anisotropy for all compounds were provided (Choisnet *et al*., 2007).

The thermodynamic stability of $In_4Sn_3O_{12}$ was suggested by an atomistic simulation method. A phase can be predicted using the ionic ratio of $r_{A^{3+}}/r_{B^{4+}}$ when C.N. = 8 and 6, respectively. The trends are as follows: disordered fluorite < 1.21 < δ phase or defected fluorite < 1.42-1.44 < pyrochlore < 1.78-1.83 < monoclinic pyrochlore < 1.92 (Starnek *et al.*, 2009). Moreover, the artificial intelligent techniques in computational engineering were used to predict the physical properties of the solid solution of $In_4Sn_3O_{12}$ and In_6WO_{12} (Bizo and Anghel, 2010).

The introduction of some cations for $In_4Sn_3O_{12}$ was studied. Pitschke first introduced either Y or Ti into $In_4Sn_3O_{12-\delta}$, with the formula $(In_{1-x}Y_x)_4Sn_3O_{12-\delta}$ and $In_4(Sn_{1-x}Ti_x)_3O_{12-\delta}$, respectively. These dopants did not increase carrier conductivity but enhance Seebeck coefficient and hence thermoelectric properties (Pitschke *et al*., 2000). Later, $In_4Sn_3O_{12}$ was doped by Ga but the samples contain some impurities although they are beneficial for thermoelectric properties (Zhou *et al*., 2011). The conductivity improvement was carried out by Sb displacement in $In_{4+x}Sn_{3-2x}Sb_xO_{12}$ (x = 0-1.5). A semiconductor turns to be a semi-metallic with Sb doping and the sample with x = 1 (In_5SnSbO_{12}) enhances the conductivity by one order of magnitude while the optical bandgap only slightly increases. It was assumed that the position of conduction band energy level contributed from Sb empty orbital as well as the contribution of Sb over 3*a* and 18*f* sites might be the reason (Choisnet *et al*., 2004). After this work, the electronic band structures of $In_4Sn_3O_{12}$ and In_5SnSbO_{12} investigated by the first-principle DFT calculations elucidate that Sb doping increases conduction band dispersion, which could be the explanation of the observed high electrical conductivity. The effective mass was also estimated for the prediction. The clarification, nevertheless, has been still of interest and progressing (Ren *et al*., 2006).

The electronic structure of the $In_4Sn_3O_{12}$ thin film was investigated more by both experimental and computational methods. The valence band photoemission spectra were reported. The occupied state at Fermi level was observed at conduction minimum of around 0.45 eV when calculated from a simple free electron model. This was further used to estimate the fundamental band gap energy, 2.7 eV, whereas the extrapolation on the optical absorption gives the value of 3.3 eV. The DFT electronic band structure accompanied with DOS agreed with experimental data (O'Neil *et al*., 2010a). Structure, optical and electrical properties were further reported by O'Neil *et al*. (2010b). The calculated crystallographic information and electronic band structure were additionally probed to elucidate cationic distribution at 18*f* sites (Zhang and Wang, 2011).

Another studied topic is gas-sensing properties. Nanocrystalline $In_4Sn_3O_{12}$ shows thermal and chemical stability, which has a potential ability to be employed as gas sensors (Kemmler *et al*., 2012). Very recently, the composite of $In_4Sn_3O_{12}$/TeO2 nanoparticle was investigated for CO gas-sensing performance (Mirzaei *et al*., 2016).

To the best of my knowledge, the origin of high electrical conductivity in $In_4Sn_3O_{12}$ has not been clarified. The intrinsic oxygen vacancy might be one of the answers. As this phase is prepared at high temperature, it might be possible to lose oxygen because non-stoichiometric oxygen-deficient In_2O_3 was found at high temperatures (De Wit, 1977). The interesting point is that the calculated electronic band structures of $In_4Sn_3O_{12}$ (Figure 2.3(a)) (Zhang and Wang, 2011) is similar to that of famous TCOs, Sn-doped In_2O_3 mentioned earlier (Chapter 1, section 1.3, Figure 1.14). Regarding DOS of $In_4Sn_3O_{12}$, the bottom of conduction band is primarily constructed by the mix states of In 5*s*, Sn 5*s* and O 2*p* orbitals whereas the top of valence band is mainly constituted by In 4*d*, Sn 4*d* and O 2*p* orbitals (Figure 2.3(b)).

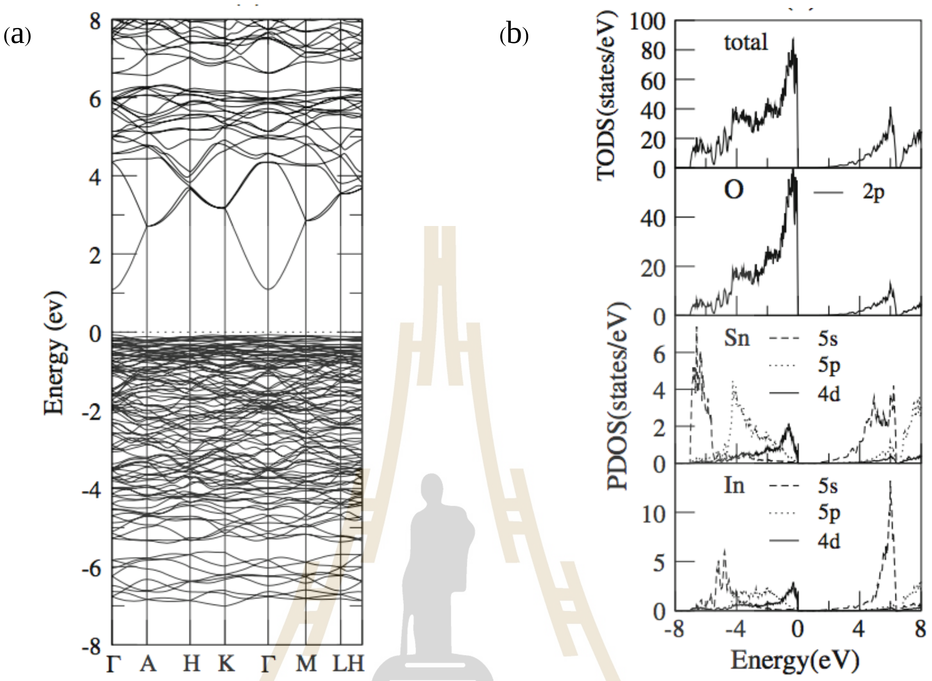

Figure 2.3 (a) The calculated electronic band structure and (b) DOS of $In_4Sn_3O_{12}$ (Zhang and Wang, 2011).

2.3 ZnO-based oxides

In general, ZnO can be crystallised into two primary forms of wurtzite (hexagonal) (Figure 2.4(a)) and zinc blende (cubic) (Figure 2.4(b)). Wurtzite is the most common form which is most thermodynamically stable at ambient conditions while zinc blende can be crystallised by using a substrate coated with cubic structure compound (Fierro, 2005). Besides, ZnO rocksalt exists but it is rather uncommon because it can be formed only under a relatively high pressure of about 10 GPa (Özgür *et al.*, 2005). ZnO with hexagonal wurtzite structure adopts space group $P6_3mc$ (Moore and Wang, 2006).

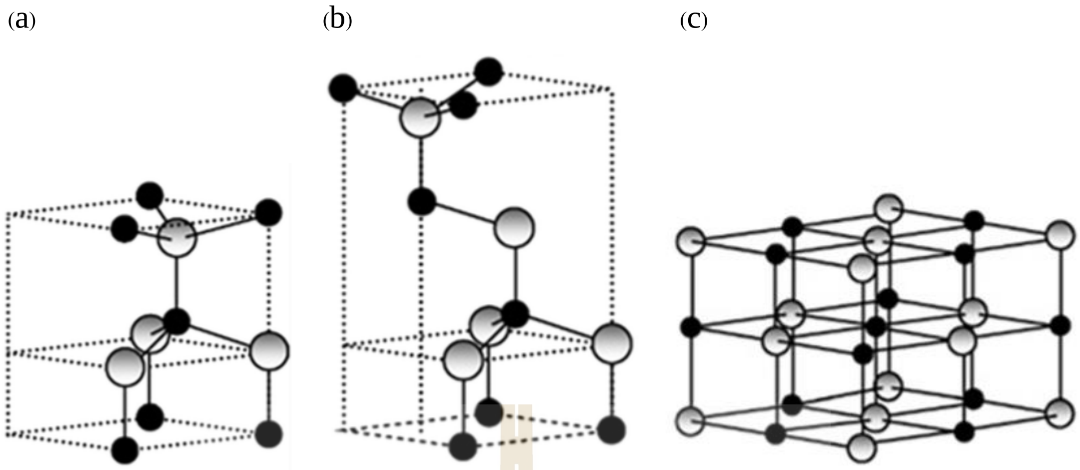

Figure 2.4 Crystal structures of ZnO: (a) hexagonal wurtzite, (b) cubic zinc blende and (c) cubic rocksalt.

A hexagonal wurtzite ZnO is widely investigated for many properties because of its attractive advantages, e.g., inexpensive, environmentally friendly (Schmidt-Mende and MacManus-Driscoll, 2007), high chemical and thermal stability. Moreover, its characteristics are varied which are useful for a wide range of applications. ZnO is well-known as an intrinsic n-type semiconductor. This makes it appealing to electrical applications. Moreover, it has wide direct band gap energy of 3.37 eV; this is useful for optical applications (Janotti and Van De Walle, 2009; Reynolds *et al*., 1999; Chen *et al*., 1998).

The combination of both electrical and optical characteristics produces unique materials named transparent conducting oxides (TCOs), which is a crucial component in the field of optoelectronic devices. The good orbital overlap between Zn and O results in a large conduction band dispersion (Figure 2.5), which provides low carrier effective mass and thus high carrier mobility (Hautier *et al*., 2004). ZnO shows a potential to be good TCOs and it has been extensively studied with doping, form/shape-modified like nanostructures such as nanowires, nanorods, nanobelts, etc. (Shrama *et al.*, 2014; Schmidt-Mende and MacManus-Driscoll, 2007).

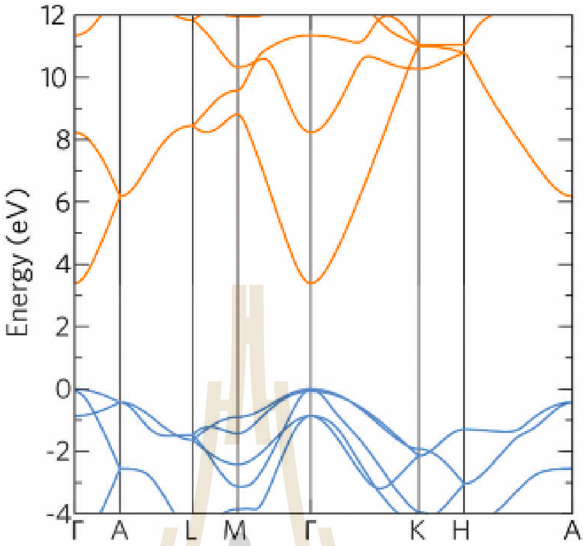

Figure 2.5 Band structure of ZnO calculated using HSE hybrid functional (Dixon *et al.*, 2017).

Furthermore, ZnO is widely investigated as a candidate in the field of photocatalysis. Its direct band gap energy is similar to that of TiO_2 (E_g = 3.2 eV), which is advantaged for the capability to absorb a wide scale of sunlight (Lee *et al.*, 2016). However, the band gap is too wide to have strong visible light absorption. This causes fast photo-generated charge recombination rate and thus lowers photocatalytic efficiency (Gomez-Solís *et al.*, 2015). Therefore, many approaches were attempted to improve photocatalytic properties of ZnO, for example, doping with cations/anions and mixing with other oxides (Subramanian *et al.*, 2001; Asahi *et al.*, 2001; Padmanabhan *et al.*, 2007; Mane *et al.*, 2005). These methods introduce impurity levels to ZnO band structure, which leads to the reduction of a band gap and consequently the inhibition of electron-hole recombination. The role of a cation and an anion in developing carrier charge separation is proposed as a mechanism described in Figure 2.6. Oxygen deficiency was reported to be a critical factor to increase the photocatalytic activity (Gomez-Solís *et al*., 2015). Furthermore, a polar plane plays a dramatic impact on enhancing the properties as it enriches the formation of oxygen vacancy (Li *et al*., 2008). Interestingly, nanostructured ZnO has become attractive because of short diffusion pathway and low reflectivity, which produce superior charge transfer performance and substantially improve photocatalytic performance (Wang *et al*., 2010).

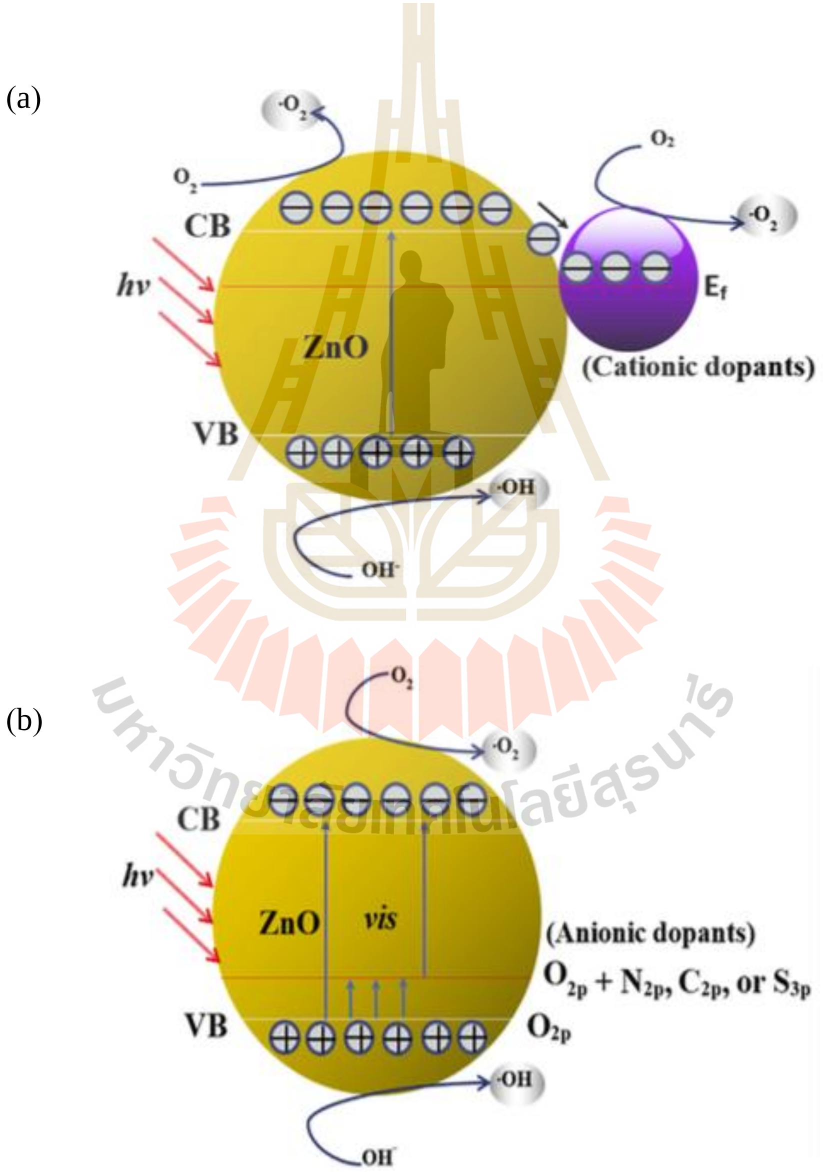

Figure 2.6 The proposed photocatalytic mechanism by (a) a cation and (b) an anion dopant on ZnO surface (Lee *et al*., 2016).

2.4 References

Asahi, R., Morikawa, T., Ohwaki, T., Aoki, K. and Taga, Y. (2001). Visible-Light Photocatalysis in Nitrogen-Doped Titanium Oxides. **Science.** 293: 269-271.

Bates, J. L., Griffin, C. W., Marchant, D. D. and Garnier, J. E. (1986). Electrical Conductivity, Seebeck Coefficient and Structure of In_2O_3-SnO_2. **American Ceramic Society Bulletin.** 65: 673-678.

Behr, G. and Krabbes, G. (1996). Abschlußbericht zum DFG-Förderprojekt Kr1241/1-1 und Be 1749/1-3," p. 67. Dresden.

Bizo, L. and Anghel, C. I. (2010). Physical Properties Predictions of Indium Based Solid Solution by Artificial Intelligence Techniques. **20th European Symposium on Computer Aided Process Engineering (ESCAPE20).**

Chen, Y., Bagnall, D. M., Koh, H., Park, K. Hiraga, K., Zhu, Z. and Yao, T. (1998). Plasma Assisted Molecular Beam Epitaxy of ZnO on c-Plane Sapphire**:** Growth and Characterization**. Journal of Applied Physics.** 84: 3912.

Choisnet, J., Bizo, L., Retoux, R., Hébert, S. and Raveau, B. (2004). New Transparent Conductors with the M_7O_{12} Ordered Oxygen-Deficient Fluorite Structure: From $In_4Sn_3O_{12}$ to $In_{5.5}Sb_{1.5}O_{12}$. **Journal of Solid State Chemistry.** 177: 3748-3751.

Choisnet, J., Bizo, L., Allix, L., Rosseinsky, M. and Raveau, B. (2007). Cation Ordering in the Fluorite-Like Transparent Conductors $In_{4+x}Sn_{3-2x}Sb_xO_{12}$ and In_6TeO_{12}. **Journal of Solid State Chemistry**. 180: 1002-1010.

De Wit, J. H. W. (1977). Structural Aspects and Defect Chemistry in In_2O_3. **Journal of Solid State Chemistry.** 20: 143-148.

Fierro, J. L. G. (2010). **Metal Oxides: Chemistry and Applications.** CRC Press, Boca Raton.

Frit, B. (1975). Structure Crystalline du Tellurate d'Indium In_2TeO_6. **Comptes Rendus Hebdomadaires des Seances de l'Academie des Sciences, Serie C.** 281: 769-772.

Gomez-Solís, C., Ballesteros, J. C., Torres-Martínez, L. M., Juarez-Ramírez, I., Torres, L. A. D., Zarazua-Morin, M. E. and Lee, S. W. (2015). Rapid Synthesis of ZnO Nano-Corncobs from Nital Solution and Its Application in the Photodegradation of Methyl Orange. **Journal of Photochemistry and Photobiology A: Chemistry.** 298: 49-54.

Hautier, G., Miglio, A., Waroquiers, D., Rignanese, G.-M. and Gonze, X. (2014). How Does Chemistry Influence Electron Effective Mass in Oxides? A High-Throughput Computational Analysis. **Chemistry of Materials.** 26: 5447-5485.

Heward, W. J. and Swenson, D. J. (2007). Phase Equilibria in the Pseudo-Binary In_2O_3-SnO_2 System. **Journal of Materials Science.** 42: 7135-7140.

Janotti. A. and Van de Walle, C. G. (2009). Fundamentals of Zinc Oxide as a Semiconductor. **Reports Progress Physics.** 72: 126501.

Kemmler, J. A., Pokhrel, S., Birkenstock, J., Schowalter, M., Rosenauer, A., Bârsan, N., Weimar, U. and Mädler, L. (2012). Quenched, Nanocrystalline $In_4Sn_3O_{12}$ High Temperature Phase for Gas Sensing Applications. **Sensors and Actuators B.** 161: 740-747.

Lee, K. M., Lai, C. W., Ngai, K. S. and Juan, J. C. (2016). Recent Developments of Zinc Oxide Based Photocatalyst in Water Treatment Technology: A Review. **Water Research.** 88: 428-448.

Li, G. R., Hu, T., Pan, G. L., Yan, T. Y., Gao, X. P. and Zhu, H. Y. (2008). Morphology-Function Relationship of ZnO: Polar Planes, Oxygen Vacancies, and Activity. **Journal of Physical Chemistry C.** 112: 11859-11864.

Mane, R. S., Lee, W. J., Pathan, H. M. and Han, S. H. (2005). Nanocrystalline TiO_2/ZnO Thin Films: Fabrication and Application to Dye-Sensitized Solar Cells, **Journal of Physical Chemistry B.** 109: 24254-24259.

Minami, T. Takeda, Y., Takata, S. and Kakumu, T. (1997). Preparation of Transparent Conducting $In_4Sn_3O_{12}$ Thin Films by DC Magnetron Sputtering. **Thin Solid Films.** 308-309: 13-18.

Minami, T. (1999). Transparent and Conductive Multicomponent Oxide Films Prepared by Magnetron Sputtering. **Journal of Vacuum Science & Technology** A. 17: 1765-1772.

Mirzaei, A., Park, S., Sun, G.-J., Kheel, H. and Lee, C. (2016). CO Gas Sensing Properties of $In_4Sn_3O_{12}$ and TeO_2 Composite Nanoparticle Sensors. **Journal of Hazardous Materials.** 305: 130-138.

Moore, D. and Wang, Z. L. (2006). Growth of Anisotropic One-Dimensional ZnS Nano- Structures. **Journal of Materials Chemistry.** 16 (40): 3898-3905.

Nadaud, N., Lequeux, N. and Nanot, M. (1998). Structural Studies of Tin-Doped Indium Oxide (ITO) and $In_4Sn_3O_{12}$. **Journal of Solid State Chemistry.** 135: 140-148.

Natansohn, S. (1968) The Synthesis and Structure of Rare-Earth and Indium Tellurate, R_2TeO_6. **Journal of Inorganic Nuclear Chemistry.** 30: 741-745.

Ohya, Y., Ito, T., Kaneko, M., Ban, T. and Takahashi, Y. (2000). Solid Solubility of SnO_2 in In_2O_3. **Journal of the Ceramic Society of Japan.** 108: 803-806.

O'Neil, D. H., Walsh, A., Jacobs, R. M. J., Kuznetsov, V. L., Egdell, R. G. and Edwards, P. P. (2010a). Experimental and Density-Functional Study of the Electronic Structure of $In_4Sn_3O_{12}$. **Physical Review B.** 81: 085110.

O'Neil, D. H., Kuznetsov, V. L., Jacobs, R. M. J., Jones, M. O. and Edwards, P. P. (2010b). Structural, Optical and Electrical Properties of $In_4Sn_3O_{12}$ Films Prepared by Pulsed Laser Deposition. **Materials Chemistry and Physics.** 123: 152-159.

Padmanabhan, S. C., Pillai, S. C., Colreavy, J., Balakrishanan, S., McCornak, D. E., Perova, T. S., Gun'ko, Y., Hinder, S. J. and Kelly, J. M. (2007). Synthesis and Thermal and Wetting Properties of Tin/Silver Alloy Nanoparticles for Low Melting Point Lead-Free Solders. **Chemistry of Materials.** 19: 4482-4485.

Pitschke, W., Werner, J., Behr, G. and Koumoto, K. (2000). Structure and Thermoelectric Properties of Me-Substituted $In_4Sn_3O_{12}$, Me = Y and Ti. **Journal of Solid State Chemistry.** 153: 349-356.

Redman, M. J., Binnie, W. P. and Mallio, W. J. (1971). Formation and Crystallography of Indium Tellurite, $In_2Te_3O_9$ and Indium Tellurate, In_2TeO_6. **Journal of the Less-Common Metals.** 23: 313-315.

Ren, C.-Y., Chiou, S.-H. and Choisnet, J. (2006). First-principles Calculations of the Electronic Band Structure of $In_4Sn_3O_{12}$ and In_5SnSbO_{12}.

Reynolds, D. C., Look, D. C., Jogai, B., Litton, C. W., Cantwell, G. and Harsch, W. C. (1999). Valence-Band Ordering in ZnO. **Physical Review B.** 60: 2340-2344.

Schmidt-Mende, L. and MacManus-Driscoll, J. L. (2007). ZnO-Nanostructures, Defects and Devices. **Materials Today.** 10: 40-48.

Shannon, R. D., Gillson, J. L. and Bouchard, R. J. (1977). Single Crystal Synthesis and Electrical Properties of $CdSnO_3$, Cd_2SnO_4, In_2TeO_6 and $CdIn_2O_4$. **Journal of Physics and Chemistry of Solids.** 38: 877-881.

Sharmaa, B.K., Khare, N. and Haranath, D. (2010). Photoluminescence Lifetime of Al-Doped ZnO Films in Visible Region. **Solid State Communications.** 150 (47-48): 2341-2345.

Shemirani, B. and Koffyberg, F. P. (1992). Semiconductivity and Band Gap of Tin-Doped Indium Tellurate. **Materials Research Bulletin.** 27: 693-698.

Siritanon, T., Sleight, A. W. and Subramanian, M. A. (2011). Compositionally Controlled Metal-Insulator Transition in $Tl_{2-x}In_xTeO_6$. **Journal of Solid State Chemistry.** 84: 877-880.

Starnek, C. R., Jiang, C., Uberuaga, B. P., Sickafus, K. E., Cleave, A. R. and Grimes, R. W. (2009). Predicted Structure and Stability of $A_4B_3O_{12}$ δ-Phase Compositions. **Physical Review B.** 80: 174101.

Subramanian, V., Wolf, P. V., Kamat, E. (2001). Semiconductor-Metal Composite Nanostructures. To What Extent Do Metal Nanoparticles Improve The Photo-Catalytic Activity of TiO_2 Films? **Journal of Physical Chemistry B.** 105: 11439-11446.

Wang, G., Yang, X., Qian, F., Zhang, J. Z. and Li, Y. (2010). Double-Sided CdS and CdSe Quantum Dot Co-Sensitized ZnO Nanowire Arrays for Photoelectrochemical Hydrogen Generation. **Nano Letters.** 10: 1088-1092.

Zhang, Y. G. and Wang, Y. X. (2011). Density-Functional Study of the Electronic Structure and Optical Properties of Transparent Conducting Oxides $In_4Sn_3O_{12}$ and $In_4Ge_3O_{12}$. **Journal of Electronic Materials.** 40: 1501-1505.

Zhou, T., Bhame, S. D., Guilmeau, E., Marinel, S. and Raveau, B. (2011). Enhanced Densification and Thermoelectric Performance of $In_4Sn_3O_{12}$ by Reactive Sintering in the In-Sn-Ga-O System. **Journal of the American Ceramic Society.** 94: 3733-3737.

Özgür, Ü., Alivov, Ya. I., Liu, C., Teke, A., Reshchikov, M. A., Doğan, S., Avrutin, V., Cho, S.-J. and Morkoç, H. (2005). A Comprehensive Review of ZnO Materials and Devices**. Journal of Applied Physics.** 98: 041301.

CHAPTER III

INVESTIGATION ON CRYSTAL STRUCTURES, OPTICAL PROPERTIES AND BAND STRUCTURE CALCULATIONS OF $In_{2-x}M_xTeO_6$ (M = Ga, Bi, La)

3.1 Abstract

The study of structure, optical properties and band structure of M substituted-In_2TeO_6 (M = Ga^{3+}, Bi^{3+}, La^{3+}) is presented. Solubility limit of each cation is different varying from 10% for La^{3+} to 20% for Ga^{3+} and 25% for Bi^{3+}. Both XANES and XPS confirm the oxidation states of Bi^{3+} and Te^{6+}. Crystallographic data of bond lengths and bond angles suggest no significant distortion of M-O_6 octahedra for all samples; however, the stereoactive $6s^2$ lone-pair electrons in Bi cause In/Bi cation in In/Bi-O_6 to shift toward one edge of the octahedra. The band structure calculation was useful to clarify that the fundamental band gap energies of all series originate from the direct allowed transition. Interestingly, Bi greatly influences the conduction band dispersion and Bi 6s state additionally contributes at the valence band maximum, while the valence band of other M-doped and un-doped samples are mainly O 2p and In 4d in character. All compounds similarly exhibit photoluminescence properties. The strong PL peak mainly originated from the near band edge transition and the broad peak from Te^{6+}-O charge transfer are observed in all samples.

3.2 Introduction

Ternary metal tellurates with the general formula M_2TeO_6, when M is a trivalent cation, crystallise in different crystal structures: trirutile ($P4_2/mnm$), Na_2SiF_6-type (P_{321}) and orthorhombic La_2TeO_6-type ($P2_12_12_1$). The size of M^{3+} in M_2TeO_6 plays an important role in its crystal structure. Trirutile structure is formed when M, such as Cr, Fe, Rh (Bayer, 1969), Ga (Berand and Range, 1994; US patent. 6 124 057, 2000) and Al (US patent. 6 124 057, 2000), has ionic radii in the range of 0.5-0.7 Å. The bigger M cations (r = 0.745-0.87 Å) like In(Malone *et al.*, 1969), Lu (Malone *et al.*, 1969; Kasper, 1969) and Sc (Höss and Schleid, 2007; Pankajavalli *et al.*, 2013) prefer Na_2SiF_6-type structure. The even bigger M cation (>0.87 Å), such as Gd, La, Sm and Y (Llanosa *et al.*, 2009), usually form La_2TeO_6-type structure. Nevertheless, there are some exceptions. Na_2SiF_6-type structure is also formed for Tl^{3+} (0.885 Å) (Bernard *et al.*, 1975), although the size of Tl^{3+} drops into the last category. Both Na_2SiF_6-type and La_2TeO_6-type structure could be formed with Yb^{3+} as its size (0.868 Å) is in the borderline (Natansohn, 1968; Tröemel *et al.*, 1987). Additionally, Bi_2TeO_6 prefers a layered structure with orthorhombic lattice (*Cmca*) (Udovic *et al.*, 2004) because of the constituent 6*s* stereoactive lone-pair electrons.

Indium tellurium oxide (In_2TeO_6) was first prepared from In_2O_3 and H_6TeO_6 by solid state reaction (Natansohn, 1968). Redman *et al*. later found that In_2TeO_6 is formed after heating $In_2Te_3O_9$ at temperature higher than 650 °C in air (Redman *et al.*, 1971). Two space groups have been reported for In_2TeO_6 as P_{321} (Frit, 1975) and $P\bar{3}m_1$ (Shannon *et al.*, 1977). There are only few reports on electronic properties of In_2TeO_6 related compounds. Here, the stoichiometric In_2TeO_6 is insulator (Shemirani and Koffyberg, 1992), oxygen-deficient In_2TeO_{6-x} behaves as a degenerate semiconductor (Shannon *et al.*, 1977). $In_2Te_{6-x}Re_xO_6$ is also reported to be a semiconductor having lower conductivity (Shannon *et al.*, 1977). Few elements have been used to substitute In in In_2TeO_6 in attempt to create extrinsic semiconductors. Only Sn and Zr doped In_2TeO_6 have been reported to show n-type semiconducting behaviour. On the other hand, Zn-doped In_2TeO_6 is insulating and there is no report of p-type semiconducting behaviour for doped-In_2TeO_6 samples (Shemirani and Koffyberg, 1992). Recently, compositionally controlled metal insulator transition was observed in $Tl_{2-x}In_xTe_xO_6$ solid solution (Siritanon *et al.*, 2011). As the optical band gap of In_2TeO_6 is large and some compounds in this family have been reported to show semiconducting behaviour, it might be possible to design transparent conducting oxides (TCOs) based on In_2TeO_6. In addition, the theoretical study, derived from the density functional theory (DFT), suggests that In_2TeO_6 has the capability to be a good n-type TCO considering its low effective mass, which result in high carrier mobility. On the other hand, the relatively large E_g (slightly lower than 3 eV) could result in little light absorption (Hautier *et al.*, 2014). Information on the structure, electronic and optical properties of the related compounds are, therefore, the important keys to develop these materials for future applications.

In the article, we report the preparation, structural studies, optical properties and electronic band structure calculations of Ga, Bi and La-doped In_2TeO_6. The Rietveld refinement is carried out to solve the crystallographic information including cell parameters, cell volumes, bond lengths and occupancies. Oxidation states of cations are investigated by X-ray absorption near-edge spectroscopy (XANES) and X-ray photoelectron spectroscopy (XPS) technique. In addition, scanning electron microscopy coupled with energy dispersive X-ray spectroscopy (SEM-EDS) is used to study morphology, particle size and elemental composition of the samples. The optical properties are studied via UV-Visible spectroscopy and photoluminescence (PL) experiment to explore the absorption and re-emitting phenomena. Additionally, the electronic band structure calculation supplies more information about electronic structure of the compounds. The obtained results are used to explain the relationships between structure, composition and properties of the materials.

3.3 Experimental

Pure phase of all polycrystalline samples were obtained by conventional solid state reaction. High purity of In_2O_3 (Sigma-Aldrich, 99.99%), TeO_2 (Sigma-Aldrich, 99+%), Bi_2O_3 (Acros organic, 99.9%), Ga_2O_3 (Sigma-Aldrich, 99.99%) and La_2O_3 (Acros organic, 99.99%) were used as starting materials. La_2O_3 was preheated at 850 °C prior to weighting. In the procedure, the stoichiometric mixtures were heated at 700 °C with different holding time and atmosphere. $In_{2-x}Bi_xTeO_6$ ($x = 0, 0.1, 0.2, 0.3, 0.4, 0.5$), $In_{2-x}Ga_xTeO_6$ ($x = 0, 0.1, 0.2, 0.3, 0.4$) and $In_{2-x}La_xTeO_6$ ($x = 0, 0.1, 0.2$) were heated for 12 hours in air, 12-24 hours in air and 4 hours in O_2, respectively. To solve the issue of Te volatilisation in In_2TeO_6 and $In_{2-x}Ga_xTeO_6$, extra TeO_2 was added and the samples were washed with hot 50% v/v HCl to remove the excess TeO_2 after heating.

To identify the phase purity, powder X-ray diffraction (XRD) measurement was carried out by a Bruker D2 Phaser diffractometer with Cu Kα radiation ($\lambda = 1.5406$ Å). High quality XRD patterns were collected in the 2-theta range of 12-120° with an increment of 0.02° by a scan rate of 2s/step. Rietveld refinement, using TOPAS software, was applied to collect crystallographic data. Scanning electron microscopy (SEM) images were taken using a FEI quanta 450 SEM with a magnification of 24,000, operated with the accelerating voltage of 20 kV and working distance of 9.9 mm. Energy dispersive X-ray spectroscopy (EDS), using the Oxford instrument (model X-Max 50 mm) was utilised with area analysis. X-ray absorption near-edge structure (XANES) and

X-ray photoelectron spectroscopy (XPS) were performed at the SUT-NANOTEC-SLRI XAS Beamline (BL5.2) and the SUT-NANOTEC-SLRI XPS Beamline (BL5.1), the SUT-NANOTEC-SLRI joint research facility, Synchrotron Light Research Institute (SLRI), Thailand (electron energy of 1.2 GeV, beam current of 80-120 mA). XANES spectra of Bi M_5-edge and Te L_3-edge were obtained by using InSb (111) and Ge (220) crystal, respectively. The spectra were normalised by the ATHENA program prior to the data analysis. XPS spectra of Bi $4f_{7/2}$, Te $3d_{5/2}$ and O 1s were recorded by a PHI5000 VersaProbe II XPS instruments (ULVAC-PHI, Japan) with monochromatic X-ray of Al K_α (1486.6 eV). The C 1s peaks at 284.8 eV were used as a reference for binding energy calibration. Optical diffuse reflectance spectroscopy (DRS) was probed by an Agilent UV-Vis-NIR spectrophotometer (model Cary 5000). The scan wavelength range of 200-800 nm with the double beam mode was used to collect diffuse reflectance (%R) spectra. Photoluminescence measurement was carried out utilising an AVANTES AvaSpec-2048TEC-USB2-2 spectrometer with the excitation LED light source of 255 nm. Electronic structures were calculated based on density functional theory (DFT) by using the VASP code (Kresse and Furthmüller, 1996). The Perdew, Burke, Ernzerhof (PBE) (Perdew *et al.*, 1996) exchange-correlation function implemented with the projector augmented wave method (PAW) (Blöchl, 1994; Kresse and Joubert, 1999) was employed. The 2×2×1 supercell, comprising of 108 atoms, was used to study $In_{2-x}M_xTeO_6$ where M_x = $Ga_{0.417}$, $La_{0.250}$ and $Bi_{0.500}$. The compounds with different compositions were modeled by placing a number of M atoms randomly on In-site (24 sites) according to the specified concentration. The cutoff energy was set at 520 eV and a Γ-centered 2×2×9 Monkhorst-Pack *k*-mesh was used for the Brillouin zone integrations. Structural relaxation was performed until the force on each ion is below 0.01 eV/Å. The optimised lattice parameter *a* and *c* of In_2TeO_6 are 9.07 Å and 4.93 Å which are in good agreement with the cell parameters reported in Figure 3.3. The electronic structures, obtained from supercell calculations, were unfolded onto the high symmetry paths as defined in the first Brillouin zone of the primitive cell (Tomić *et al.*, 2014).

3.4 Results and discussion

3.4.1 Crystal structure

In_2TeO_6 has hexagonal Na_2SiF_6-type structure (P_{321}). The structure mainly consists of the three-dimensional corner sharing network of InO_6 octahedra (Figure 3.1). The octahedral units of Te are not connected with each other but connected to InO_6 units by edge sharing.

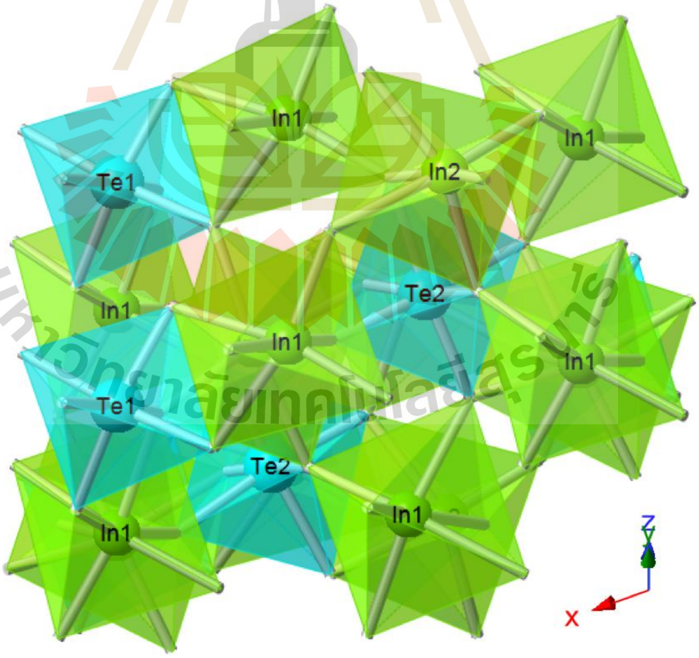

Figure 3.1 Crystal structure of ideal In_2TeO_6.

Only Sn and Tl have been reported to substitute In (Shemirani and Koffyberg, 1992; Siritanon *et al.*, 2011) in In_2TeO_6. In this work, In has been successfully substituted by Ga, Bi and La. XRD diffraction patterns of entire series confirm the formation of solid solutions, as all diffractions can be indexed as In_2TeO_6 phase (PDF77-2044) (Figure 3.2). Elemental compositions, obtained from EDS study, agree well with the nominal ones. The solubility limits of solid solutions $In_{2-x}M_xTeO_6$ with different M are different; $In_{2-x}Ga_xTeO_6$ (x = 0-0.40), $In_{2-x}Bi_xTeO_6$ (x = 0-0.50) and $In_{2-x}La_xTeO_6$ (x = 0-0.20) single phase can be obtained and the samples with higher x content contain some impurities. Therefore, the solubility limits of Ga, Bi and La are 20%, 25% and 10%, respectively. The incomplete solid solution is expected as Ga_2TeO_6, Bi_2TeO_6 and La_2TeO_6 are known to have different structures.

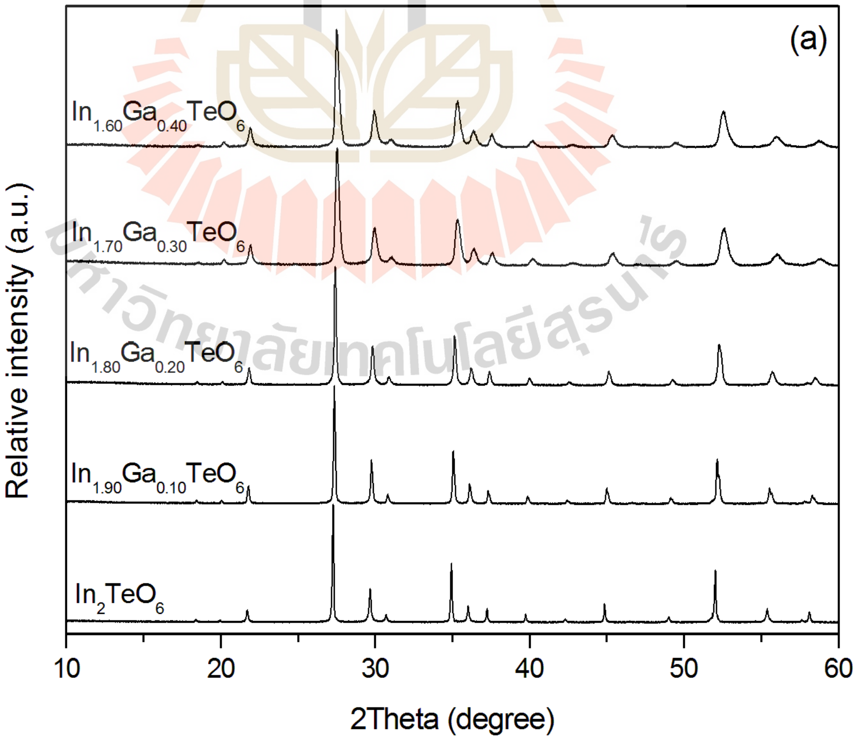

Figure 3.2 X-ray diffraction patterns of (a) $In_{2-x}Ga_xTeO_6$ (x = 0-0.40), (b) $In_{2-x}Bi_xTeO_6$ (x = 0-0.50) and (c) $In_{2-x}La_xTeO_6$ (x = 0-0.20).

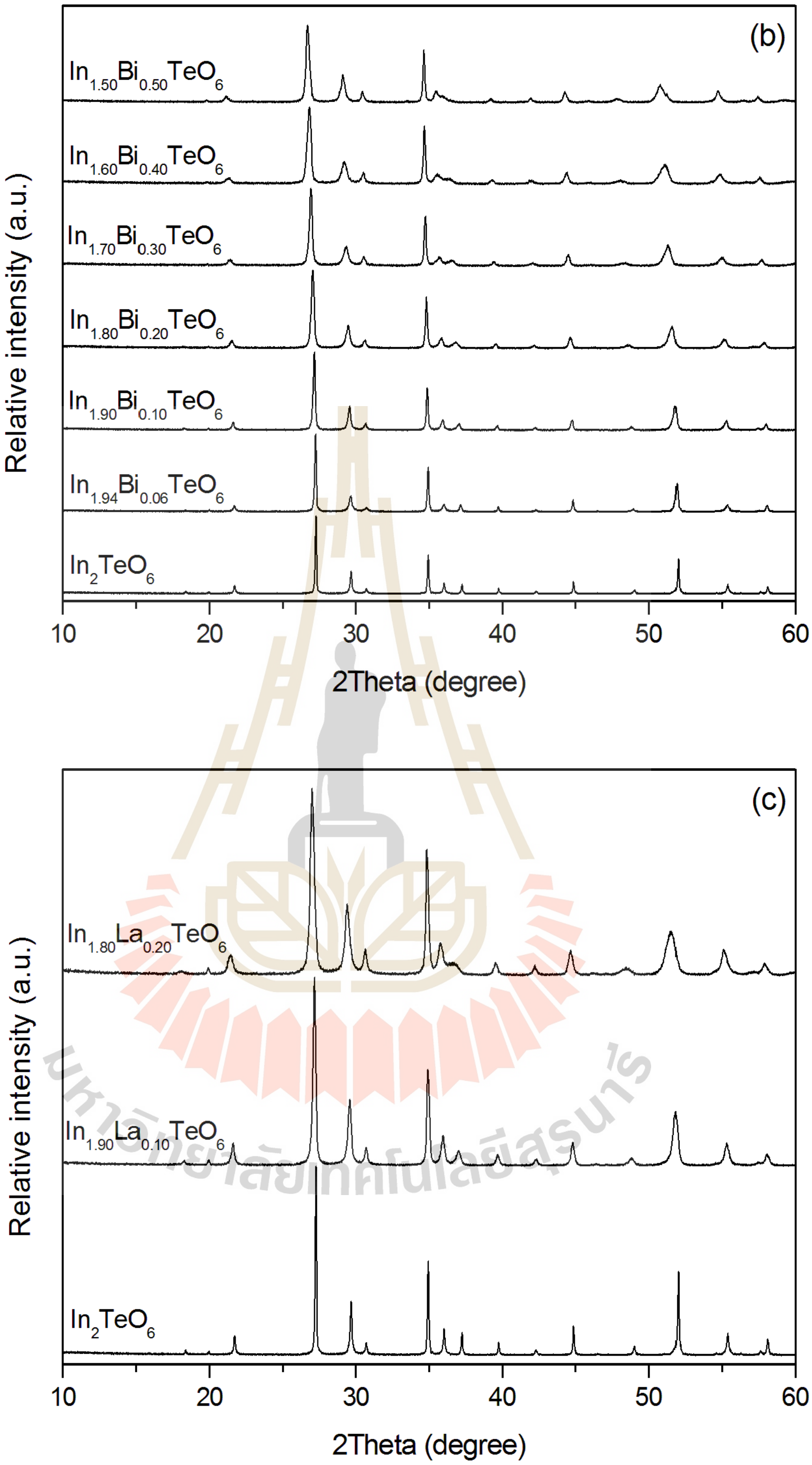

Figure 3.2 X-ray diffraction patterns of (a) $In_{2-x}Ga_xTeO_6$ (x = 0-0.40), (b) $In_{2-x}Bi_xTeO_6$ (x = 0-0.50) and (c) $In_{2-x}La_xTeO_6$ (x = 0-0.20) (Continued).

Cell parameters of the samples vary linearly with doping content, as shown in Figure 3.3. Ga^{3+} (r = 0.62 Å) is smaller than In^{3+} (r = 0.80 Å) thus the cell parameters decrease when Ga content is increased. On the other hand, substituting Bi and La in In_2TeO_6 increase the cell parameters. La is well known to be La^{3+} (r = 1.032 Å) in oxides which is larger than In^{3+}. On the other hand, Bi can be in both +3 and +5 state in oxides (Udovic *et al*., 2004; Egorysheva *et al*., 2015; Fujimoto, 2010). Nevertheless, the larger cell parameters in Bi-substituted samples suggest that it is in 3+ ($r_{Bi^{3+}}$ = 1.03 Å) rather than 5+ ($r_{Bi^{5+}}$ = 0.76 Å) in this case (Shannon and Prewitt, 1969; Shannon, 1976).

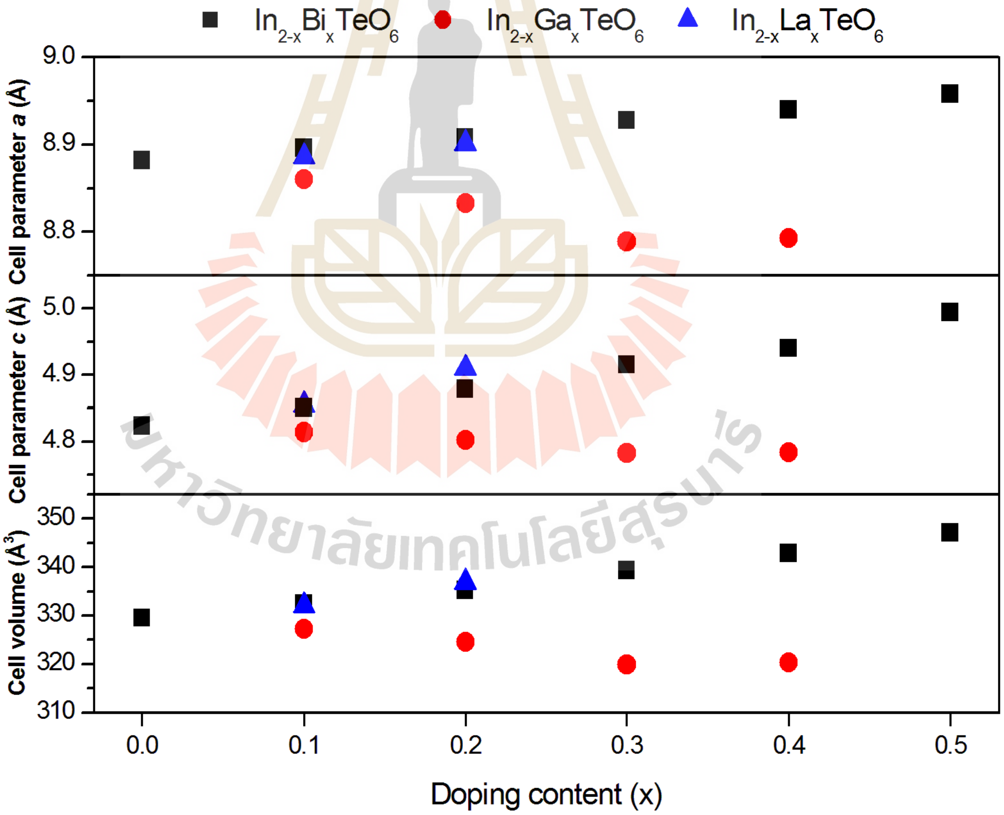

Figure 3.3 Cell parameters *a*, *c* and cell volume of $In_{2-x}Ga_xTeO_6$ (red circle), $In_{2-x}Bi_xTeO_6$ (black square) and $In_{2-x}La_xTeO_6$ (blue triangle).

In additions, X-ray peak broadening is observed in all cases. In general, a peak broadening is a result of crystallite size or crystallite strain when instrumental error is ignored (Murty *et al*., 2013). The broadening resulted from the first factor usually occurs with a crystallite size in nanoscale (<100 nm). In our cases, SEM images, as shown in Figure 3.4, confirm that the particle size of the samples are large so that the broadening should come mostly from crystallite strain. While the crystal lattice can contain both homogeneous and inhomogeneous strain, the homogeneous strain only causes the peak position to shift without changing the peak profile. On the other hand, inhomogeneous or lattice strain is produced when atoms with very different sizes occupy the same site resulting in lattice plane distortion (Li *et al*., 2011). This lattice strain is reasonable in our samples as the difference in ionic size between each dopant and In^{3+} is greater than 20%. This effect becomes more obvious in heavily doped samples.

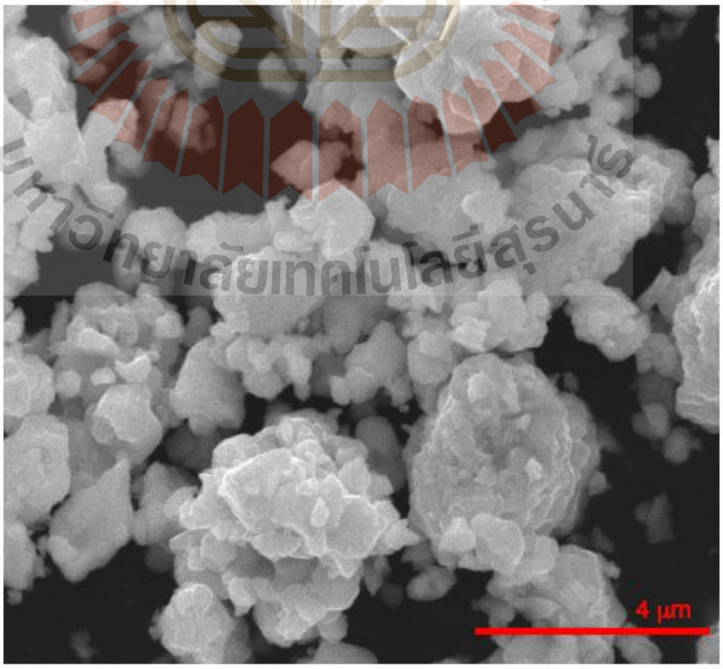

Figure 3.4 SEM image of $In_{1.90}Bi_{0.10}TeO_6$.

In additions, X-ray peak broadening is observed in all cases. In general, a peak broadening is a result of crystallite size or crystallite strain when instrumental error is ignored (Murty *et al*., 2013). The broadening resulted from the first factor usually occurs with a crystallite size in nanoscale (<100 nm). In our cases, SEM images, as shown in Figure 3.4, confirm that the particle size of the samples are large so that the broadening should come mostly from crystallite strain. While the crystal lattice can contain both homogeneous and inhomogeneous strain, the homogeneous strain only causes the peak position to shift without changing the peak profile. On the other hand, inhomogeneous or lattice strain is produced when atoms with very different sizes occupy the same site resulting in lattice plane distortion (Li *et al*., 2011). This lattice strain is reasonable in our samples as the difference in ionic size between each dopant and In^{3+} is greater than 20%. This effect becomes more obvious in heavily doped samples.

The refined parameters and crystallographic data are summarised in Table 3.1 and 3.2, respectively. In addition, the examples of Rietveld refinement plot are given in Figure 3.5. In the refinement, the modified Thompson-Cox-Hastings pseudo-Voigt "TCHZ" peak type is utilised for Bi and La-doped samples, while PearsonVII peak type is used to refine the Ga-dopes series. Anisotropic refinement model is applied in lattice strain peak broadening but no preferred orientation is included. Although there are two distinct crystallographic sites for In in In_2TeO_6, both Bi and La prefer to occupy In1 site. Attempts to refine Bi and La in In1 and In2 sites simultaneously result in zero or slightly negative occupancies at In2 thus all Bi and La are fixed at In1 site. On the other hand, Ga occupancies were refined on both sites and the refined occupancies indicate that Ga was distributed in both In1 and In2. In all cases, the overall occupancies of substituting cations were fixed at the nominal values, which are confirmed based on the EDS technique. The equivalent isotropic thermal parameters, $B_{eq.}$, are fixed to the values obtained from crystallographic information file (CIF). Attempts to refine the thermal parameters result in negative values in some cases as the parameters are strongly correlated with each other (Ozawaa *et al*., 2004).

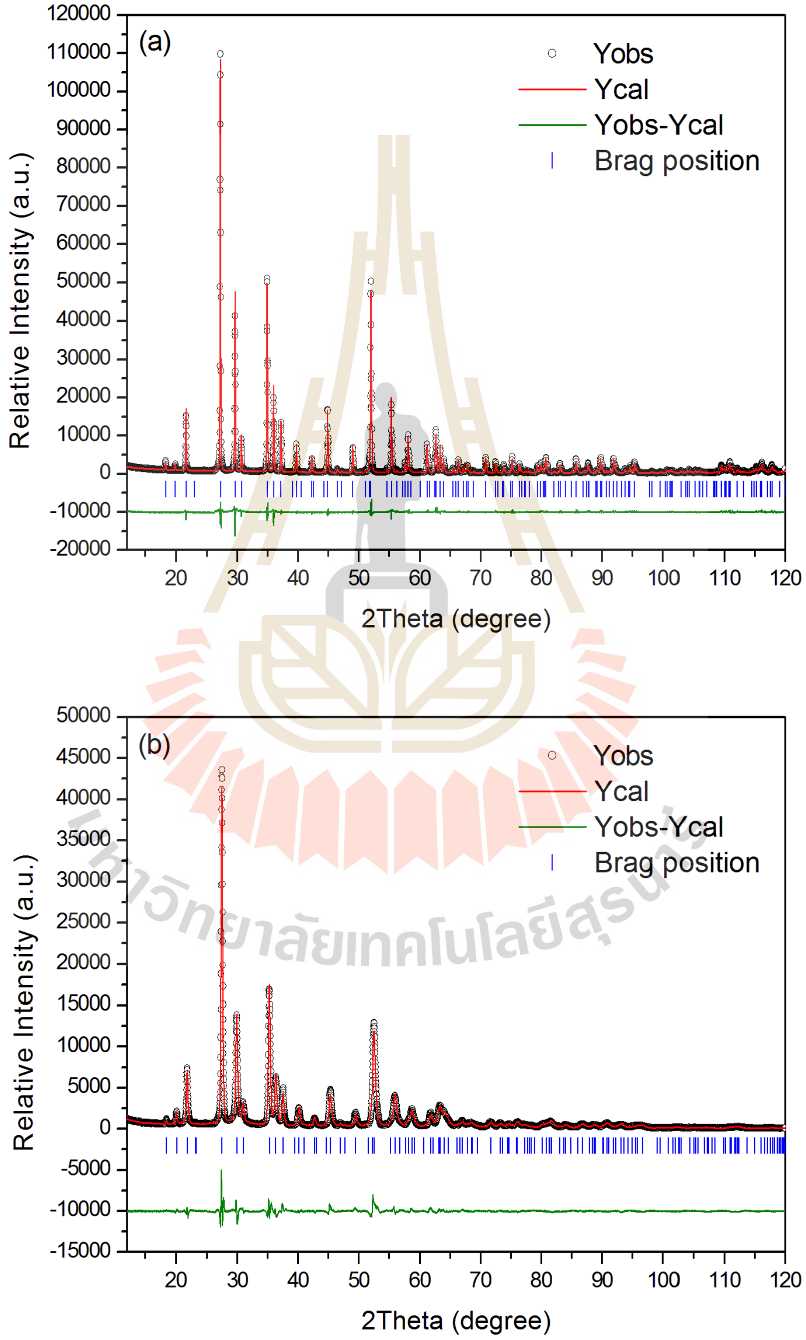

Figure 3.5 Rietveld refinement plots of (a) In_2TeO_6, (b) $In_{1.60}Ga_{0.40}TeO_6$, (c) $In_{1.50}Bi_{0.50}TeO_6$ and (d) $In_{1.80}La_{0.20}TeO_6$.

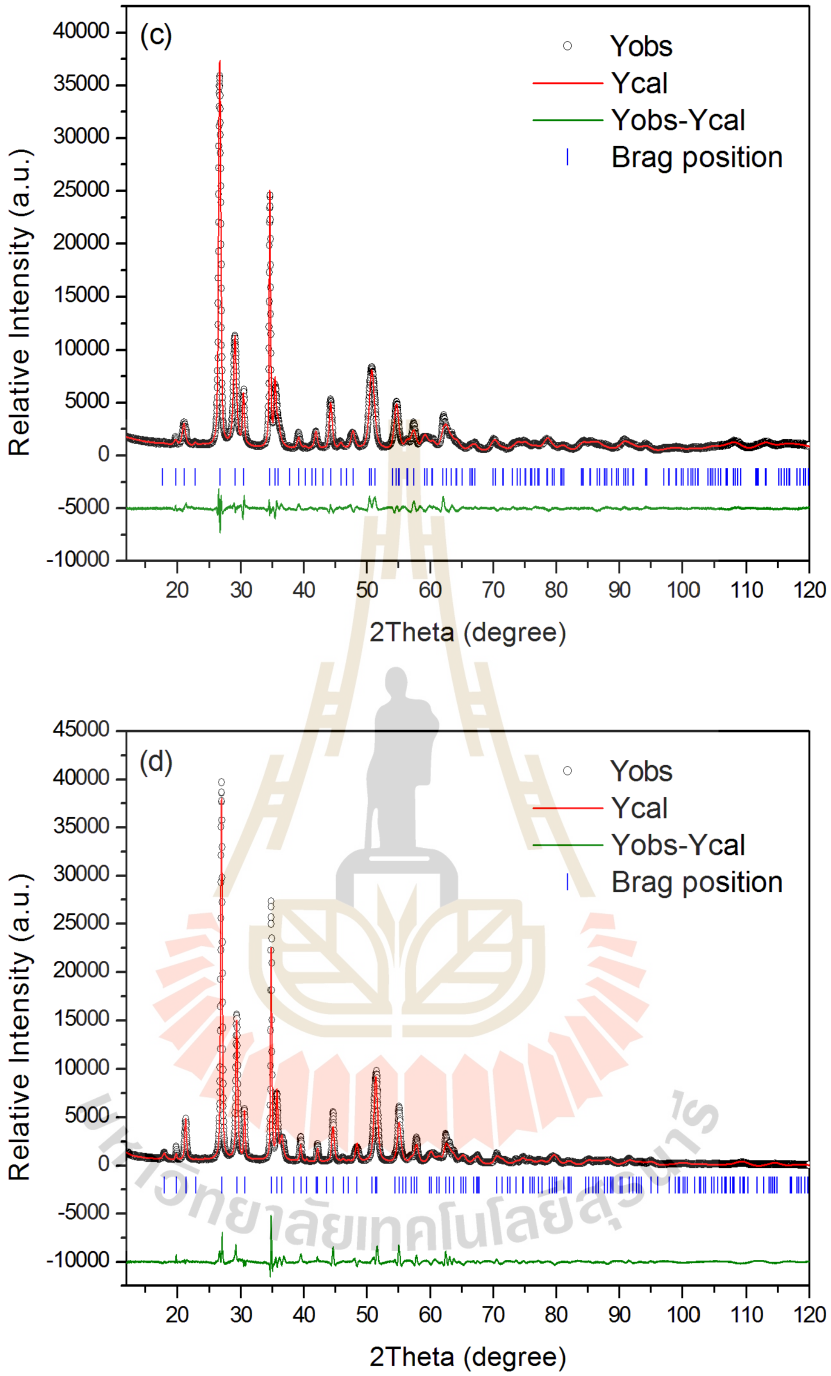

Figure 3.5 Rietveld refinement plots of (a) In_2TeO_6, (b) $In_{1.60}Ga_{0.40}TeO_6$, (c) $In_{1.50}Bi_{0.50}TeO_6$ and (d) $In_{1.80}La_{0.20}TeO_6$ (Continued).

Table 3.1 Rietveld refinement parameters of $In_{2-x}Ga_xTeO_6$ (x = 0, 0.20, 0.40), $In_{2-x}Bi_xTeO_6$ (x = 0, 0.10, 0.30, 0.50) and $In_{2-x}La_xTeO_6$ (x = 0, 0.10, 0.20).

	a (Å)	c (Å)	V (Å^3)	%R_{exp}	%R_p	%R_{wp}
In_2TeO_6	8.88211(5)	4.82304(4)	329.529(5)	2.73	7.68	9.91
$In_{1.80}Ga_{0.20}TeO_6$	8.8332(2)	4.8025(2)	324.52(2)	3.158	9.222	14.632
$In_{1.60}Ga_{0.40}TeO_6$	8.7943(4)	4.7830(3)	320.36(4)	3.177	8.571	11.164
$In_{1.90}Bi_{0.10}TeO_6$	8.8958(2)	4.8499(1)	332.38(2)	2.659	7.149	9.591
$In_{1.70}Bi_{0.30}TeO_6$	8.9278(3)	4.9149(3)	339.26(3)	2.61	7.563	10.126
$In_{1.50}Bi_{0.50}TeO_6$	8.9581(5)	4.9941(4)	347.07(5)	2.491	6.569	8.581
$In_{1.90}La_{0.10}TeO_6$	8.8863(4)	4.8550(3)	332.02(3)	3.103	11.559	15.71
$In_{1.80}La_{0.20}TeO_6$	8.9012(5)	4.9096(4)	336.88(5)	3.113	10.987	15.141

Table 3.2 Crystallographic data of $In_{2-x}Ga_xTeO_6$ (x = 0, 0.20, 0.40), $In_{2-x}Bi_xTeO_6$ (x = 0, 0.10, 0.30, 0.50) and $In_{2-x}La_xTeO_6$ (x = 0, 0.10, 0.20).

Atom	Site	*x*	*y*	*z*	Occupancy	$B_{eq.}$ (Å^2)
In_2TeO_6						
In1	3*e*	0.6305(2)	0	0	1	0.49
In2	3*f*	0.2943(2)	0	1/2	1	0.44
Te2	2*d*	1/3	2/3	0.5023(28)	1	0.25
O1	6*g*	0.0906(33)	0.8744(37)	0.7707(15)	1	0.93
O2	6*g*	0.4584(40)	0.5835(42)	0.7494(20)	1	2.43
O3	6*g*	0.2142(31)	0.7620(27)	0.2723(19)	1	1.04
$In_{1.80}Ga_{0.20}TeO_6$						
In1/Ga	3*e*	0.6316(3)	0	0	0.854(16)/0.146(16)	0.49
In2/Ga	3*f*	0.2939(4)	0	1/2	0.946(16)/0.054(16)	0.44
Te2	2*d*	1/3	2/3	0.5162(14)	1	0.25
O1	6*g*	0.1072(41)	0.8751(42)	0.7933(30)	1	0.93
O2	6*g*	0.4681(52)	0.5914(52)	0.7713(37)	1	2.43
O3	6*g*	0.2286(50)	0.7669(33)	0.2620(33)	1	1.04

Table 3.2 Crystallographic data of $In_{2-x}Ga_xTeO_6$ (x = 0, 0.20, 0.40), $In_{2-x}Bi_xTeO_6$ (x = 0, 0.10, 0.30, 0.50) and $In_{2-x}La_xTeO_6$ (x = 0, 0.10, 0.20) (Continued).

Atom	Site	*x*	*y*	*z*	Occupancy	$B_{eq.}$ (Å^2)
$In_{1.60}Ga_{0.40}TeO_6$						
In1/Ga	3*e*	0.6302(4)	0	0	0.846(13)/0.154(13)	0.49
In2/Ga	3*f*	0.3004(4)	0	1/2	0.754(13)/0.246(13)	0.44
Te2	2*d*	1/3	2/3	0.5106(18)	1	0.25
O1	6*g*	0.0933(39)	0.8604(40)	0.7755(24)	1	0.93
O2	6*g*	0.4576(51)	0.5643(45)	0.7519(28)	1	2.43
O3	6*g*	0.2430(43)	0.7562(29)	0.2301(30)	1	1.04
$In_{1.90}Bi_{0.10}TeO_6$						
In1/Bi	3*e*	0.6293(2)	0	0	0.9/0.1	0.49
In2	3*f*	0.2932(2)	0	1/2	1	0.44
Te2	2*d*	1/3	2/3	0.5090(17)	1	0.25
O1	6*g*	0.0933(30)	0.8828(40)	0.7778(21)	1	0.93
O2	6*g*	0.4537(33)	0.5771(46)	0.7506(27)	1	2.43
O3	6*g*	0.2126(35)	0.7632(26)	0.2934(24)	1	1.04
$In_{1.70}Bi_{0.30}TeO_6$						
In1/Bi	3*e*	0.6283(2)	0	0	0.7/0.3	0.49
In2	3*f*	0.2917(3)	0	1/2	1	0.44
Te2	2*d*	1/3	2/3	0.5106(20)	1	0.25
O1	6*g*	0.1013(25)	0.8854(39)	0.7699(32)	1	0.93
O2	6*g*	0.4574(27)	0.5739(42)	0.7544(37)	1	2.43
O3	6*g*	0.2136(29)	0.7620(27)	0.3145(38)	1	1.04
$In_{1.50}Bi_{0.50}TeO_6$						
In1/Bi	3*e*	0.6255(2)	0	0	0.5/0.5	0.49
In2	3*f*	0.2921(3)	0	1/2	1	0.44
Te2	2*d*	1/3	2/3	0.5122(22)	1	0.25
O1	6*g*	0.1065(27)	0.8868(32)	0.7641(40)	1	0.93
O2	6*g*	0.4677(26)	0.5821(38)	0.7505(46)	1	2.43
O3	6*g*	0.2261(27)	0.7731(24)	0.3221(45)	1	1.04

Table 3.2 Crystallographic data of $In_{2-x}Ga_xTeO_6$ (x = 0, 0.20, 0.40), $In_{2-x}Bi_xTeO_6$ (x = 0, 0.10, 0.30, 0.50) and $In_{2-x}La_xTeO_6$ (x = 0, 0.10, 0.20) (Continued).

Atom	Site	*x*	*y*	*z*	Occupancy	$B_{eq.}$ (Å^2)
$In_{1.90}La_{0.10}TeO_6$						
In1/La	3*e*	0.6340(3)	0	0	0.9/0.1	0.49
In2	3*f*	0.2874(3)	0	1/2	1	0.44
Te2	2*d*	1/3	2/3	0.5249(12)	1	0.25
O1	6*g*	0.0906(26)	0.8685(28)	0.7750(37)	1	0.93
O2	6*g*	0.4497(35)	0.5760(39)	0.7497(45)	1	2.43
O3	6*g*	0.2231(33)	0.7718(35)	0.3122(41)	1	1.04
$In_{1.80}La_{0.20}TeO_6$						
In1/La	3*e*	0.6314(4)	0	0	0.8/0.2	0.49
In2	3*f*	0.2880(4)	0	1/2	1	0.44
Te2	2*d*	1/3	2/3	0.4818(14)	1	0.25
O1	6*g*	0.1058(42)	0.8840(47)	0.7635(34)	1	0.93
O2	6*g*	0.4542(54)	0.5969(52)	0.7257(39)	1	2.43
O3	6*g*	0.2187(40)	0.7799(36)	0.3060(43)	1	1.04

$B_{eq.}$ = equivalent isotropic thermal parameters

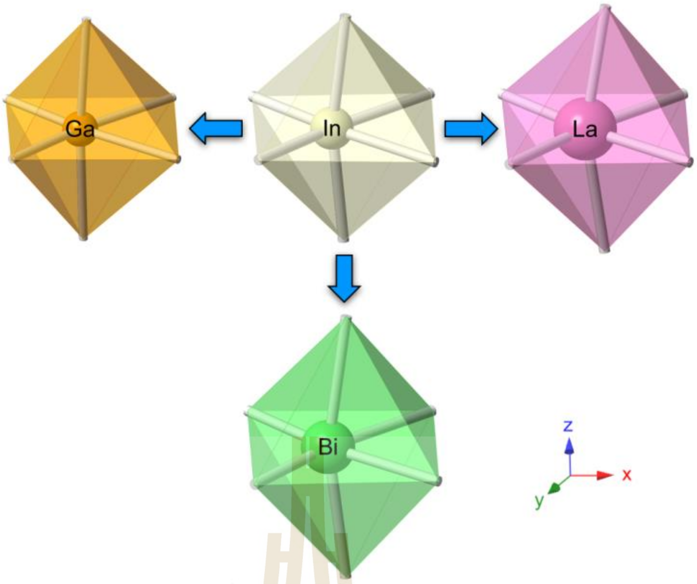

Figure 3.6 Schematic diagram of an M-O_6 octahedron for $In_{2-x}M_xTeO_6$ when M_x = $Ga_{0.40}$, $Bi_{0.50}$ and $La_{0.20}$.

The refined crystallographic data is used to calculate bond lengths as summarised in Table 3.3. In Bi and La series, the average In1-O bond length, where Bi and La atoms reside, is extended by the corresponding fractions indicating that the average octahedral units are enlarged. On the other hand, the average In2-O bond length tends to shrink to maintain the crystal structure stability. Changes of bond lengths in Ga substituted samples depend on the Ga content. $In_{2-x}Ga_xTeO_6$ samples with $x \leq 2$ show an increase in both In1-O and In2-O distances. On the other hand, the trend is not as clear in samples with $x > 0.2$. Using the refined crystallographic data, figures depicting the environment of cation(s) in In1 sites are created (Figure 3.6). In general, the size of the octahedron represents its contents. The smaller substituting cation results in a smaller octahedron and the bigger substituting cation results in a larger one. Although both Bi and La are bigger than In, the local environment of these two cations are different. The metal cation in Bi doped samples clearly shifts from the prior position toward one edge of the octahedron. This is most probably a result of Bi 6s^2 electrons which can now occupy more space on the opposite edge of the octahedron. The similar phenomenon is also reported in some works (Retuerto *et al.*, 2013; Singh *et al.*, 2012; Park and Woodward, 2000). The same electrons are also responsible for a layered structure in Bi_2TeO_6 and other unique structures in several oxides (Cheng *et al.*, 2004; García-Munoz *et al.*, 2003; Hervieu *et al.*, 1999; Lalitha, 2010; Seshadri and Hill, 2001). Additionally, only slight deviation of M-O-M bond angles from the value in In_2TeO_6 is observed, which suggests insignificant octahedral distortion in the system.

Table 3.3 Bond lengths and average bond lengths of In-O and Te-O.

M_x	In_2TeO_6	$Ga_{0.2}$	$Ga_{0.4}$	$Bi_{0.1}$	$Bi_{0.3}$	$Bi_{0.5}$	$La_{0.1}$	$La_{0.2}$
In1-O1 (Å)	2.195(27)	2.115(30)	1.900(29)	2.250(30)	2.300(29)	2.355(25)	2.116(23)	2.274(33)
In1-O2 (Å)	2.049(29)	2.031(36)	2.064(29)	2.006(32)	1.980(29)	2.038(28)	2.031(29)	2.231(36)
In1-O3 (Å)	2.118(19)	2.163(31)	2.153(29)	2.184(21)	2.275(20)	2.400(21)	2.302(22)	2.285(28)
In2-O1 (Å)	2.050(18)	2.025(22)	2.080(21)	2.052(18)	1.989(17)	1.961(20)	2.001(18)	1.922(24)
In2-O2 (Å)	2.251(26)	2.239(34)	2.205(32)	2.298(22)	2.309(20)	2.245(21)	2.359(24)	2.279(33)
In2-O3 (Å)	2.163(20)	2.166(26)	2.332(24)	2.108(20)	2.085(22)	2.017(21)	2.028(26)	1.979(33)
Te1-O1 (Å)	2.003(32)	2.036(40)	2.083(30)	1.950(33)	2.017(31)	2.072(29)	2.084(27)	2.067(41)
Te2-O2 (Å)	2.005(37)	2.038(44)	2.079(44)	2.002(36)	2.065(33)	2.087(32)	1.935(34)	1.909(49)
Te2-O3 (Å)	1.991(28)	1.987(39)	1.917(30)	1.977(30)	1.925(29)	1.910(27)	1.953(34)	1.957(35)

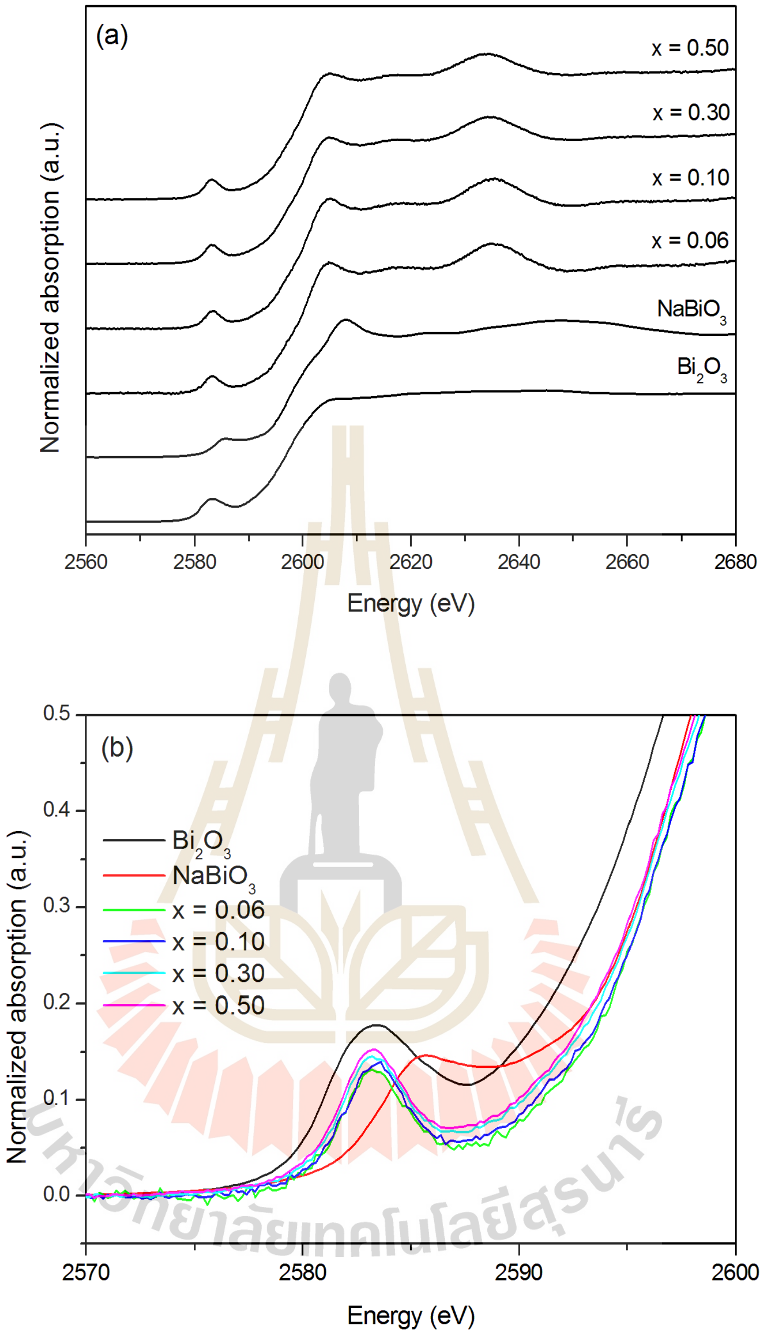

Figure 3.7 (a) Normalised Bi M$_5$-edge XANES spectra and (b) Pre-edge region of Bi M$_5$-edge XANES spectra of $In_{2-x}Bi_xTeO_6$ (x = 0.06, 0.10, 0.30 and 0.50).

X-ray absorption near edge structure (XANES) gives more understanding about the local structure. The edge position and pre-edge features are related to the valence state of absorbing atoms (Berghöfer and Reinen, 1993). In this work, the chemical state of Bi is probed at Bi M_5 edge region. Normalised XANES spectra are shown in Figure 3.7(a). Bi_2O_3 and $NaBiO_3$ were used as references containing Bi^{3+} and Bi^{5+}, respectively. Considering XANES spectra of all compositions, features and position of the pre-edge clearly distinguish the oxidation state of Bi absorbing atom. Pre-edges characteristic of all Bi-doped In_2TeO_6 samples (Figure 3.7(b)) are similar to that of Bi_2O_3, therefore it can be concluded that Bi is in +3 state. The pre-edge at M_5-edge region indicates the electronic transition from 3d core states to unoccupied 6p states (Berghöfer and Reinen, 1993; Ozkendir and Bozgeyik, 2010) because of its relatively low energy even though the transition to empty f states is also possible according to dipole selection rule (Berghöfer and Reinen, 1993). As the energy levels of 6p states are close to that of 6s states, they have strong coupling which results in spin-orbit splittings and the hybridised sp states are generated and bonded with O 2p. This results in the multiple peaks of broad absorption above the edge energy (Ozkendir and Bozgeyik, 2010). In general, the intensity of the white line peaks is related to the symmetry. In this case, lower white line intensity is observed with increasing Bi content indicating a lowering of symmetry in the crystal (Ozkendir and Bozgeyik, 2010). Te valence state in Bi-doped In_2TeO_6 is determined at L_3-edge region. Figure 3.8 illustrates normalised Te L_3-edge XANES spectra of all samples comparing to TeO_2 and $Te(OH)_6$ reference which contain Te^{4+} and Te^{6+}, respectively. Features of both pre-edge and edge energy of all samples indicate the presence of Te^{6+} (Singh *et al.*, 2014). The pre-edge and white line can be denoted to the transition from $2p_{3/2}$ to the empty 5s and from $2p_{3/2}$ to 5d, respectively (Ibanez *et al.*, 1994). The similar XANES spectra confirms the same local structure of Te in all samples.

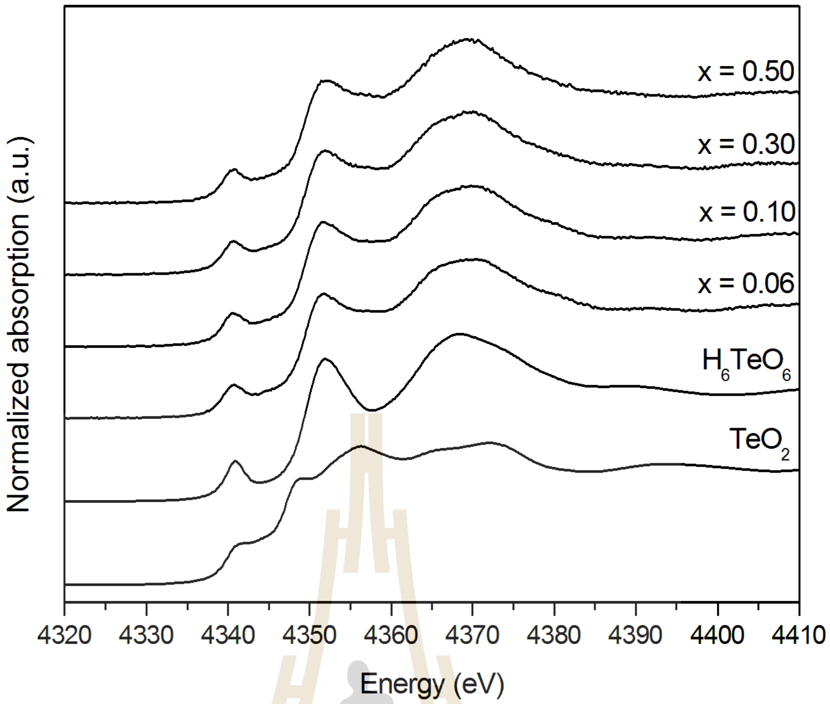

Figure 3.8 Normalised Te L_3-edge XANES spectra of $In_{2-x}Bi_xTeO_6$ (x = 0.06, 0.10, 0.30 and 0.50).

X-ray photoelectron spectroscopy is utilised to confirm the oxidation state of all component cations in the compounds and reflect their contents at the surface. The high-resolution XPS spectra of Bi $4f_{7/2}$, Te $3d_{5/2}$ and O 1s for $In_{2-x}Bi_xTeO_6$ series (x = 0.06, 0.10, 0.30 and 0.50) are shown in Figure 3.9. The symmetric peaks of Bi $4f_{7/2}$ state were observed at 159.1-159.3 eV corresponding to Bi^{3+}-O bonds (Figure 3.9(a)) (Di *et al.*, 2015; Reddy Singh *et al.*, 2012). The Bi $4f_{7/2}$ peak intensity also increases with the Bi content in the samples. The Te $3d_{5/2}$ peaks at 576.2-576.4 eV (Figure 3.9(b)) are attributed to Te^{6+}-O bond (Moulder *et al.*, 1992; Holmberg *et al.*, 2006; Millet *et al.*, 2002). The O 1s peak (Figure 3.9(c)) can be deconvoluted into three main peaks using Gaussian-Lorentzian profile fitting and Shirley background subtraction. The first peak (O_I) at 530.2 eV corresponds to the lattice oxygen (O^{2-}) in the structure. The second peak

(O_{II}) at 531.2 eV could be attributed to C-O bond due to the surface contamination. The third peak (O_{III}) at 533.0 eV can be assigned to surface adsorbed oxygen such as surface hydroxyls and oxygen-contained organic species (He *et al*., 2003; Song *et al*., 2001). The oxidation states of all elemental components from XPS are consistent with XANES results.

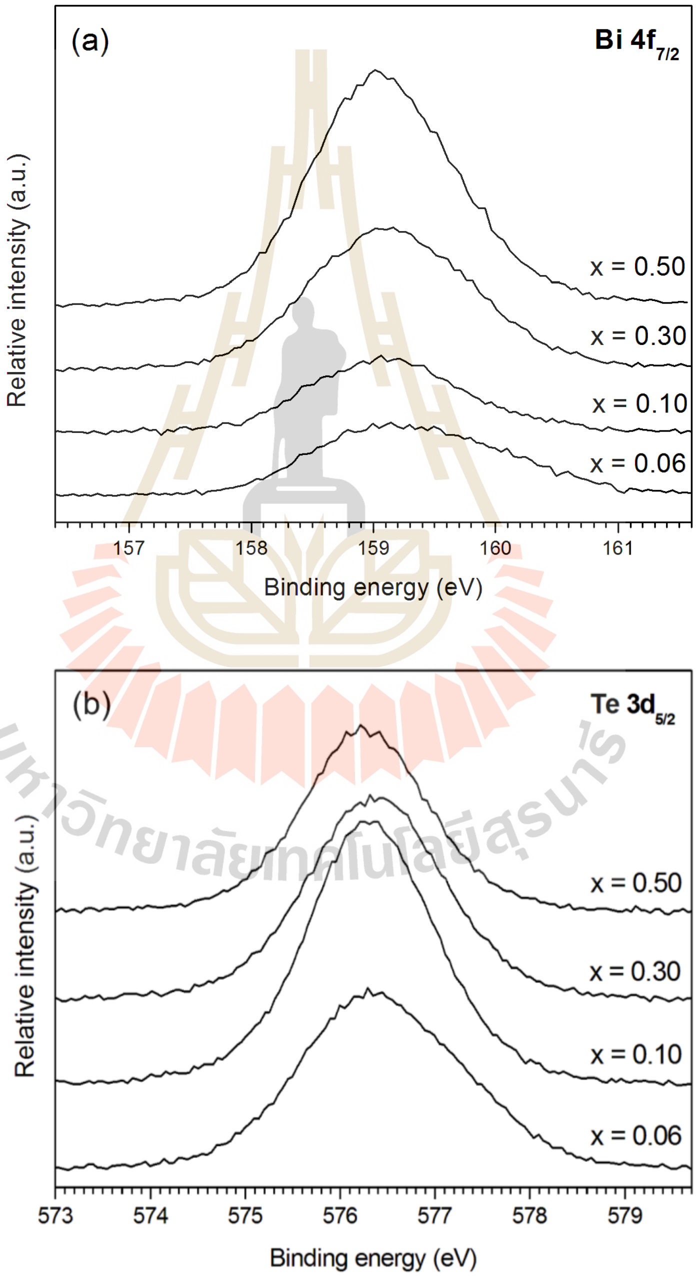

Figure 3.9 XPS spectra of (a) Bi 4$f_{7/2}$, (b) Te 3$d_{5/2}$ and (c) O 1*s* for $In_{2-x}Bi_xTeO_6$ series (x = 0.06, 0.10, 0.30 and 0.50).

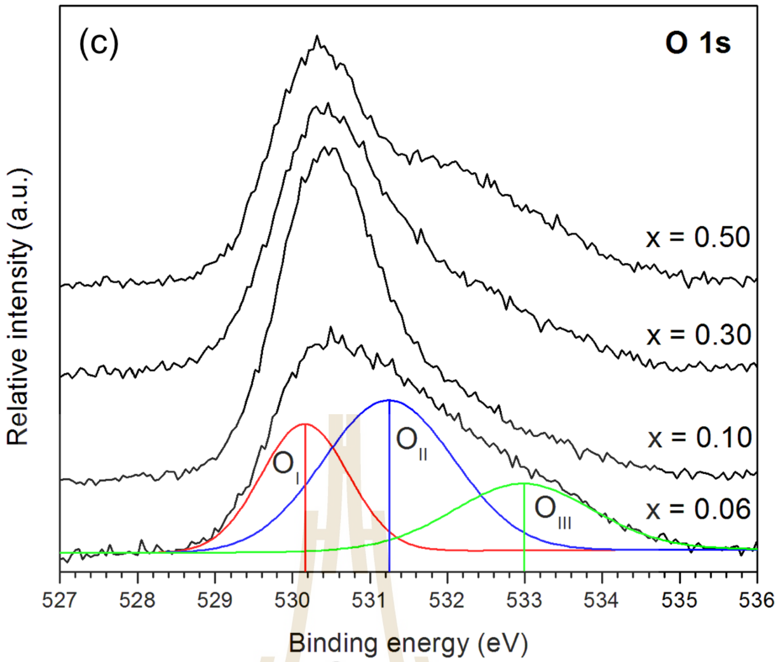

Figure 3.9 XPS spectra of (a) Bi 4$f_{7/2}$, (b) Te 3$d_{5/2}$ and (c) O 1s for $In_{2-x}Bi_xTeO_6$ series (x = 0.06, 0.10, 0.30 and 0.50) (Continued).

3.4.2 Optical properties and band structure calculation

The absorbance UV-Visible spectra are shown in Figure 3.10(a). Based on the sharpness of absorption spectra, the samples may be divided into two groups. The first group includes Bi-doped samples exhibiting sharp absorption edge, while absorption edge of un-doped, Ga-doped and La-doped samples clearly show two different slopes. To obtain band gap energy of the samples, Kubelka-Munk function, $F(R_\alpha)$, was applied. The relation is as follows: $F(R_\alpha) = (1-R_\alpha)^2/2R_\alpha$, where R is reflectance and $R_\alpha = R_{sample}/R_{reference}$. The plots of $[F(R_\alpha)h\upsilon]^{1/n}$ vs. $h\upsilon$ when n = 1/2 corresponding to direct allowed transition are shown in Figure 3.10(b). Extrapolation on the highest slope onto the x axis (when $F(R_\alpha) = 0$) provides E_g.

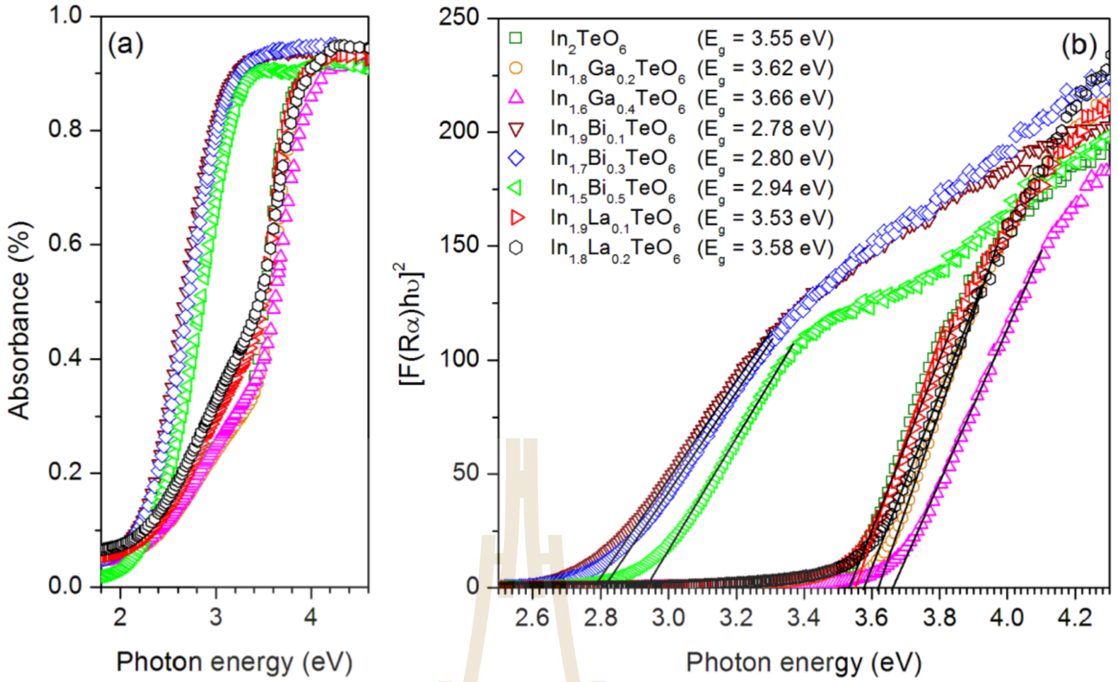

Figure 3.10 Absorbance UV-Visible spectra (a) and Kubelka-Munk plots (b) of $In_{2-x}M_xTeO_6$ when M_x = $Ga_{0.2}$, $Ga_{0.4}$, $Bi_{0.1}$, $Bi_{0.3}$, $Bi_{0.5}$, $La_{0.1}$ and $La_{0.2}$ according to direct allowed transition.

The calculated electronic structures of In_2TeO_6, $In_{1.58}TeO_6Ga_{0.42}$, $In_{1.75}TeO_6La_{0.25}$ and $In_{1.5}TeO_6Bi_{0.5}$ are shown in Figure 3.11. To compensate for the DFT underestimation, a rigid shift is applied to the conduction band to match the calculated optical band gap with the experimental observations (Walsh *et al.*, 2008). The conduction band is shifted by 0.8 eV for In_2TeO_6, 0.9 eV for $In_{1.58}TeO_6Ga_{0.42}$ and $In_{1.5}TeO_6Bi_{0.5}$ and 0.6 eV for $In_{1.75}TeO_6La_{0.25}$. The band structure of In_2TeO_6 in Figure 3.11(a) shows that valence bands are dominated by O 2p and In 4d characters while the conduction bands are mainly dominated by s-character of In 5s and O 2s. For Ga-doping (Figure 3.11(b)), the character of conduction bands is barely changed and crystal symmetry is preserved. On the other hand, valence bands are much disturbed due to Ga d-characters although the intensity of main characters of valence bands still presented. For La, the valence bands are reasonably changed, while conduction bands are fairly changed due to La 6s electrons, as shown in Figure 3.11(c). The parabolic dispersion of CBM at Γ is still observed. In the case of Bi-doping, band structure in Figure 3.11(d) indicates much larger change due to incorporation of Bi into In site. The parabolic dispersion is lifted and s-bands of Bi 6s electrons are introduced into the previous In_2TeO_6 band gap.

Since the optical transition operator between two states is proportional to the momentum operator ($-i\hbar\nabla$), the transition from valence state ψ_v to the conduction state ψ_c is obtained from $\langle\psi_c|\nabla|\psi_v\rangle$ (Gajdoš *et al*., 2006). The quantity of $|\langle\psi_c|\nabla|\psi_v\rangle|^2$ is calculated where ψ_c and ψ_v are restricted to the conduction band minimum (CBM) state and the valence band states at Γ, respectively. In all compounds, the top of valence band exhibits very little dispersion or nearly flat dispersion. The direct optical transitions at Γ from the valence band maximum (VBM) to the CBM are very low (Figure 3.11) which can only make a very weak contribution to photon absorption under the influence of thermal vibrations. This indicates that this transition is forbidden. Similar forbidden transition from VBM and CBM is observed in several In containing oxides (Walsh *et al*., 2008; Koffyberg and Benko, 1980). The strong transitions occur from valence bands, 2 eV below the VBM for undoped, Ga and La-doped In_2TeO_6. The transition from VBM to CBM might be the origin of the less steep absorption at low energy region in UV-Vis spectra for these samples while the strong transitions from 2 eV below VBM is the origin of the steeper absorption edge at higher energy. Similar results are obtained for Bi-doped sample but the strong transition originates from 0.8 eV below VBM. However, VBM is mainly Bi 6s in character which have very weak or zero contribution to photon absorption as shown in the spectrum of transition strength. Therefore, there is only one sharp absorption observed in UV-Vis spectra of Bi-doped samples.

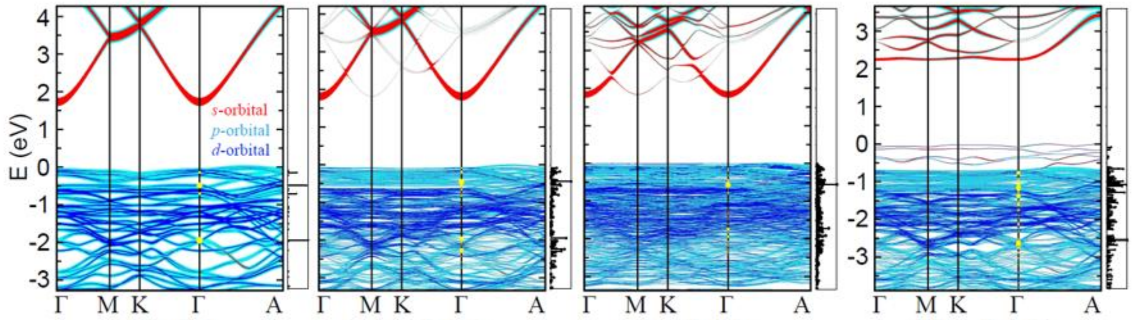

a) In_2TeO_6 b) $In_{1.58}TeO_6Ga_{0.42}$ c) $In_{1.75}TeO_6La_{0.25}$ d) $In_{1.50}TeO_6Bi_{0.50}$

Figure 3.11 The calculated orbital-projected electronic structures of In_2TeO_6, $In_{1.58}TeO_6Ga_{0.42}$, $In_{1.75}TeO_6La_{0.25}$ and $In_{1.5}TeO_6Bi_{0.5}$ along Γ-M-K-Γ-A high symmetry directions. The *s*, *p and d*-band characters are indicated by red (black), blue (grey) and dark blue (dark grey), respectively. The thickness of bands indicates the spectral weight. The spectrum of $\left|\langle\psi_c|\nabla|\psi_v\rangle\right|^2$ for all compounds is shown next to corresponding band structure plot and their magnitudes are given in arbitrary units. The transition strength contributed to prominent peaks is highlighted by yellow (white) dot on the band structure plot.

Photoluminescence (PL) spectra (Figure 3.12) of all samples covers range of wavelengths varying from about 350 to 600 nm resulting in the white light emission. It is noted that the utilised excitation source of 255 nm (4.86 eV) has higher energy than the band gap energy of all samples (E_g = 2.78-3.66 eV). Similar to the UV-Vis spectra, PL spectra can be categorised into two groups. PL spectra of the un-doped In_2TeO_6, Ga-doped and La-doped samples show two strong bands at 3.02 and 2.60 eV. The emission peak in UV region (~410 nm or ~3.02 eV) corresponds to near band edge transition, where the excited electrons go through non-radiative transitions from the bottom of conduction band to the sub-band or surface state first. Radiative transition of excited electrons in the said states to the valence band later occurs which leads to PL. The energy of this emission peaks is therefore slightly lower than the band gap energy (Liqiang *et al*., 2006; Zhang *et al*., 2011). The obtained results do not allow us to completely rule out the defect-originated luminescence. However, it is interesting to note that these samples were prepared under different conditions, which should have effects on type or concentration of the defect (Liqiang *et al*., 2006; Studenikin *et al*., 1998; Li *et al*., 2004; Ahn *et al*., 2009; Shinde and Dhoble, 2012). The fact that the strong luminescence peak at 2.60 eV is not significantly different from samples to samples led us to believed that this transition is either intrinsic or related to some deep defect levels. Possible mechanism includes the presence of the energy level within the band.

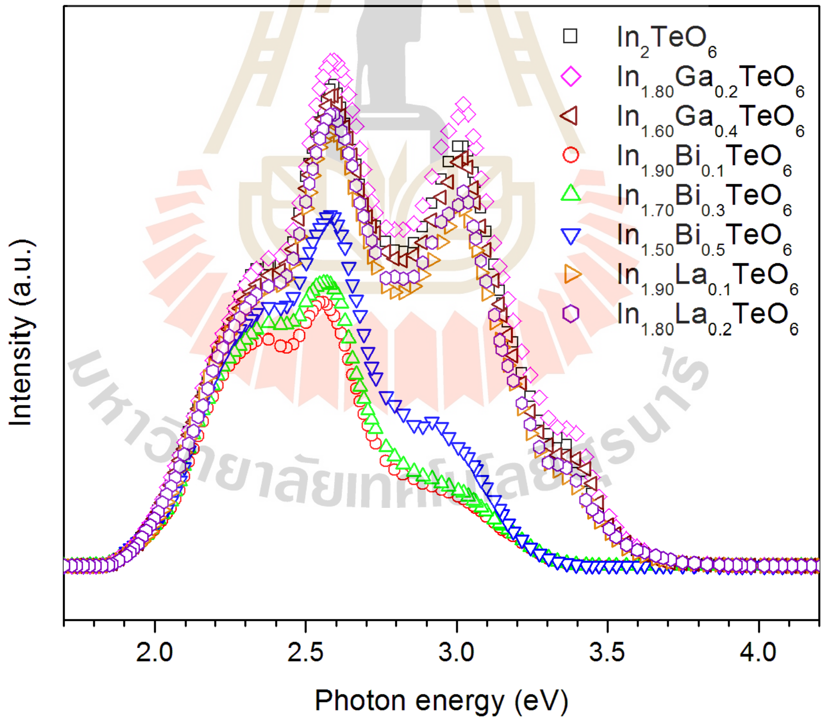

Figure 3.12 Photoluminescence spectra of $In_{2-x}M_xTeO_6$ (M_x = $Ga_{0.2}$, $Ga_{0.4}$, $Bi_{0.1}$, $Bi_{0.3}$, $Bi_{0.5}$, $La_{0.1}$ and $La_{0.2}$).

PL spectra of Bi-doped series show less number of peaks. As these samples have lower band gap energy, the absence of high energy peak is expected. Similar peaks at about 2.60 eV are observed in all Bi-doped samples, but they seem to be slightly broader. We believed that two mechanisms are related to this peak; the near band edge transition and, similar to the first group, the transition from an inter band to valence band. It should be noted that the peaks show a slight blue-shift when Bi content increases, which is consistent with the trend in band gap energy. The very broad shoulder is observed in PL spectra of all samples centering at ~2.95 eV. This could originate from the charge transfer of Te^{6+}-O. Similar observations are reported in many oxides containing d^{10} cations including In^{3+}, Ga^{3+}, Sb^{5+} and Te^{6+} (Blasse, 1990; De Bruin *et al*., 1993).

3.5 Conclusions

Ga, Bi and La-doped In_2TeO_6 have been successfully synthesised with the general formula $In_{2-x}Ga_xTeO_6$ (x = 0, 0.20, 0.40), $In_{2-x}Bi_xTeO_6$ (x = 0, 0.10, 0.30, 0.50) and $In_{2-x}La_xTeO_6$ (x = 0, 0.10, 0.20). The chemical formula of $In_{2-x}M_x$ has been confirmed by EDS. The oxidation state of Bi and Te, confirmed by synchrotron-based techniques, XANES and XPS, are +3 and +6, respectively. The linear relationship between the cell parameters and the composition leads us to conclude that the trivalent cations displace In. XRD peak broadening and SEM image imply the occurrence of internal lattice strain after cation substitution. Doping of Ga, Bi and La cause the size of MO_6 octahedra to change corresponding to the ionic radius of dopants. Additionally, the appearance of stereochemically active lone-pair $6s^2$ electrons causes the shift of Bi^{3+} center within the octahedra. UV-Visible spectroscopy and the electronic structure calculation accompanying with the optical transition operator indicate that undoped-, Ga, Bi and La-doped In_2TeO_6 possess direct allowed transition. In most samples, conduction band dominantly arises from In 5s and O 2s orbitals, while O 2p and In 4d orbitals mainly form valence band. However, the interaction between Bi 6s states and O 2p states additionally influence the valence band and conduction band of Bi doped samples. Photoluminescence property of In_2TeO_6-based samples is reported. All PL peaks are broadened over the visible region thus the samples luminate the visual white light. PL is most probably originated from the near band transition and the presence of the inter-band level.

3.6 References

Ahn, C. H., Kim, Y. Y., Kim, D. C., Mohanta, S. K. and Cho, H. K. (2009). A Comparative Analysis of Deep Level Emission in ZnO Layers Deposited by Various Methods. **Journal Applied Physics.** 105: 013502.

Bates, J. L., Griffin, C. W., Marchant, D. D. and Garnier, J. E. (1986). Electrical Conductivity, Seebeck Coefficient and Structure of In_2O_3-SnO_2. **American Ceramic Society Bulletin.** 65: 673-678.

Bayer, G. (1969). Zur Kristallchemie des Tellurs, Telluroxide und Oxidverbindungen mit Tellur. **Fortschritte der Mineralogie.** 46: 41-72.

Berand, N. and Range, K.-J. (1994). Single-Crystal Structure Refinement of the Trirutile-Type Compound Ga_2TeO_6. **Journal of Alloys and Compounds.** 205: L3-L5.

Bernard, F., Rose, P. and Daniele, M. (1975). Synthese et Etude Structurale du Tellurate (VI) de Thallium (III) Tl_2TeO_6. **Materials Research Bulletin.** 10: 1305-1312.

Berghöfer, G. and Reinen, D. (1993). X-ray Absorption Studies of Mixed-Valent Bi Oxides with Peroxskite Structure. **Modern Physics** Letters B. 7: 1133-1140.

Blasse, G. (1990). Do Metal Ions with d10 Configuration Luminesce? **Chemical Physics Letters.** 175: 237-241.

Blöchl, P. E. (1994). Projector Augmented-Wave Method. **Physical Review B.** 50: 17953-17979.

Cheng, Z. X., Silver, T. M., Li, A. H., Wang, X. L. and Kimura, H. (2004). Effect of Progressive Substitution of La^{3+} by Bi^{3+} on the Structure, Magnetic and Transport Properties of $La_{0.67}Sr_{0.33}MnO_3$. **Journal of Magnetism and Magnetic Materials.** 283: 143-149.

De Bruin, T. J. M., Wiegel, M., Dirksen, G. J. and Blasse, G. (1993). Luminescence of Li_2ZrTeO_6. **Journal of Solid State Chemistry.** 107: 397-400.

Di, J., Xia, J., Ji, M., Li, H., Xu, H., Li, H. and Chen, R. (2015). The Synergistic Role of Carbon Quantum Dots for the Improved Photocatalytic Performance of Bi_2MoO_6. **Nanoscale.** 7: 11433-11443.

Egorysheva, A. V., Ellert, O. G., Zubavichus, Y. V., Gajtko, O. M., Efimov, N. N., Svetogorov, R. D. and Murzin, V. Yu. (2015). New Complex Bismuth Oxides in the Bi_2O_3-NiO-Sb_2O_5 System and Their Properties. **Journal of Solid State Chemistry.** 225: 97-104.

Frit, B. (1975). Structure Crystalline du Tellurate d'Indium In_2TeO_6 **Comptes Rendus Hebdomadaires des Seances de l'Academie des Sciences, Serie C.** 281: 769-772.

Fujimoto, Y. (2009). Local Structure of the Infrared Bismuth Luminescent Center in Bismuth-Doped Silica Glass. **Journal of American Ceramic Society.** 93: 581-589.

Gajdoš, M., Hummer, K., Kresse, G., Furthmüller, J. and Bechstedt, F. (2006). Linear Optical Properties in the Projector-Augmented Wave Methodology. **Physical Review B.** 73: 045112.

García-Munoz, J. L., Frontera, C., Aranda, M. A. G., Ritter, C., Llobet, A., Respaud, M., Goiran, M., Rakoto, H., Masson, O., Vanacken, J. and Broto, J. M. (2003). Charge and Orbital Order in Rare-Earth and Bi Manganites: A Comparison. **Journal of Solid State Chemistry.** 171: 84-89.

Hautier, G., Miglio, A., Waroquiers, D., Rignanese, G.-M. and Gonze, X. (2014). How Does Chemistry Influence Electron Effective Mass in Oxides? A High-Throughput Computational Analysis. **Chemistry of Materials.** 26: 5447-5485.

He, L., Wu, Z., Li, Z., Ju, J., Ou, Q. and Liang, R. (2013). Surface Work Function of Indium Tin Oxide Treated using Plasma Immersion Ion Implantation. **Journal of Physics D: Applied Physics.** 46: 175306.

Hervieu, M., Boullay, Ph., Michel, C., Maignan, A. and Raveau, B. (1999). A New Family of Misfit Layered Oxides with Double Rock Salt Layers $Bi_{\alpha}(A_{0.75\pm\varepsilon}Bi_{0.25\pm\varepsilon}O)_{(3+3x)/2}MO_2$(A = Ca, Sr and M = Co, Cr). **Journal of Solid State Chemistry.** 142: 305-318.

Holmberg, J., Hansen, S., Grasselli, R. K. and Andersson, A. (2006). Catalytic Effects in Propene Ammoxidation Achieved Through Substitutions in the M2 Phase of the Mo-V-Nb-Te-Oxide System. Topics in Catalysis. 38: 17-29.

Höss, P. and Schleid, T. (2007). $Sc_2Te_5O_{13}$ und Sc_2TeO_6: Die ersten Oxotellurate des Scandiums. **Zeitschrift für anorganische und allgemeine Chemie.** 633: 1391-1396.

Ibanez, A., Ericsson, T., Lindqvist, O., Bazin, D. and Philippot, E. (1994). Local Range Order of Tellurium Atoms in TeO_2-BaO and TeO_2-BaF_2, Glassy Systems. **Journal of Materials Chemistry.** 4: 1101-1106.

Kasper, H. M. (1969) Lincoln Laboratory Quarterly Technical Summary, M.I.T.

Koffyberg, F. P. and Benko, F. A. (1980). Cd_2SnO_4, $CdIn_2O_4$, and Cd_2GeO_4 as Anodes for the Photoelectrolysis of Water. **Applied Physics Letters.** 37: 320-322.

Kresse, G. and Furthmüller, J. (1996). Efficiency of Ab-Initio Total Energy Calculations for Metals and Semiconductors using A Plane-Wave Basis Set. **Computational Materials Science.** 6: 15-50.

Kresse, G. and Joubert, D. (1999). From Ultrasoft Pseudopotentials to the Projector Augmented-Wave Method. **Physical Review B.** 59: 1758-1775.

Lalitha, G. and Reddy, P. V. (2010). Low Temperature Resistivity Anomalies in Bismuth Doped Manganites. **Journal of Alloys and Compounds.** 494: 476-482.

Li, D., Leung, Y. H., Djurišić, A. B., Liu, Z. T., Xie, M. H., Shi, S. L., Xu, S. J. and Chan, W. K. (2004). Different Origins of Visible Luminescence in ZnO Nanostructures Fabricated by The Chemical and Evaporation Methods. **Applied Physics Letters.** 85: 1601-1603.

Li, J., Siritanon, T., Stalick, J. K., Sleight, A. W. and Subramanian, M. A. (2011). Structural Studies and Electrical Properties of Cs/Al/Te/O Phases with the Pyrochlore Structure. **Inorganic Chemistry.** 50: 5747-5754.

Liqiang, J., Yichun, Q., Baiqi, W., Shudan, L., Baojiang, J., Libin, Y., Wei, F., Honggang, F. and Jiazhong, S. (2006). Review of Photoluminescence Performance of Nano-Sized Semiconductor Materials and Its Relationships with Photocatalytic Activity. **Solar Energy Materials & Sollar Cells.** 90: 1773-1787.

Llanosa, J., Castillo, R., Barrionuevo, D., Espinoza, D. and Conejeros, S. (2009) The Family of Ln_2TeO_6 Compounds (Ln = Y, La, Sm and Gd): Characterization and Synthesis by the Pechini Sol-Gel Process. **Journal of Alloys and Compounds.** 485: 565-568.

Malone, J. A., Dorrian, J. F., Muller, O. and Newnham, R. E. (1969). Crystal Structure of Lu_2TeO_6. **Journal of the American Ceramic Society.** 52: 570-572.

Millet, J. M. M., Roussel, H., Pigamo, A., Dubois, J. L. and Jumas, J. C. (2002). Characterization of Tellurium in MoVTeNbO Catalysts for Propane Oxidation or Ammoxidation. **Applied Catalysis A: General.** 232: 77-92.

Moulder, J. F., Stickle, W. F., Sobol, P. E. and Bomben, K. D. (1992). Handbook of X-ray Photoelectron Spectroscopy, second ed., Perkin-Elmer Corp., Eden Prairie, Minnesota.

Murty, B. S., Shankar, P., Raj, B., Rath, B. B. and Murday, J. (2013). Textbook of Nanoscience and Nanotechnology, first ed., Springer-Verlag Berlin and Heidelberg GmbH & Co. KG, Berlin, Germany.

Natansohn, S. (1968). The Synthesis and Structure of Rare-Earth and Indium Tellurates, R_2TeO_6. **Journal of Inorganic and Nuclear Chemistry.** 30: 741-745.

Ozkendir, O. M. and Bozgeyik, M. S. (2010). Electronic Structure Difference of Stoichiometric and Off-Stoichiometric SBT. **The European Physical Journal B.** 76: 203-208.

Ozawaa, K., Eguchib, M., Nakamuraa, H. and Sakka, Y. (2004). Bismuth-Doping Effect on Structural Properties and Proton Conductivity of Pyrochlore-Type Antimonic Acid. **Solid State Ionics.** 172: 109-112.

Pankajavalli, R., Jain, A., Sharma, A., Anthonysamy, S. and Ganesan, V. (2013). Thermodynamic Investigation on M–Te–O (M = Sc, Y) System. **Journal of Thermal Analysis and Calorimetry.** 112: 83-93.

Perdew, J. P., Burke, K. and Ernzerhof, M. (1996). Generalized Gradient Approximation Made Simple. **Physical Review Letters.** 77: 3865-3868.

Park, J.-H. and Woodward, P. M. (2000). Synthesis, Structure and Optical Properties of Two New Perovskites: $Ba_2Bi_{2/3}TeO_6$ and $Ba_3Bi_2TeO_9$. **International Journal Inorganic Materials.** 2: 153-166.

Reddy, K. H., Martha, S. and Parida, K. M. (2012). Facile Fabrication of Bi_2O_3/Bi-$NaTaO_3$ Photocatalysts for Hydrogen Generation under Visible Light iIradiation. RSC **Advances.** 2: 9423-9436.

Redman, M. J., Binnie, W. P. and Mallio, W. J. (1971). Formation and Crystallography of Indium Tellurite, $In_2Te_3O_9$, and Indiurn Tellurate, ln_2TeO_6. **Journal of the Less-Common Metals.** 23: 313-315.

Retuerto, M., Muñoz, A., Martínez-Lope, M. J., Garcia-Hernandez, M., André, G., Krezhov, K. and Alonso, J. A. (2013). Influence of the Bi^{3+} Electron Lone Pair in the Evolution of the Crystal and Magnetic Structure of $La_{(1-x)}Bi_{(x)}Mn_2O_5$ Oxides. **Journal of Physics: Condensed. Matter.** 25: 216002.

Seshadri, R. and Hill, N. A. (2001). Visualizing the Role of Bi 6s “Lone Pairs” in the Off-Center Distortion in Ferromagnetic $BiMnO_3$. **Chemistry of Materials.** 13: 2829-2899.

Shannon, R. D. and Prewitt, C. T. (1969). Effective Ionic Radii in Oxides and Fluorides**.** **Acta Crystallographica Section B.** 25: 925-946.

Shannon, R. D. (1976). Revised Effective Ionic Radii and Systematic Studies of Interatomic Distances in Halides and Chalcogenides. **Acta Crystallographica Section A.** 32: 751-767.

Shannon, R. D., Gillson, J. L. and Bouchard, R. J. (1977). Single Crystal Synthesis and Electrical Properties of $CdSnO_3$, Cd_2SnO_4, In_2TeO_6 and $Cdln_2O_4$. **Journal of Physics and Chemistry of Solids.** 38: 877-881.

Shemirani, B. and Koffyberg, F. P. (1992). Semiconductivity and Band Gap of Tin-Doped Indium Tellurate. **Materials Research Bulletin.** 27: 693-698.

Shinde, K. N. and Dhoble, S. J. (2012). Effect of Synthesis Method on Photoluminescence Properties of $Na_2Sr_2Al_2PO_4Cl_9:Ce^{3+}$ Nanophosphor. **Nano-Micro Letters.** 4: 78-82.

Singh, A., Moriyoshi, C., Kuroiwa, Y. and Pandey, D. (2012). Evidence for Diffuse Ferroelectric Phase Transition and Cooperative Tricritical Freezing of Random-Site Dipoles due to Off-Centered Bi^{3+} Ions in the Average Cubic Lattice of $(Ba_{1-x}Bi_x)(Ti_{1-x}Fe_x)O_3$. **Physical Review B.** 85: 064116.

Singh, H., Sinha, A. K., Ghosh, H., Singh, M. N., Rajput, P., Prajapat, C. L., Singh, M. R. and Ravikumar, G. (2014). Structural Investigations on $Co_{3-x}Mn_xTeO_6$; (0 x 2); High Temperature Ferromagnetism and Enhanced Low Temperature Anti-Ferromagnetism. **Journal of Applied Physics.** 116: 074904.

Siritanon, T., Sleight, A. W. and Subramanian, M. A. (2011). Compositionally Controlled Metal-Insulator Transition in $Tl_{2-x}In_xTeO_6$. **Journal of Solid State Chemistry.** 84: 877-880.

Song, W., So, S. K. and Cao, L. (2001). Angular-Dependent Photoemission Studies of Indium Tin Oxide Surfaces. **Applied Physics A.** 72: 361-365.

Studenikin, S. A., Golego, N. and Cocivera, M. (1998). Fabrication of Green and Orange Photoluminescent, Undoped ZnO Films using Spray Pyrolysis. **Journal of Applied Physics.** 84: 2287-2294.

Tomić, M., Jeschke, H. O. and Valentí, R. (2014). Unfolding of Electronic Structure Through Induced Representations of Space Groups: Application to Fe-Based Superconductors. **Physical Review B.** 90: 195121.

Tröemel, M., Huetzler, F. W., Burckhardt, H. G., Platte, C. and Muench, E. (1987). Lanthanoidtellurate Ln_2TeO_6. **Zeitschrift für anorganische und allgemeine Chemie.** 551: 95-100.

Udovic, M., Valant, M. and Suvorov, D. (2004). Formation and Decomposition of the Bi_2TeO_6 Compound. **Journal of the European Ceramic Society.** 24: 953-958.

US Pat., 6 124 057, 2000.

Walsh, A., Da Silva, J. L. F., Wei, S.-H., Körber, C., Klein, A., Piper, L. F. J., DeMasi, A., Smith, K. E., Panaccione, G., Torelli, P., Payne, D. J., Bourlange, A. and Egdell, R. G. (2008). Nature of the Band Gap of In_2O_3 Revealed by First-Principles Calculations and X-Ray Spectroscopy. **Physical Review Letters.** 100: 167402.

Zhang, J., Chen, X., Shen, Y., Li, Y., Hu, Z. and Chu, J. (2011). Synthesis, Surface Morphology, and Photoluminescence Properties of Anatase Iron-Doped Titanium Dioxide Nano-Crystalline Films. **Physical Chemistry Chemical Physics.** 13: 13096-13105.

CHAPTER IV

UNDERSTANDING STRUCTURE, OPTICAL AND ELECTRICAL PROPERTIES OF M-DOPED $In_4Sn_3O_{12}$ (M = Nb, Ta)

4.1 Abstract

The current research aims to investigate transparent conducting properties of $In_4Sn_3O_{12}$ related compounds. Undoped and M-doped $In_4Sn_3O_{12}$ with the formula $In_{4+x}Sn_{3-2x}M_xO_{12}$ (M_x = $Nb_{0.5}$, $Ta_{0.5}$) have been successfully synthesised by solid state reaction as confirmed by powder X-ray diffraction. Interestingly, only the composition with x = 0.5 could be achieved without impurity. With the substitution of Nb/Ta, the In/Sn mol ratio increases and thus resulted in the enlargement in cell parameters *a*, *c* and cell volume. The oxidation states of all elements were identified by X-ray photoelectron spectroscopy to be In^{3+} ,$Sn^{4+}$and $Nb^{5\ +}$/Ta^{5+}. The larger optical band gap energies were obtained in doped samples, coresponding to their pale green colour compared to the light green of undoped sample. While the results from computational calculations indicate that Nb and Ta substitutions do not significantly change the band structure, they have large effects on the sample electronic properties. Although the conductivity of $In_4Sn_3O_{12}$ is relatively high, those of the $In_{4.5}Sn_2Nb_{0.5}O_{12}$ and $In_{4.5}Sn_2Ta_{0.5}O_{12}$ are much lower. To investigate the conduction mechanism, the conductivity of the sample after heat treatment in N_2 was studied. The improved conductivity after such annealing along with the results from X-ray photoelectron spectroscopy suggest that the major charge carriers are electrons created from oxygen vacancies in the lattice.

4.2 Introduction

$In_4Sn_3O_{12}$ becomes an attractive candidate for transparent conducting oxides (TCOs) since it was discovered with the high electrical conductivity ($\rho_{RT} \sim 2 \times 10^{-2}$ ohm.cm) (Bates *et al*., 1986). This less-indium containing oxides interest researchers as an alternative TCOs to the famous ITO (Sn-doped In_2O_3), which has the large conductivity (($\rho_{RT} \sim 1 \times 10^{-4}$ ohm.cm) (Ginley and Perkins, 2011). The electrical properties were improved by the preparation conditions e.g. annealing in Ar (Behr and Krabbes, 1996), optimum O_2 partial pressure (Minami *et al*., 1997) and by Sb substitution (Choisnet *et al*., 2004). The extensive structural details of $In_4Sn_3O_{12}$ (Choisnet *et al*., 2004; Nadaud *et al*., 1998; Pitschke *et al*., 2000; Choisnet *et al*., 2007; O'Neil *et al*., 2010; Zhang and Wang, 2011) and the relationship between In/Sn cations environments and electrical properties were investigated (Nadaud *et al*., 1998). Moreover, the DFT band structure calculation of $In_4Sn_3O_{12}$ (O'Neil *et al*., 2010; Zhang and Wang, 2011; Ren *et al*., 2006) and Sb-doped $In_4Sn_3O_{12}$ (Ren *et al*., 2006) has been performed to try to understand their electrical properties. To the best of our knowledge, the origin of high electrical conductivity in $In_4Sn_3O_{12}$ has not been clarified. An interesting point is that the calculated electronic band structure of $In_4Sn_3O_{12}$ (Zhang and Wang, 2011) is similar to that of famous TCOs, Sn-doped In_2O_3 (Mryasov and Freeman, 2001).

Here, M-doped $In_4Sn_3O_{12}$, when M = Nb and Ta, have been investigated with the formulas of $In_{4+x}Sn_{3-2x}M_xO_{12}$ (M_x = $Nb_{0.5}$ and $Ta_{0.5}$). The obtained samples are characterised using X-ray diffraction (XRD) to study the phase purity. Rietveld refinement method is used to get the crystallographic information including cell parameters, cell volume, cation occupancy, and bond length. X-ray photoelectron spectroscopy (XPS) is utilised to confirm the oxidation state of all cations in the compounds. The optical properties, which are probed by both UV-Vis diffuse reflectance spectroscopy and Photoluminescence (PL) spectroscopy, provide the band gap energy (E_g) and absorption and re-emitting phenomena. The computational study is used to gain understandings about the optical properties from the calculated band structure and electrical properties, which is used to explain the origin of conductivity in $In_4Sn_3O_{12}$.

4.3 Experimental

All polycrystalline samples were synthesised using solid state reaction. In_2O_3 (Sigma-Aldrich, 99.99%), SnO_2 (Acros Organics, 99.9%), Nb_2O_5 (Acros Organics, 99.99%), Ta_2O_5 (Acros Organics, 99.99%), Sc_2O_3 (Sigma-Aldrich, 99.9%), and ZrO_2 (Carlo Erba, 99%) were used as precursors. The reaction was performed at 1400-1450 °C in air for 24-36 hours with several intermediate grindings. Post annealing of N_2 was performed at 900 °C for 3 hours to investigate the electrical properties.

The phase identification was studied by powder X-ray diffraction (XRD) using a Bruker D2 Phaser diffractometer with Cu Kα radiation (λ = 1.5406 Å). The crystallographic information was obtained by Rietveld refinement using TOPAS software (V4.2.0.2) from high quality XRD patterns, which were collected in the 2-theta range of 10-120° with an increment of 0.02° by a scan rate of 2s/step. Different peak shape types were applied; PV_TCHZ function matches $In_4Sn_3O_{12}$ while PV_MOD peak types matches the rest of samples. X-ray photoelectron spectroscopy (XPS) was performed at the SUT-NANOTEC-SLRI XPS Beamline (BL5.1), the SUT-NANOTEC-SLRI joint research facility, Synchrotron Light Research Institute (SLRI), Thailand (electron energy of 1.2 GeV, beam current of 80-120 mA). Optical diffuse reflectance spectroscopy (DRS) was performed using an Agilent UV-Vis-NIR spectrophotometer (model Cary 5000). The diffuse reflectance (%R) spectra were collected in the scan wavelength range of 200-800 nm with the double beam mode. Photoluminescence measurement was carried out utilising an AVANTES AvaSpec-2048TEC-USB2-2 spectrometer with the excitation LED light source of 255 nm.

4.4 Calculation details

All calculations reported herein were carried out on the basis of spin-polarised density functional theory (DFT) with periodic model as implemented in the Vienna ab initio simulation package (VASP 5.3) (Kresse and Furthmüller, 1996a; Kresse and Furthmüller, 1996b; Kresse and Hafner, 1993). The exchange and correlation functional was approximated using the Perdew–Burke–Ernzerhof functional based on the generalised gradient approximation (Xiao *et al.*, 2013). We chose the ultra-soft pseudopotential with projector augmented-wave (PAW) method (Blöchl, 1994; Joubert, 1999) to describe the nuclei and core electronic states. The valence electrons considered are In 4d5s5p, Sn 4d5s5p O 2s2p, Nb 4s4p4d5s, and Ta 5p5d6s. Their wave functions were expanded in plane-wave with a cutoff energy of 500 eV. A Gaussian smearing (σ = 0.05 eV) was used during structural relaxations in which the calculated energies were extrapolated to zero smearing width. The ion positions were optimised using the Monkhorst-Pack (MP) approach (Monkhorst and Pack, 1976) with a k-point sampling of 2×2×2. The optimisation was ceased when the calculated residual forces were lower than 0.02 eV/Å.

To explore the stability of oxygen vacancies in the stoichiometric and doped $In_4Sn_3O_{12}$ structures, we used the hexagonal unit cell of $In_4Sn_3O_{12}$ as a model. The $In_4Sn_3O_{12}$ unit cell contains 12 In cations, 9 Sn cations, and 36 O anions which corresponds to three $In_4Sn_3O_{12}$ formula units ($In_{12}Sn_9O_{36}$). Sn and In cations are statistically distributed at the 18*f* sites which yield nonequivalent lattice configurations with different total energies. For simplicity, we considered only the configuration depicted in Figure 4.1a to represent the $In_4Sn_3O_{12}$ structure. While the other lower energy configurations may exist, it is expected that the overall stability of oxygen vacancies remains unchanged since these oxygen vacancies are connected with various Sn and In cations throughout the lattice. In addition, the considered structural configuration was successfully used to describe the electronic structure of $In_4Sn_3O_{12}$. The doped structures were created based on the experiments carried out in this study where one Sn ion in the unit cell was replaced by a doping metal ion (Nb or Ta). Substitution of Sn(IV) by a higher valent cation, Nb(V) or Ta(V), yields an extra electron in the lattice. To compensate the extra charge, an adjacent Sn ion to the doped metal ion was replaced by an In ion as shown in Figure 4.1b. As a result, the doped structures maintain their charge neutrality where no additional charge carriers were created which is consistent with that obtained from our synthesised samples.

To explore the electronic structures of the stoichiometric and doped $In_4S_3O_{12}$ systems, we computed their band structures and projected density of states (PDOS) employing the tetrahedral smearing method with Bloch corrections. A denser k-point of 5×5×5 was necessary to achieve converged electronic structures.

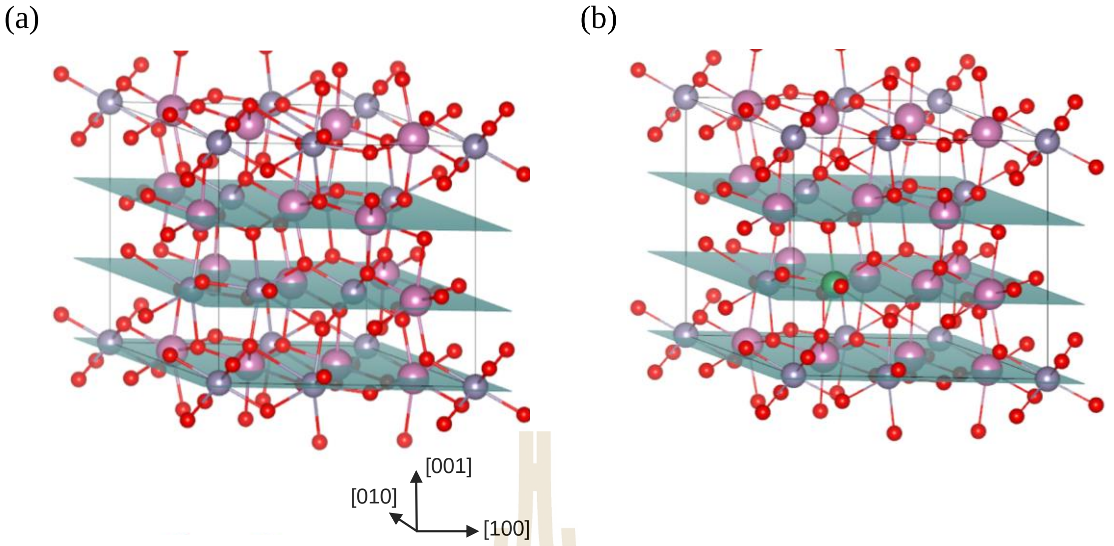

Figure 4.1 Unit cell of a) pure $In_4Sn_3O_{12}$ and b) metal (Nb, Ta) doped $In_4Sn_3O_{12}$. Pink, grey and red spheres represent In, Sn and O ions, respectively. The green sphere denotes the position of the doping ions (Nb or Ta).

4.5 Results and discussion

4.5.1 Crystal structure

$In_4Sn_3O_{12}$ adopts a rhombohedral lattice (hexagonal basis) in a trigonal space group ($R\bar{3}H$) (Nadaud *et al*., 1998). The ideal structure (Figure 4.2) consists of two distinguishable sites in octahedra (3*a*) and seven-fold coordination environment (18*f*), which are labeled as M1 and M2, respectively. All M1 site are occupied by Sn while the rest of Sn and In occupy M2 (Nadaud *et al*., 1998; Choisnet *et al*., 2007). The structure derives from M_7O_{12}-type oxygen-deficient fluorite structure (Pitschke *et al*., 2000). The oxygen atoms and anionic vacancies are periodically ordered in this structure (Choisnet *et al*., 2007).

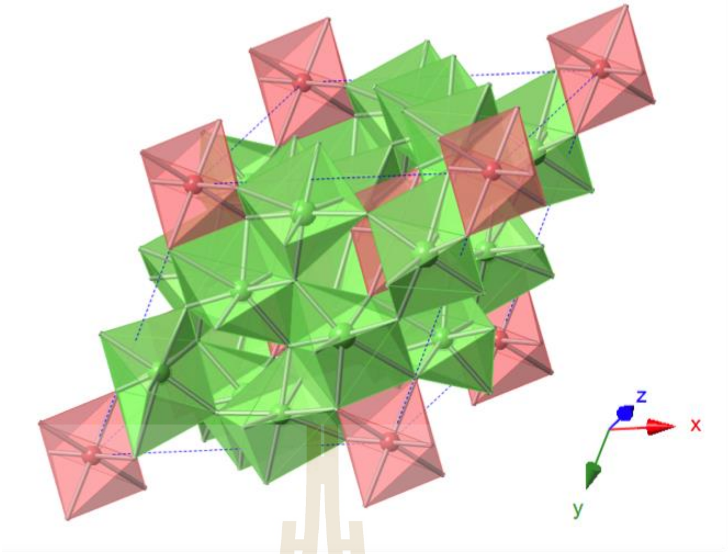

Figure 4.2 Crystal structure of ideal $In_4Sn_3O_{12}$.

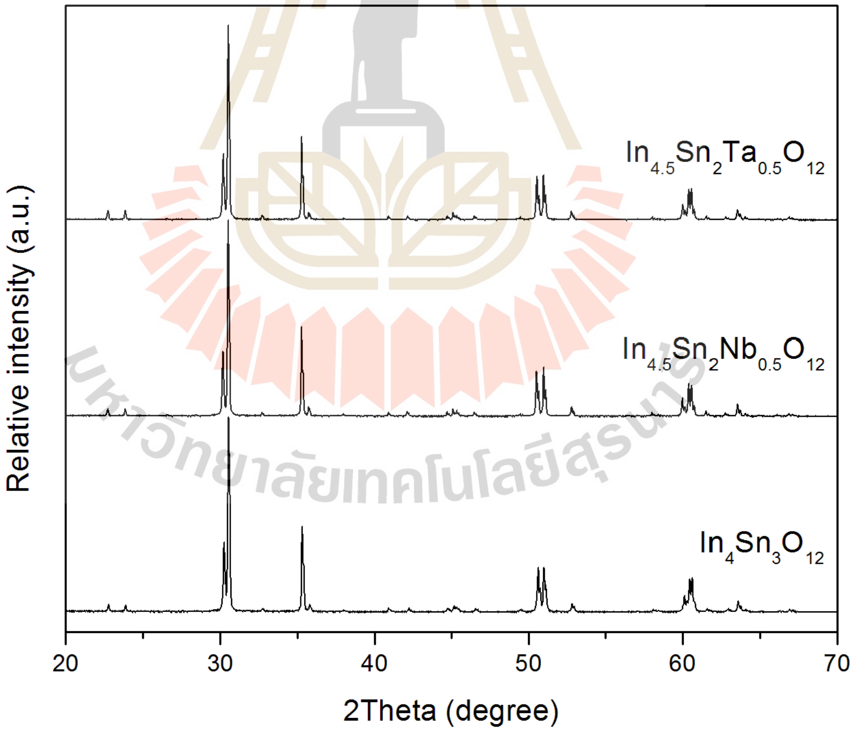

Figure 4.3 XRD patterns of $In_4Sn_3O_{12}$ and $In_{4+x}Sn_{3-2x}M_xO_{12}$ (M = $Nb_{0.5}$, $Ta_{0.5}$).

In this work, undoped and M-doped $In_4Sn_3O_{12}$ with the formula $In_{4+x}Sn_{3-2x}M_xO_{12}$ (M_x = $Nb_{0.5}$ and $Ta_{0.5}$) have been successfully synthesised. Their XRD patterns (Figure 4.3) can be indexed based on $In_4Sn_3O_{12}$ (PDF 08-0773), no impurity phase was detected. It is found that Nb and Ta doped samples form single phase with only one composition (x = 0.5). In_2O_3 and/or SnO_2 are detected as impurities for the compositions with lower doping content and $InMO_4$ (M = Nb and Ta) phase appears for the compositions with higher M loading.

The structural analysis was further performed by Rietveld refinement and the plots are shown in Figure 4.4. The full pattern analysis fitting was well obtained as the convergence was reached easily, resulting in the good confident values indicating the good agreement between the observed and the calculated patterns. The refined parameters and crystallographic information are reported in Table 4.1 and 4.2. In the refinement, the modified Thompson-Cox-Hastings pseudo-Voigt “TCHZ” peak type is applied for undoped $In_4Sn_3O_{12}$ sample, while the diffraction peak profile of M-doped samples is fitted with the “PV_MOD” peak type. Regarding the compounds with the formula $In_{4.5}Sn_2M_{0.5}O_{12}$ (M = Nb, Ta), Nb and Ta were refined over both the Sn1 (3*a*) and Sn2/In (18*f*) sites. Nb distributes over both sites while Ta mostly occupies at Sn1(3*a*) site.

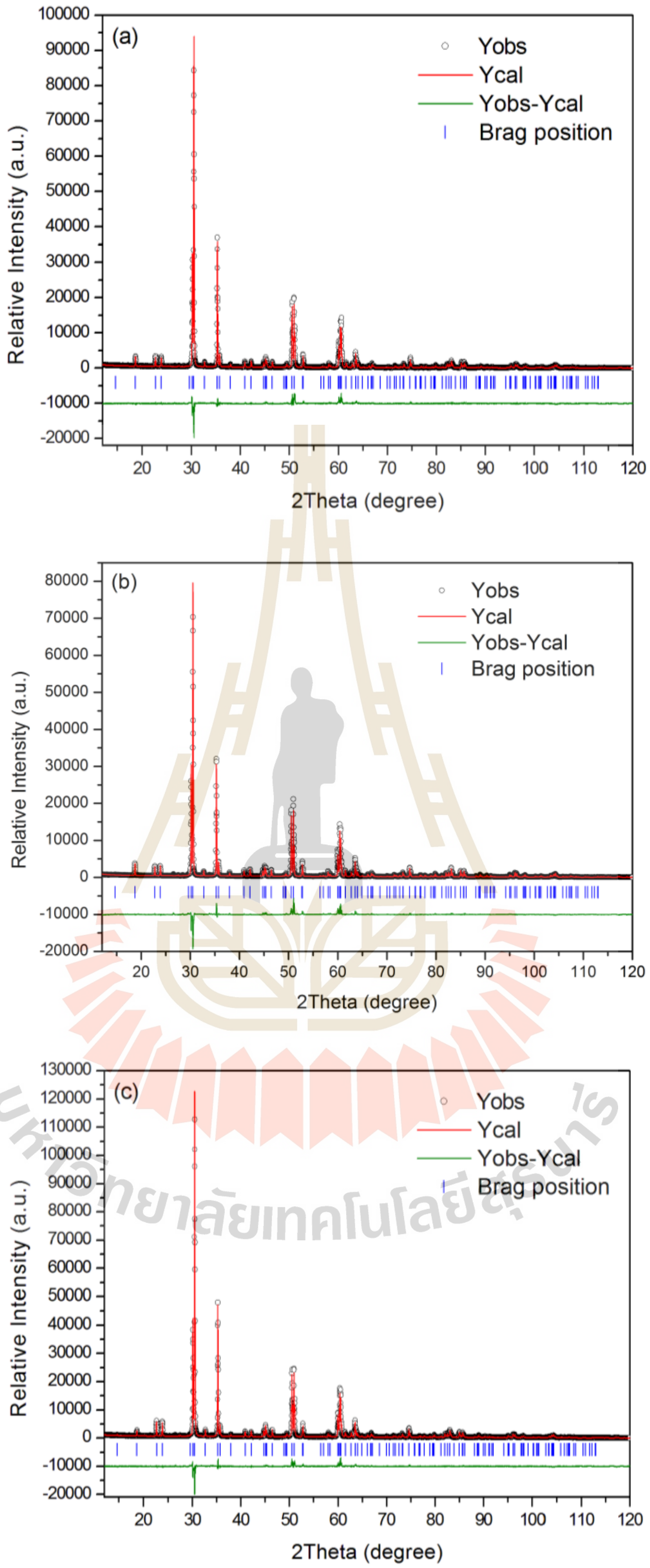

Figure 4.4 Rietveld refinement plots of (a) $In_4Sn_3O_{12}$, (b) $In_{4.5}Sn_2Nb_{0.5}O_{12}$ and (c) $In_{4.5}Sn_2Ta_{0.5}O_{12}$.

Table 4.1 Rietveld refinement parameters of $In_4Sn_3O_{12}$ and $In_{4+x}Sn_{3-2x}M_xO_{12}$ ($M_x = Nb_{0.5}$, $Ta_{0.5}$).

	a (Å)	*c* (Å)	V (Å^3)	%R$_{exp}$	%R$_p$	%R$_{wp}$	GOF
$In_4Sn_3O_{12}$	9.4634(89)	8.8567(10)	686.90(15)	3.75	9.68	12.83	3.42
$In_{4.5}Sn_2Nb_{0.5}O_{12}$	9.4666(71)	8.8751(88)	688.80(12)	3.87	10.85	13.67	3.53
$In_{4.5}Sn_2Ta_{0.5}O_{12}$	9.4671(70)	8.8736(84)	688.75(12)	3.17	7.73	10.22	3.22

The cell parameters *a*, *c* and cell volume (Table 4.1) of Nb and Ta-substituted samples are slightly larger than that of undoped sample. Note that the oxidation states of Nb and Ta are 5+ as confirmed by XPS. The ionic radii of Nb^{5+}/Ta^{5+} (r_i = 0.64 Å, C.N. = 6) are less than that of Sn^{4+} (r_i = 0.69 Å, C.N. = 6) and In^{3+} (r_i = 0.80 Å, C.N. = 6) (Shannon, 1976). According to the formula $In_{4+x}Sn_{3-2x}M_xO_{12}$ ($M_x = Nb_{0.5}$, $Ta_{0.5}$), as the M (Nb/Ta) cations increases, the Sn content decreases while the In content increases with the mol ratio of 2:1 to balance the charge neutrality of compounds ($2Sn^{4+} \leftrightarrow M^{5+} + In^{3+}$). Therefore, it can be concluded that the cell parameters slightly increase because of the addition of a larger In^{3+}.

In spite of the same ionic radii, Nb and Ta have dissimilar atomic number and X-ray scattering power. This should affect their peak intensity in the XRD patterns; nonetheless, the difference in peak intensity was not observed as only small amount of Nb and Ta are in the lattice. It should be noted that no peak broadening is observed in all M-doped compounds because the difference in ionic radii of M cations and the parents cations are less than 20% thus causing only little strain in the lattice.

Table 4.2 Crystallographic data of $In_4Sn_3O_{12}$ and $In_{4+x}Sn_{3-2x}M_xO_{12}$ (M_x = $Nb_{0.5}$, $Ta_{0.5}$).

Atom	Site	*x*	*y*	*z*	Occupancy	$B_{eq.}$ (Å^2)
$In_4Sn_3O_{12}$						
Sn1	3*a*	0	0	0	1	2.249(73)
Sn2	18*f*	0.2525(15)	0.2145(13)	0.3504(14)	1/3	2.056(26)
In	18*f*	0.2525(15)	0.2145(13)	0.3504(14)	2/3	2.056(26)
O1	18*f*	0.1978(11)	0.1748(16)	0.1141(88)	1	1.930(29)
O2	18*f*	0.1895(16)	0.9756(15)	0.3862(87)	1	2.040(26)
$In_{4.5}Sn_2Nb_{0.5}O_{12}$						
Sn1/Nb	3*a*	0	0	0	0.821(35)/0.179(35)	2.130(10)
Sn2/Nb	18*f*	0.2531(16)	0.2155(14)	0.3516(15)	0.1966(58)/0.0534(58)	1.653(32)
In	18*f*	0.2531(16)	0.2155(14)	0.3516(15)	0.75	1.653(32)
O1	18*f*	0.1913(12)	0.1759(18)	0.1113(92)	1	1.190(27)
O2	18*f*	0.1954(16)	0.9772(15)	0.3765(96)	1	1.450(26)
$In_{4.5}Sn_2Ta_{0.5}O_{12}$						
Sn1/Ta	3*a*	0	0	0	0.510(17)/0.490(17)	2.846(81)
Sn2/Ta	18*f*	0.2520(14)	0.2150(12)	0.3510(12)	0.3317(28)/0.0016(28)	2.199(30)
In	18*f*	0.2520(14)	0.2150(12)	0.3510(12)	2/3	2.199(30)
O1	18*f*	0.1986(11)	0.1727(15)	0.1150(80)	1	2.360(25)
O2	18*f*	0.1888(13)	0.9754(13)	0.3862(78)	1	2.700(25)

$B_{eq.}$ = equivalent isotropic thermal parameters

X-ray photoelectron spectroscopy is performed to confirm the oxidation states of the elements. The high-resolution XPS spectra of In $3d_{5/2}$, Sn $3d_{5/2}$, O 1s, Nb $3d_{5/2}$ and Ta $4f_{7/2}$ are shown in Figure 4.5. For undoped, $Nb_{0.5}$-doped and $Ta_{0.5}$-doped $In_4Sn_3O_{12}$ samples, In $3d_{5/2}$ (Figure 4.5(a)) observed at ~444.49 eV corresponds to In^{3+} (Bertrand, 1981; Lin *et al*., 1977; Song *et al*., 2001) and Sn $3d_{5/2}$ (Figure 4.5(b)) observed at ~486.47 eV is assigned to Sn^{4+} (Ansell *et al*., 1977; Fan and Goodenough, 1977). O 1s spectra

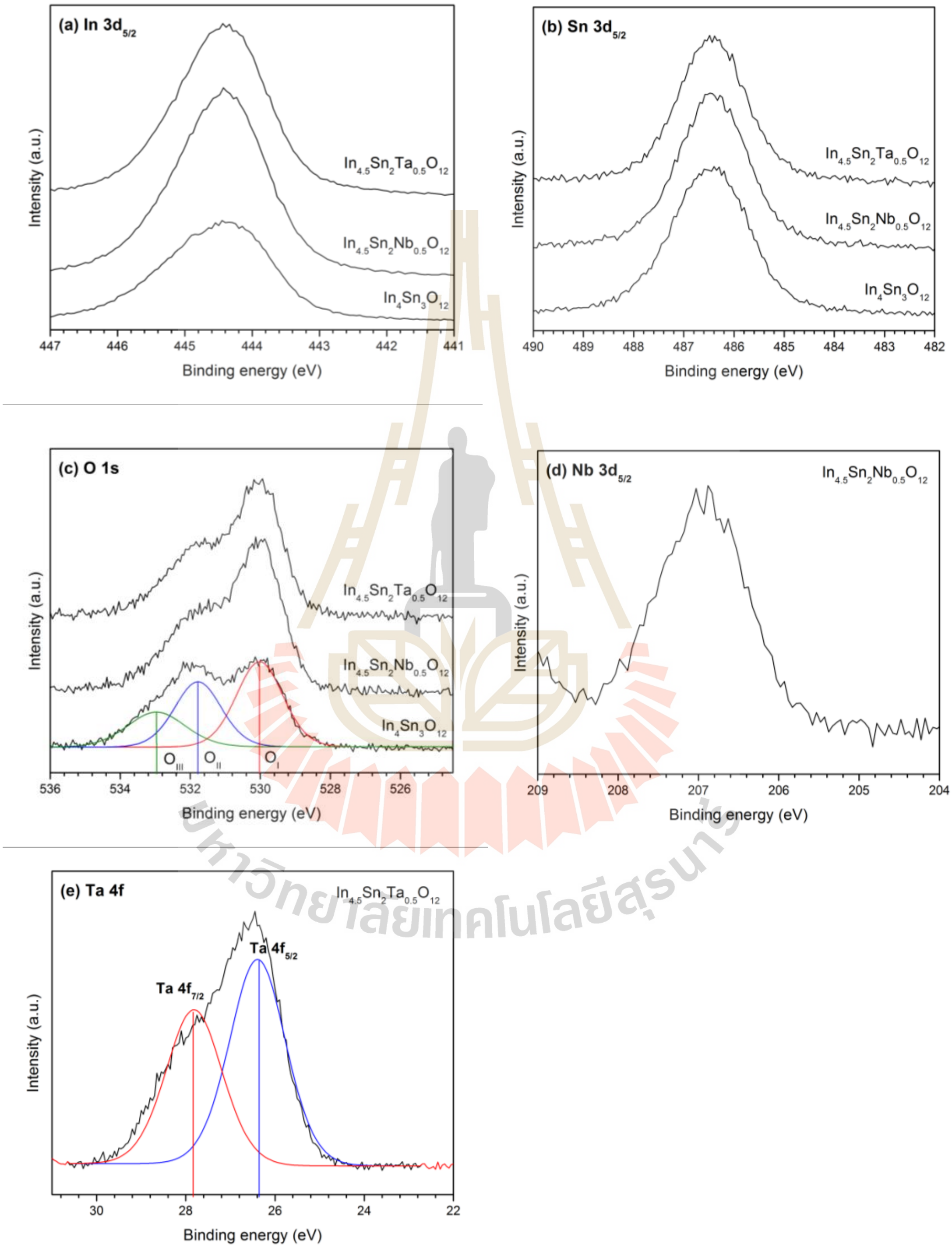

Figure 4.5 High-resolution XPS spectra of (a) In $3d_{5/2}$, (b) Sn $3d_{5/2}$, (c) O 1s, (d) Nb $3d_{5/2}$ and (e) Ta $4f_{7/2}$ of $In_4Sn_3O_{12}$, $In_{4.5}Sn_2Nb_{0.5}O_{12}$ and $In_{4.5}Sn_2Ta_{0.5}O_{12}$.

(Figure 4.5(c)) can be deconvoluted into three peaks. The first O_I peak at ~530.02 eV can be indexed as O^{2-} in lattice. The second O_{II} peak at ~531.78 eV is assigned as oxygen vacancy and oxygen in C-O bond from surface contamination during sample preparations for the measurement. The O_{III} peak at ~532.97 eV can be identified as loosely bound oxygen species such as adsorbed O_2, -OH or O-contained organic species (Song *et al.*, 2001; Gan *et al.*, 2013; Hoch *et al.*, 2014; Park *et al.*, 2015; He *et al.*, 2013). In case of doped samples, Nb $3d_{5/2}$ peak of 206.96 eV (Figure 4.5(d)) (Nefedov *et al.*, 1974) and Ta $4f_{7/2}$ peak of 26.39 eV (Figure 4.5(e)) (Sarma and Rao, 1980) are interpreted as Nb^{5+} and Ta^{5+}, respectively.

4.5.2 Optical properties

Figure 4.6a shows the UV-Vis absorption spectra of all samples, which exhibit sharp absorption edge. The DFT band structure calculation suggests that the direct allowed transition is observed for $In_4Sn_3O_{12}$ (Ren *et al.*, 2006; Zhang and Wang, 2011). The UV-Visible diffuse reflectance (%R) spectra (not shown here) of all samples were collected and Kubelka-Munk function $F(R_\alpha) = (1-R_\alpha)^2/2R_\alpha$, where R is reflectance and $R_\alpha = R_{sample}/R_{reference}$, is used to obtain the band gap energy. The plots of $[F(R_\alpha)h\upsilon]^{1/n}$ vs. $h\upsilon$ when n = 1/2 corresponding to direct allowed transition and the direct E_g are shown as Figure 4.6b. The band gap energy of $In_4Sn_3O_{12}$ is 2.89 eV. By the substitution with Nb and Ta, the band gap energies become larger (3.02 eV and 3.08 eV, repectively). This is evidenced from the color as well; the undoped sample is light green while the doped samples are pale green.

The emission peak at around 2.6 eV is observed from the photoluminescence spectra (Figure 4.7) for all samples. This corresponds to the near band edge transition, which is the emission of excited electrons from the sub-bands or surface state near the conduction band to the highest energy state an electron can exist in the valence band. The emitted energy is slightly lower than their band gap energies because of non-radiative relaxation like thermal vibration, which can be ascribed as Strokes shift due to Franck-Condon effects (Liqiang *et al*., 2006; Zhang *et al*., 2011). Furthermore, two shoulders observed over two regions. The fist shoulder covered the area of 2.2-2.4 eV could be attributed to oxygen vacancy (Zhou *et al*., 1999; Papageorgiou *et al*., 2011; Alberto Ramos Ramón *et al*., 2015). The second shoulder seen at around 3 eV appears apparently for doped samples could be the charge transfer of In^{3+}-O (De Bruin *et al*., 1993) and Sn^{4+}-O (Gu *et al*., 2004; Lai *et al*., 2009).

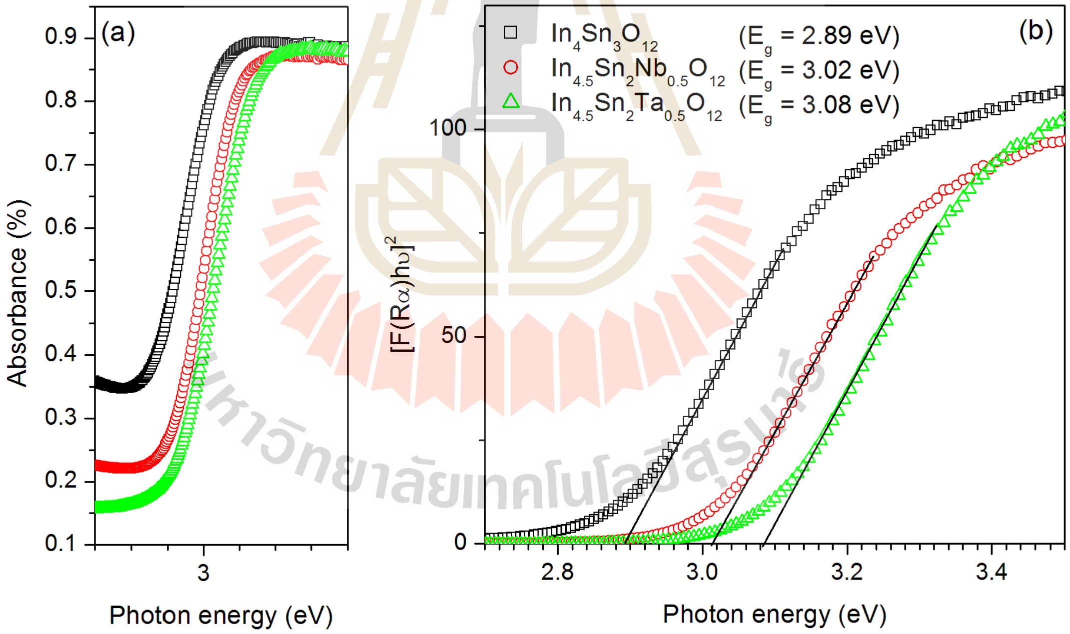

Figure 4.6 UV-Vis absorption spectra (a) and Kubelka-Munk plots (b) of $In_4Sn_3O_{12}$ and $In_{4+x}Sn_{3-2x}M_xO_{12}$ (M = $Nb_{0.5}$, $Ta_{0.5}$).

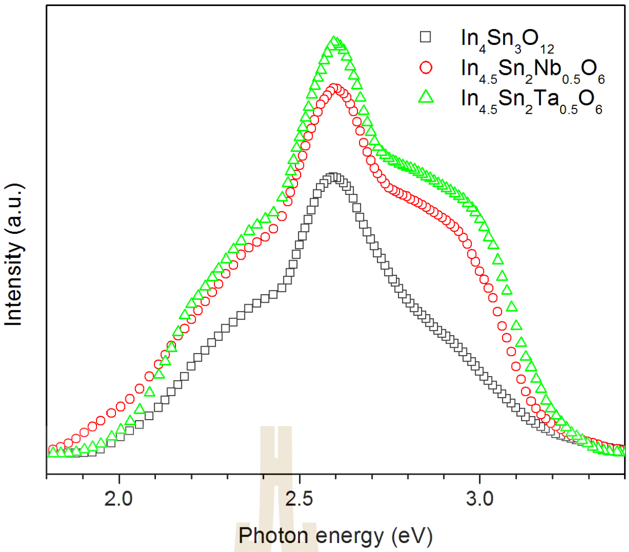

Figure 4.7 Photoluminescence spectra of $In_4Sn_3O_{12}$ and $In_{4+x}Sn_{3-2x}M_xO_{12}$ (M = $Nb_{0.5}$, $Ta_{0.5}$).

4.5.3 Electrical properties

$In_4Sn_3O_{12}$ prepared in this work has the resistivity of 3.24×10^{-2} Ω.cm, which is similar to those reported in other works (Choisnet *et al*., 2004; Nadaud *et al*., 1998; Pitschke *et al*., 2000). The substitution of Nb^{5+} and Ta^{5+} for $In_4Sn_3O_{12}$ with the formula $In_{4+x}Sn_{3-2x}M_xO_{12}$ (M = Nb and Ta) should not create any extra charger carriers. Nevertheless, such small substitutions significantly affect the resistivity of substituted-compounds (Table 4.3).

To the best of our knowledge, the semiconducting behavior in $In_4Sn_3O_{12}$ has not been clarified. One possible explanation is the intrinsic oxygen vacancy. As this phase is prepared at high temperature, it might be possible to lose oxygen because non-stoichiometric oxygen-deficient In_2O_3 was also found at high temperatures (De Wit, 1977). In addition, it was found that the resistivity of all samples decreases after N_2 annealing at 900 °C for 3 hours (Table 4.3). Since no impurity was detected in XRD patterns of the annealed samples (not shown here), the conductivity must come from the major phase whose structure remain unchanged. Although the conductivity is related to both the carrier density and the carrier mobility, such dramatic changes in the numbers indicate that the first factor plays more important role here.

It is unlikely that In, Sn, Ta, or Nb have mixed valency, therefore, the electronic conductivity most likely stems from the presence of oxygen vacancies. It should be noted that the highest intensity of O_{II} peak in O XPS spectra which implies the oxygen vacancy content is observed in the most conducting sample.

Table 4.3 Electrical resistivity of $In_4Sn_3O_{12}$ and $In_{4+x}Sn_{3-2x}M_xO_{12}$ (M_x = $Nb_{0.5}$, $Ta_{0.5}$) before and after N_2 annealing at 900 °C for 3 hours.

Samples	Resistivity (Ω.cm)	
	Before N_2 annealing	After N_2 annealing (3 h)
$In_4Sn_3O_{12}$	3.24×10^{-2}	1.07×10^{-2}
$In_{4.5}Sn_2Nb_{0.5}O_{12}$	1.31×10^{5}	6.01×10^{2}
$In_{4.5}Sn_2Ta_{0.5}O_{12}$	1.62×10^{3}	1.85×10

4.5.4 Calculation studies

The electronic structures of pure and doped systems were further examined using DFT calculations. As shown in Figure 4.8a, the calculated band structure of pure $In_4Sn_3O_{12}$ along the high-symmetry directions of the Brillouin zone exhibits a direct band gap of 1.01 eV at the Γ point which is consistent with other calculated PBE values (1.12 eV and 1.2 eV) but significantly lower than that of the experimental value (2.89 eV). Such a large underestimation originates from the use of approximate exchange-correlation functional which fails to cancel exactly the self-interaction energy. The conduction band minimum (CBM), centered at the Γ point, lies rather low in energy compared with the average energy of the band edge across the Brillouin zone resulting in a relatively high band-edge curvature and a light effective mass.

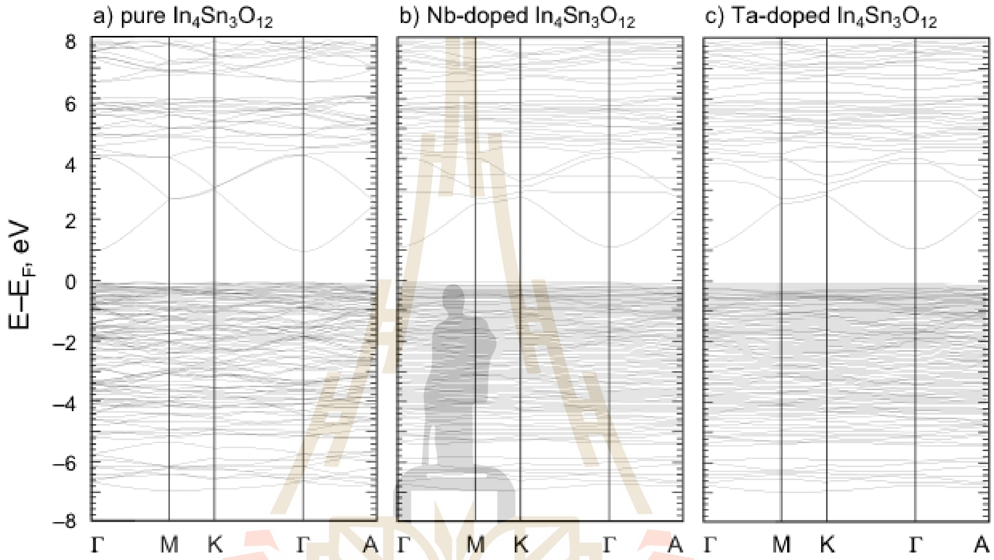

Figure 4.8 Calculated band structures along the high symmetry points in the Brillouin zone of a) pure, b) Nb-doped and c) Ta-doped $In_4Sn_3O_{12}$.

The band structures of the doped systems display similar features to that of the pure $In_4Sn_3O_{12}$ system, as shown in Figure 4.8 panel b and c. Nevertheless, their CBM are flatter than that of the pure system leading to larger effective masses for Nb-doped and Ta-doped systems. The calculated results indicate that Nb and Ta doping lower the electron mobility in the material which could be one factor that diminishes the electronic conductivity of the doped samples.

To obtain insight into the bonding properties of pure and doped $In_4Sn_3O_{12}$, we computed and analysed their total and projected density of states (DOS). As shown in Figure 4.9a, the calculated DOS of pure $In_4Sn_3O_{12}$ exhibits semiconducting behavior with a band gap of 1.01 eV. The valence band develops its overall character from O 2p states. At the bottom of the valence band, energy ranges from -6.9 eV to -5.4 eV, significant hybridisation between cation s states and O 2p states occurs. Non-negligible metal 4d states were also found to strongly hybridise with O 2p states at the top of the valence band. The conduction band is predicted to be relatively diffuse since it mainly comprises the admixture of the cation 5s states and O 2p with a rather large bandwidth of 5.2 eV.

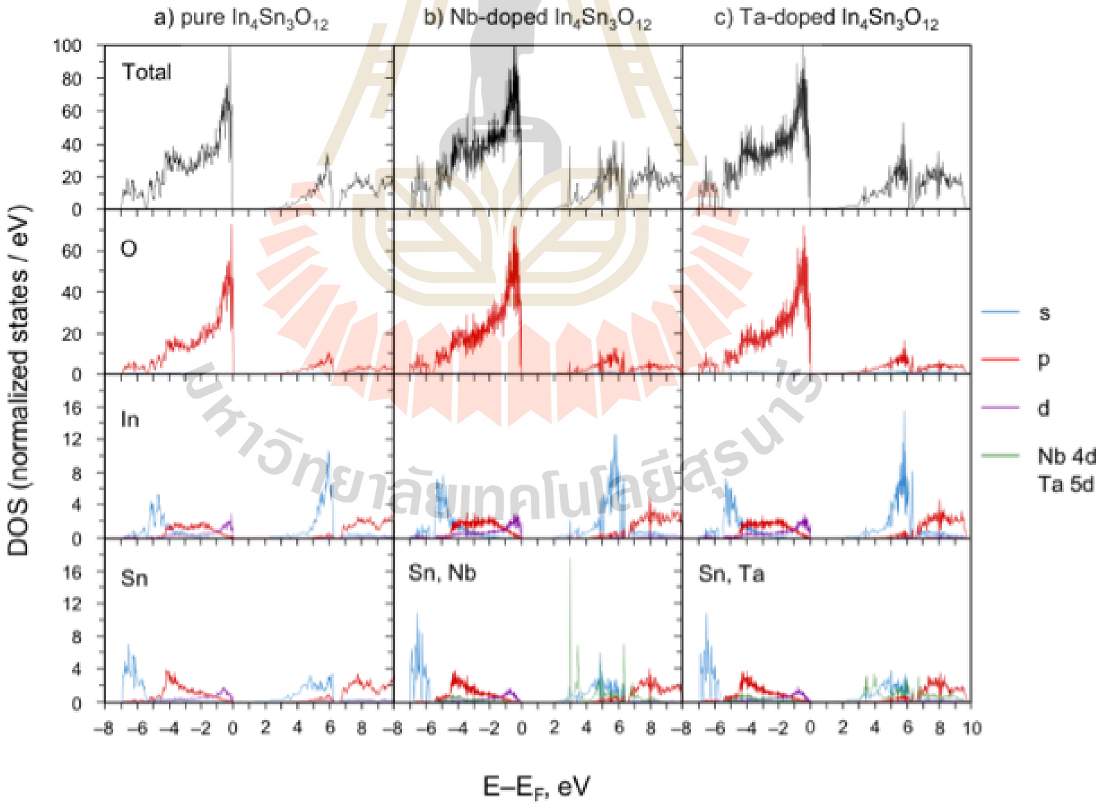

Figure 4.9 Calculated total and projected density of states of a) pure, b) Nb-doped and c) Ta-doped $In_4Sn_3O_{12}$.

Introduction of Nb or Ta dopant into the $In_4Sn_3O_{12}$ lattice does not generate any charge carriers since they are compensated by a higher In/Sn ratio in the samples as previously discussed. Hence, the DOS of the doped systems maintain their semiconducting character where the main features of the DOS are similar to that of the pure system. The only key distinct is the established Nb 4d and Ta 5d states at the bottom of the conduction band as shown in Figure 4.9 panel b and c, respectively. The contributions of relatively localised d states from the metal dopants may reduce the mobility of conducting electrons which reflects through the heavier effective masses obtained from the calculated band structures.

4.6 Conclusions

Undoped and M-doped $In_4Sn_3O_{12}$ with the formula $In_{4-x}Sn_{3-2x}M_xO_{12}$ (M_x = $Nb_{0.5}$ and $Ta_{0.5}$) have been successfully prepared by solid state reaction at 1400-1450 °C in air. The obtained XRD patterns of all samples confirms the pure phase formation of $In_4Sn_3O_{12}$ related structure. The substitution of In and Sn by Nb/Ta results in the increase of the mol ratio of In/Sn, which illustrates through the increase in cell parameters *a*, *c* and cell volume. The oxidation states of all elements were determined by XPS: In^{3+}, Sn^{4+} and Nb^{5+}/Ta^{5+}. In case of O, the O 1s XPS spectra can be deconvoluted to three components of O-lattice, O vacancy/O-C (contamination) and adsorbed O species such as O_2, -OH and O-contained organic compounds. The optical band gap energy of doped samples were larger than that of undoped samples. This can be seen by their colours: the undoped sample was light green while those of doped samples were pale green. The observed photoluminescence spectra reveal the possible defects in samples, which can be oxygen deficiency and charge transfer of In-O and Sn-O components. The electrical resistivity obtained in undoped compound was lower than that in Nb-doped and Ta-doped compounds. Oxygen vacancy defect was proposed to be the main cause of electrical conduction. The computational study was utilised to gain deep understanding accordingly. The calculated energy of oxygen vacancy formation was higher in case of doped systems. Moreover, the DFT band structures were investigated and no significant difference was obtained after Nb/Ta doping. Flatter CBM observed in doped samples suggests the smaller carrier mobility could be obtained and thus heighten the electrical resistivity. However, the great difference resistivities obtained between doped and undoped systems suggests that the main factor affecting the resistivities was carrier density. The projected DOS provides additional data on bonding contributions: cation 4d states were strongly admixed with O 2p states at VBM and the hybridysation of cation 5s states and O 2p was found at CBM.

4.7 References

Alberto Ramos Ramón, J., León Sánchez, D., Herrera Zaldívar, M. and Pal, U. (2015). Morphology and defect evolution in vapor-grown In_2O_3:Sn micro-/nanoparticles. **Materials Science in Semiconductor Processing**. 40: 943–953.

Ansell, R. O., Dickinson, T., Povey, A. F. and Sherwood, P. M. A. (1977). Quantitative use of the angular variation technique in studies of tin by X-ray photoelectron spectroscopy. **Journal of Electron Spectroscopy and Related Phenomena**. 11: 301–313.

Bates, J. L., Griffin, C. W., Marchant, D. D. and Garnier, J.E. (1986). Electronic conductivity, Seebeck coefficient, defect, and structure of In_2O_3-SnO_2. **American**

Ceramic Society Bulletin. 65: 4.

Behr, G. and Krabbes, G. (1996). Abschlußbericht zum DFG-Förderprojekt Kr1241/1-1 und Be 1749/1-3. In **Abschlußbericht zum DFG-Förderprojekt Kr1241/1-1 und Be 1749/1-3**. Dresden.

Bertrand, P. A. (1981). XPS study of chemically etched GaAs and InP. **Journal of Vacuum Science and Technology**. 18: 28.

Blöchl, P. E. (1994). Projector augmented-wave method. **Physical Review B**. 50: 17953–17979.

Choisnet, J., Bizo, L., Allix, M., Rosseinsky, M. and Raveau, B. (2007). Cation ordering in the fluorite-like transparent conductors $In_{4+x}Sn_{3-2x}Sb_xO_{12}$ and In_6TeO_{12}. **Journal of Solid State Chemistry**. 180: 1002–1010.

Choisnet, J., Bizo, L., Retoux, R., Hébert, S. and Raveau, B. (2004). New transparent conductors with the M_7O_{12} ordered oxygen-deficient fluorite structure: from $In_4Sn_3O_{12}$ to $In_{5.5}Sb_{1.5}O_{12}$. **Journal of Solid State Chemistry**. 177: 3748–3751.

De Bruin, T. J. M., Wiegel, M., Dirksen, G.J. and Blasse, G. (1993). Luminescence of Li_2ZrTeO_6. **Journal of Solid State Chemistry**. 107: 397–400.

De Wit, J. H. W. (1977). Structural aspects and defect chemistry in In_2O_3. **Journal of Solid State Chemistry**. 20: 143–148.

Fan, J. C. C. and Goodenough, J. B. (1977). X-ray photoemission spectroscopy studies of Sn-doped indium-oxide films. **Journal of Applied Physics**. 48: 3524–3531.

Gan, J., Lu, X., Wu, J., Xie, S., Zhai, T., Yu, M., and Tong, Y. (2013). Oxygen vacancies promoting photoelectrochemical performance of In_2O_3 nanocubes. **Scientific Reports**. 3: 1021.

Ginley, D. S. and Perkins, J. D. (2011). Transparent Conductors. In **Handbook of transparent conductors**.

Gu, F., Wang, S. F., Lü, M. K., Zhou, G. J., Xu, D. and Yuan, D. R. (2004). Photoluminescence properties of SnO_2 nanoparticles synthesized by sol-gel method. **Journal of Physical Chemistry B**. 108: 8119–8123.

He, L., Wu, Z., Li, Z., Ju, J., Ou, Q. and Liang, R. (2013). Surface work function of indium tin oxide treated using plasma immersion ion implantation. **Journal of Physics D: Applied Physics**. 46.

Hoch, L. B., Wood, T. E., O'Brien, P. G., Liao, K., Reyes, L. M., Mims, C. A. and Ozin, G. A. (2014). The Rational Design of a Single-Component Photocatalyst for Gas-Phase CO_2 Reduction Using Both UV and Visible Light. **Advanced Science**. 1: 1400013.

Joubert, D. (1999). From ultrasoft pseudopotentials to the projector augmented-wave method. **Physical Review B - Condensed Matter and Materials Physics**. 59: 1758–1775.

Kresse, G. and Furthmüller, J. (1996a). Efficient iterative schemes for ab initio total-energy calculations using a plane-wave basis set. **Physical Review B - Condensed Matter and Materials Physics**. 54: 11169–11186.

Kresse, G. and Furthmüller, J. (1996b). Efficiency of ab-initio total energy calculations for metals and semiconductors using a plane-wave basis set. **Computational Materials Science**. 6: 15–50.

Kresse, G. and Hafner, J. (1993). Ab initio molecular dynamics for liquid metals. **Physical Review B**. 47: 558–561.

Lai, M., Lim, J.-H., Mubeen, S., Rheem, Y., Mulchandani, A., Deshusses, M. and Myung, N. V. (2009). Size-controlled electrochemical synthesis and properties of SnO2 nanotubes. **Nanotechnology**. 20: 185602.

Lin, A. W. C., Armstrong, N. R. and Kuwana, T. (1977). X-ray Photoelectron/Auger

Electron Spectroscopic Studies of Tin and Indium Metal Foils and Oxides. **Analytical Chemistry**. 49: 1228–1235.

Liqiang, J., Yichun, Q., Baiqi, W., Shudan, L., Baojiang, J., Libin, Y. and Jiazhong, S. (2006). Review of photoluminescence performance of nano-sized semiconductor materials and its relationships with photocatalytic activity. **Solar Energy Materials and Solar Cells**. 90: 1773–1787.

Minami, T., Takeda, Y., Takata, S. and Kakumu, T. (1997). Preparation of transparent conducting $In_4Sn_3O_{12}$ thin films by DC magnetron sputtering. **Thin Solid Films**. 308–309: 13–18.

Monkhorst, H. and Pack, J. (1976). Special points for Brillouin zone integrations. **Physical Review B**. 13: 5188–5192.

Mryasov, O. and Freeman, A. (2001). Electronic band structure of indium tin oxide and criteria for transparent conducting behavior. **Physical Review B**. 64: 233111.

Nadaud, N., Lequeux, N., Nanot, M., Jové, J. and Roisnel, T. (1998). Structural studies of tin-doped indium oxide (ITO) and In4Sn3O12. **Journal of Solid State Chemistry**. 135: 140–148.

Nefedov, V. I., Salyn, Y. V, Chertkov, A. A. and Padurets, L. N. (1974). The x-ray electronic study of the distribution of electron density in transition element hydrides. **Zh. Neorg. Khim.** 19: 1443–1445.

O'Neil, D. H., Kuznetsov, V. L., Jacobs, R. M. J., Jones, M. O. and Edwards, P. P. (2010). Structural, optical and electrical properties of $In_4Sn_3O_{12}$ films prepared by pulsed laser deposition. **Materials Chemistry and Physics**. 123: 152–159.

Papageorgiou, P., Zervos, M. and Othonos, A. (2011). An investigation into the conversion of In_2O_3 into InN nanowires. **Nanoscale Research Letters**. 6.

Park, J.-W., So, H. S., Lee, H.-M., Kim, H.-J., Kim, H.-K. and Lee, H. (2015). Transition from a nanocrystalline phase to an amorphous phase in In-Si-O thin films: The correlation between the microstructure and the optical properties. **Journal of Applied Physics**. 117: 155305.

Pitschke, W., Werner, J., Behr, G. and Koumoto, K. (2000). Structure and Thermoelectric Properties of Me-Substituted $In_4Sn_3O_{12}$, Me = Y and Ti. **Journal of Solid State Chemistry**. 153: 349–356.

Ren, C.-Y., Chiou, S.-H. and Choisnet, J. (2006). First-principles calculations of the electronic band structure of $In_4Sn_3O_{12}$ and In_5SnSbO_{12}. **Journal of Applied Physics**. 99: 23706.

Sarma, D. D. and Rao, C. N. R. (1980). XPES studies of oxides of second- and third-row transition metals including rare earths. **Journal of Electron Spectroscopy and Related Phenomena**. 20: 25–45.

Shannon, R. D. (1976). Revised effective ionic radii and systematic studies of interatomic distances in halides and chalcogenides. **Acta Crystallographica Section A**. 32: 751–767.

Song, W., So, S. K. and Cao, L. (2001). Angular-dependent photoemission studies of indium tin oxide surfaces. **Applied Physics A: Materials Science and Processing**. 72.

Xiao, G., Nuansaeng, S., Zhang, L., Suthirakun, S., Heyden, A., Loye, H.-C. zur and Chen, F. (2013). Enhanced reducibility and conductivity of Na/K-doped $SrTi_{0.8}Nb_{0.2}O_3$. **Journal of Materials Chemistry A**. 1: 10546.

Zhang, J., Chen, X., Shen, Y., Li, Y., Hu, Z. and Chu, J. (2011). Synthesis, surface morphology, and photoluminescence properties of anatase iron-doped titanium dioxide nano-crystalline films. **Physical Chemistry Chemical Physics**. 13: 13096.

Zhang, Y. G. and Wang, Y. X. (2011). Density-Functional Study of the Electronic

Structure and Optical Properties of Transparent Conducting Oxides $In_4Sn_3O_{12}$ and $In_4Ge_3O_{12}$. **Journal of Electronic Materials**. 40: 1501–1505.

Zhou, H., Cai, W. and Zhang, L. (1999). Photoluminescence of indium-oxide nanoparticles dispersed within pores of mesoporous silica. **Applied Physics Letters**. 75: 495–497.

CHAPTER V

PHOTOCATALYTIC AND ELECTRICALLY CONDUCTIVE TRANSPARENT Cl-DOPED ZnO THIN FILMS *via* AEROSOL-ASSISTED CHEMICAL VAPOUR DEPOSITION

5.1 Abstract

A simple, economical and effective solution-based chemical vapour deposition (CVD) technique, aerosol-assisted CVD, has been successfully applied to produce inexpensive Cl-doped ZnO films using Zn acetate dihydrate and $FeCl_3$. X-ray photoelectron spectroscopy and the increase in cell parameters from powder X-ray diffraction determined that Cl had been doped into the wurtzite ZnO lattice. The Cl-doping had a significant effect on the morphology of the thin films synthesised and resulted in an improvement in the visible light transmission and lower electrical resistance (typical resistivities of doped films ~10^{-2} Ω.cm). The highest transmittance (%T) of 85% was obtained when 7 mol% $FeCl_3$ was used in the precursor solution and the lowest resistivity of $4.28 \pm 0.41 \times 10^{-2}$ Ω.cm was obtained with 5 mol% $FeCl_3$. The greatest photocatalytic activity of stearic acid degradation under UVA irradiation was obtained on using 10 mol% $FeCl_3$, resulting in the highest formal quantum efficiency (FQE) of $3.0 \pm 0.1 \times 10^{-4}$ molecule/photon. These films, therefore, display transparent

conducting oxide and photocatalytic properties, giving multifunctional characteristics and promising applications.

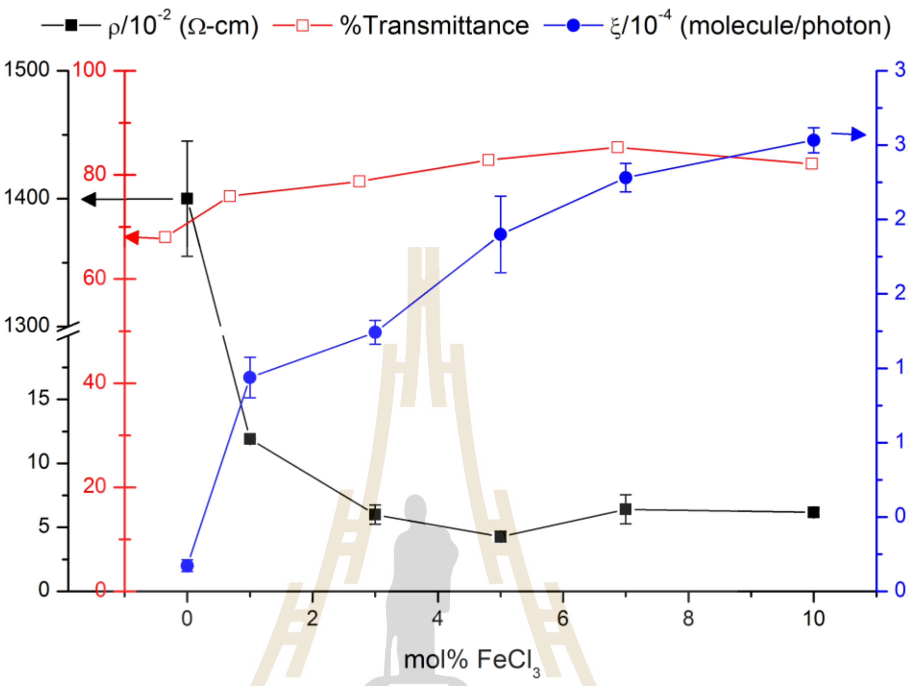

Figure 5.1 Cl-doped ZnO films, grown via aerosol-assisted CVD, are shown to have potential application as both TCOs and photocatalysts.

5.2 Introduction

Transparent conducting oxide (TCO) materials have the unique coexistent properties of high optical transparency and high electrical conductivity that contribute to various electronic devices such as liquid crystal displays (LCDs), touch panel screens, E-paper, defrosting windows, electrochromic windows and mirrors, photovoltaics, flexible electronics and invisible security circuits (Gordon, 2000; Ginley and Perkins, 2011). Semiconducting oxides with large band gap energies (>3.1 eV) and the ability to be doped to generate low resistivity ($<10^{-2}$ Ω.cm) are required for TCO properties (Dixon *et al*., 2016) Even though Sn-doped In_2O_3 (ITO) and F-doped SnO_2 (FTO) are the most widely used TCOs because of their excellent properties of low electrical resistivity with high transparency (Gordon, 2000; Granqvist and Hultåker, 2002; Bhachu *et al*., 2011; Lin *et al*., 2009), In_2O_3 has the disadvantages of high cost of extraction and processing, as well as concern over the relative scarcity of indium ores. Sn also has also suffers from price fluctuations compared to others elements, such as Zn (U.S. Department of the Interior and U.S. Geological Survey, 2017).

Zinc oxide (ZnO) is a promising candidate for TCOs because it is well known as an intrinsic *n*-type semiconductor with a wide band gap of *ca*. 3.37 eV; moreover, it has high thermal stability (Hu and Gordon, 1992), is inexpensive, earth abundant and relatively nontoxic compared to ITO and FTO (Hu and Gordon, 1992; Ghandhi *et al*., 1980; Hollingsworth *et al*., 2010; McNally *et al*., 2012; Waugh *et al*., 2008). Doping is a strategy to enhance the electrical conductivity of TCO materials. Cation dopants such as Al^{3+}, Ga^{3+}, In^{3+} (Manzi *et al*., 2016; Kuprenaite *et al*., 2015; Potter *et al*., 2016; Ponja *et al*., 2014; Potter *et al*., 2018; Howard *et al*., 2017; Howard *et al*., 2016), Sc^{3+} (Dixon *et al*., 2017), Si^{4+} (Potter *et al*., 2017; Howard *et al*., 2017) and Cu (Walters and Parkin, 2009) and anion dopants such as F^- (Ponja *et al*., 2014; Yates *et al*., 2015; Xu *et al*., 2005), Cl^- (Rousset *et al*., 2009) and N^{3-} (Yang *et al*., 2009) have all been successfully incorporated into ZnO thin films. Anion doping is considered to be a superior route to obtain high carrier concentration and mobility while maintaining high transparency, because the conduction band is less perturbed by the dopant and thus the scattering of electrons in the conduction band is minimised (Gordon, 2000). F-doping has been extensively studied and the resulting materials show excellent properties (Bhachu *et al*., 2011; Mohri *et al*., 2012; Hu and Gordon, 1991). Investigations on the use of other anions, such as Cl, are relatively limited. However, there have been some reports on the electrical, optical and photoelectrochemical properties of Cl-doped ZnO, which show the potential of Cl doping (Lee *et al.*, 2013; Chikoidze *et al.*, 2008; Choi *et al.*, 2015; Lee *et al.*, 2012; Chikoidze *et al.*, 2008; Rousset *et al.*, 2011). Therefore, we were interested in exploring further the novel properties of ZnO:Cl, in particular the film deposition method which has been shown to play a key role in modifying the film properties. Aerosol-assisted chemical vapour deposition (AACVD) is an effective technique to control the morphology and simultaneously the properties of the deposited films (Marchand *et al.*, 2013). Moreover, it is a simple, sustainable and scalable deposition film fabrication technique (Powell and Carmalt, 2017) that allows for the use of a variety of precursors with appropriate solubility in a suitable solvent (Waugh *et al.*, 2008) In the procedure, soluble halide precursors can be utilised which are generally cheaper than metal-organic precursors (Yan and Xu, 2010).

In general, TCO films have poor photocatalytic activity and photocatalytic films show poor TCO properties (Kafizas *et al.*, 2014). For example, W-doped TiO_2 and Nb-doped TiO_2 films are good photocatalysts and electrically conductive (resistivities were $6.3 \times 10^{-1} – 6.3 \times 10^{-2}$ Ω.cm and $5.8 \times 10^{-2} – 1.3 \times 10^{-3}$ Ω.cm, respectively) but they are coloured (Sathasivam *et al.*, 2015; Bhachu *et al.*, 2014), P-doped TiO_2 films are also good photocatalysts but their conductivity (resistivities were 1.69-6.49 Ω.cm) as well as transparency (%T is less than 80%) have not yet passed the requirement to be considered good TCO materials (Sotelo-Vazquez *et al.*, 2015). In general, multifunctional properties are not commonly observed in most films. The ability to synthesise films that display both good electrical and photocatalytic properties whilst being transmissive of visible wavelengths would therefore be of benefit for multifunctional devices.

Here, the Cl-doped ZnO films were prepared by a simple, economical and potential film deposition, AACVD technique for the first time. Photocatalytic properties of ZnO:Cl films are first observed. Self-cleaning transparent conducting Cl-doped ZnO thin films are described as promising materials for sustainable applications.

5.3 Experimental

5.3.1 Film synthesis

All films were synthesised *via* aerosol assisted chemical vapor deposition (AACVD). Zn(II) acetate dihydrate, $Zn(OAc)_2•2H_2O$, (≥98%, Sigma-Aldrich) and Ferric chloride anhydrous, $FeCl_3$, (98%, Aldrich) were used as the Zn and Cl precursors respectively. All precursors were used as received without further purification. Methanol (99.9%, Fisher Scientific) was used as the solvent. Nitrogen gas (99.99%, BOC) was used as the carrier gas.

In a typical deposition, the precursor solution was prepared by dissolving $Zn(OAc)_2•2H_2O$ (0.50 g, 2.28 mmol) in methanol (20 mL). $FeCl_3$ was dissolved in methanol and then added to the zinc acetate solution in the corresponding mol% of 0, 1, 3, 5, 7, 10 and 15. Each precursor was stirred until separately for *ca*. 5 minutes and then mixed by stirring to give the final precursor solution. A glass substrate, coated with a 50 nm SiO_2 barrier layer (NSG Pilkington Ltd), with the dimension of 3.2 mm × 45 mm × 100 mm was used. The SiO_2 barrier layer is important to prevent leeching of ions between the substrate and the film. Prior to depositing, the substrate was cleaned by detergent, isopropanol and acetone, respectively. The AACVD apparatus is illustrated in Figure 5.2. The substrate was placed on a carbon heating block, which was enclosed in a quartz tube. The top plate of stainless steel of 4.8 cm × 15 cm was suspended over the substrate approximately 8 mm to assist the laminar flow of the aerosol. In the deposition, the obtained precursor solution was atomised using a ‘Liquifog’ piezo ultrasonic humidifiers (Johnson Matthey). The aerosol or mist was generated and transported to the heated substrate through the baffle *via* nitrogen carrier gas with a flow rate of 1.5 L/min. The deposition temperature was 500 ºC for all samples. A typical deposition would take 15-20 minutes in order to for all of the solution to aerosolise, after which the substrate was left to cool under a continuous flow of nitrogen gas and removed when the temperature of reactor was below 100 ºC. The film was cut into pieces of 1 × 1 cm^2 prior to the characterisations.

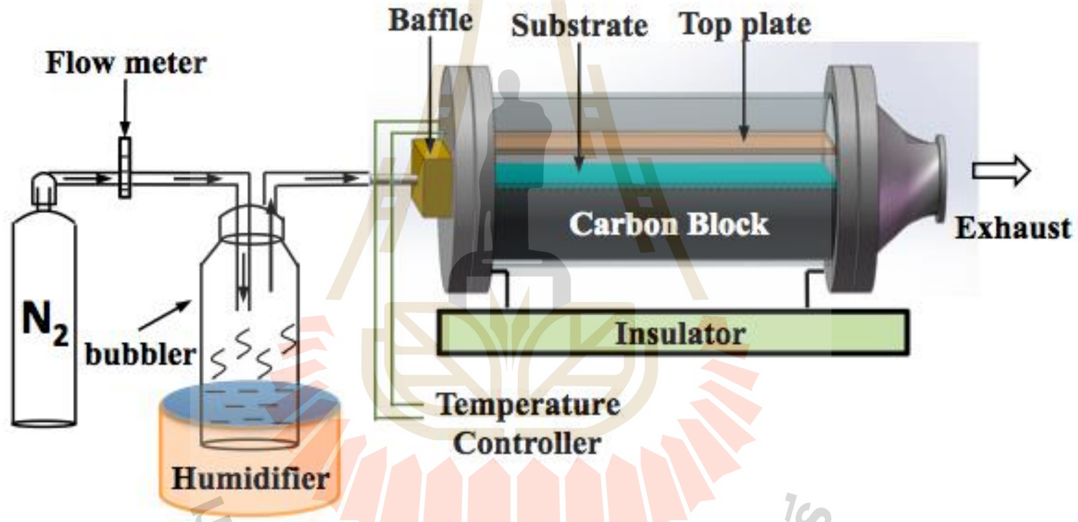

Figure 5.2 The schematic illustration of aerosol assist chemical vapour deposition (AACVD) apparatus.

5.3.2 Film characterisations

X-ray photoelectron spectroscopy (XPS) spectra of Zn 2p, Fe 2p, Cl 2p and O 1s were investigated to confirm the oxidation states as well as compositions of constituent elements. A Thermo Scientific K-alpha spectrometer with a monochromatic Al Kα radiation, a dual beam charge compensation system and constant pass energy of 50 eV were utilised. The collected spectra were fitted using CasaXPS software. The C 1s peaks at 284.5 eV were used as reference for binding energy calibration. X-ray diffraction (XRD) measurement, using a Bruker-Axs D8 X-ray diffractometer with parallel beam optics equipped with a PSD LynxEye silicon strip detector, was performed to check the phase purity of the films. Monochromatic Cu $K_{\alpha 1}$ and $K_{\alpha 2}$ X-rays (λ = 1.54056 Å and 1.54439 Å, respectively), with the intensity ratio of 2:1, were generated using a voltage of 40 kV and a current of 40 mA. The incident beam angle was kept at a grazing setup of 1°. XRD patterns were collected with 2θ range of 10-66° with a step size of 0.05° by a scan rate of 4s/step. Le Bail refinement using GSAS and EXPGUI software (Larson and Von Dreele, 2004; Toby, 2001) was done to get the cell parameters. Scanning electron microscope (SEM) images and side-on SEM images were gained to study the surface morphology and film thickness, respectively, using a JEOL JSM-6301F Field Emission instrument with an operated acceleration voltage of 10 kV. UV/Vis transmittance spectra were measured to obtain the optical properties by using a Perkin Elmer Lambda 950 UV/Vis/NIR Spectrophotometer. Surface topology and roughness (root mean squared, R_q) were characterised using an atomic force microscope (AFM, Bruker Multimode 8). The tips were used in the ScanAsyst tapping mode to scan the area of 1.0 µm × 1.0 µm, respectively, with 512 scans.

Hall effect measurement with the Van der Pauw method was carried out on an Ecopia HMS-3000 to investigate the electrical properties: resistivity (ρ), carrier concentration (n) and carrier mobility (μ). A magnetic field of 0.58 T and an input current of 1 µA - 1 mA were applied for the measurement.

To determine the photocatalytic properties, the test of stearic acid degradation was studied. A thin layer of stearic acid was coated on films by dipping in a 0.05 M stearic acid solution in chloroform using a bespoke dip coating apparatus, which withdraws the substrate at a fixed rate vertically from the stearic acid solution. Fourier transform infrared (FTIR) spectra were collected in the absorbance mode in the range of 2700-3000 cm^{-1}, using a Perkin Elmer RX-I instrument, to monitor the C-H bond decomposition under UVA (λ = 365 nm) light exposure. A 2 × 8 W blacklight-bulb (BLB) UVA lamps (*Vilber-Lourmat*) with the irradiation of ~0.5 mW cm^{-2}, as measured by a UVX meter (*UVP*), were used in the test. The linear regression of the initial 30-40% degradation steps (zero-order kinetics) with a conversion factor (1 cm^{-1} $\approx$ 9.7 x 10^{15} molecule of stearic acid/cm^{2}) (Mills and Wang, 2006) was utilised to determine the photocatalytic activity rates as formal quantum efficiency (FQE) value.

5.4 Results and discussion

5.4.1 Film synthesis

In the synthesis, the precursors $Zn(OAc)_2{\cdot}2H_2O$ and $FeCl_3$ were dissolved in methanol. At low concentrations (below 5 mol%) of $FeCl_3$ the solution was clear and colourless. However, at higher concentrations (>5 mol% of $FeCl_3$) some white colloid was observed in the mixed solution. The undoped ZnO films deposited were typically darker in hue than the doped films. This was attributed to higher carbon contamination in the undoped films, which was confirmed by the presence of C 1s XPS spectra in the bulk of films. The prepared films become more transparent with increasing the amount of $FeCl_3$. Figure 5.3 shows a photograph of the most transparent films prepared using 7 mol% $FeCl_3$ in the solution precursor (right) compared with bare glass (left). The 15 mol% $FeCl_3$-loaded precursor solution resulted in the deposition of a hazy film and hence it was not further characterised for optical and electrical properties.

Figure 5.3 Photograph of bare glass (left) and 7 mol% $FeCl_3$ loaded ZnO film (right).

All the films had good adhesion to the substrate, passing the Scotch tape test and steel scalpel scratch test. The films showed good stability after six months storage under ambient condition and they were stable to common solvents such as methanol, isopropanol, acetone and chloroform. All films were deposited at 500 °C, since this temperature resulted in films with the optimum appearance, good coverage and the best electrical properties, in comparison to films deposited at 400 °C and 550 °C.

5.4.2 Elemental analysis

The chemical components and their oxidation states were studied by X-ray photoelectron spectroscopy (XPS) which indicated that Cl-doped ZnO thin films had been dsposited. XPS core level spectra for Zn 2p, Fe 2p, Cl 2p and O 1s were performed. No Fe was observed in any of the samples (both surface and depth profiling). It has been previously reported that Fe can substitute at the Zn site in ZnO films, which can be in the form of either Fe^{2+} (Chen *et al.*, 2006; Saha *et al.*, 2012; Kafle *et al.*, 2016) or Fe^{3+} (Singh *et al.*, 2015; Ariyakkani *et al.*, 2017; Gorzkowska-Sobas *et al.*, 2010; Santhosh *et al.*, 2014) or mixed Fe^{2+}/Fe^{3+} (Yadav *et al.*, 2016; Rambu *et al.*, 2013). However, no Fe substitution was observed in these films deposited via AACVD. This could be a result of side reactions occurring in the solution, such as a ligand exchange, yielding iron acetate. Indeed, after some AACVD depositions, a red precipitate was observed in the bubbler which may be iron acetate as this is insoluble and has been described previously as a red solid if impure (Paul *et al.*, 1978; Laurikenas *et al.*, 2016). Furthermore, this would result in Zn^{2+} and Cl^{-} being present in higher concentrations in the precursor solution. However, other reactions are also possible, for example anhydrous $FeCl_3$ undergoes hydrolysis to produce HCl and iron hydroxide and the presence of HCl could result in Cl-doping.

Zn2p and O1s spectra of all films show similar features; therefore the Cl-doped ZnO films formed using 10 mol% $FeCl_3$ has been chosen as a representative example and is shown in Figure 5.4(a) and 5.4(b). The Zn $2p_{3/2}$ peak, observed at 1020.6 (±0.2) eV, was assigned to Zn^{2+}-O bond (Figure 5.4(a)) (Mar *et al.*, 1993; Deroubaix and Marcus, 1992). The O 1s spectrum (Figure 5.4(b)) can be deconvoluted into two peaks; the peak at 529.5 (±0.2) eV, corresponds to O^{2-} in the lattice and the peak at 531.4 (±0.2) eV can be attributed to oxygen vacancies or loosely bound oxygen species, such as adsorbed O_2 and -OH. This oxygen is related to chemisorption on the surface and at the grain boundaries of the polycrystalline films (Chen *et al.*, 2000; Park *et al.*, 2015; Islam *et al.*, 1996; Xue *et al.*, 2009). The Cl 2p XPS spectra of all the Cl-doped films are shown in Figure 5.4(c), indicating that Cl was introduced into the films. The Cl $2p_{3/2}$ peak at around 198.4 (±0.2) eV corresponds to Cl-Zn bond. All XPS values quoted correspond to those observed in the literature (Lee *et al.*, 2013; Choi *et al.*, 2015; Lee *et al.*, 2012).

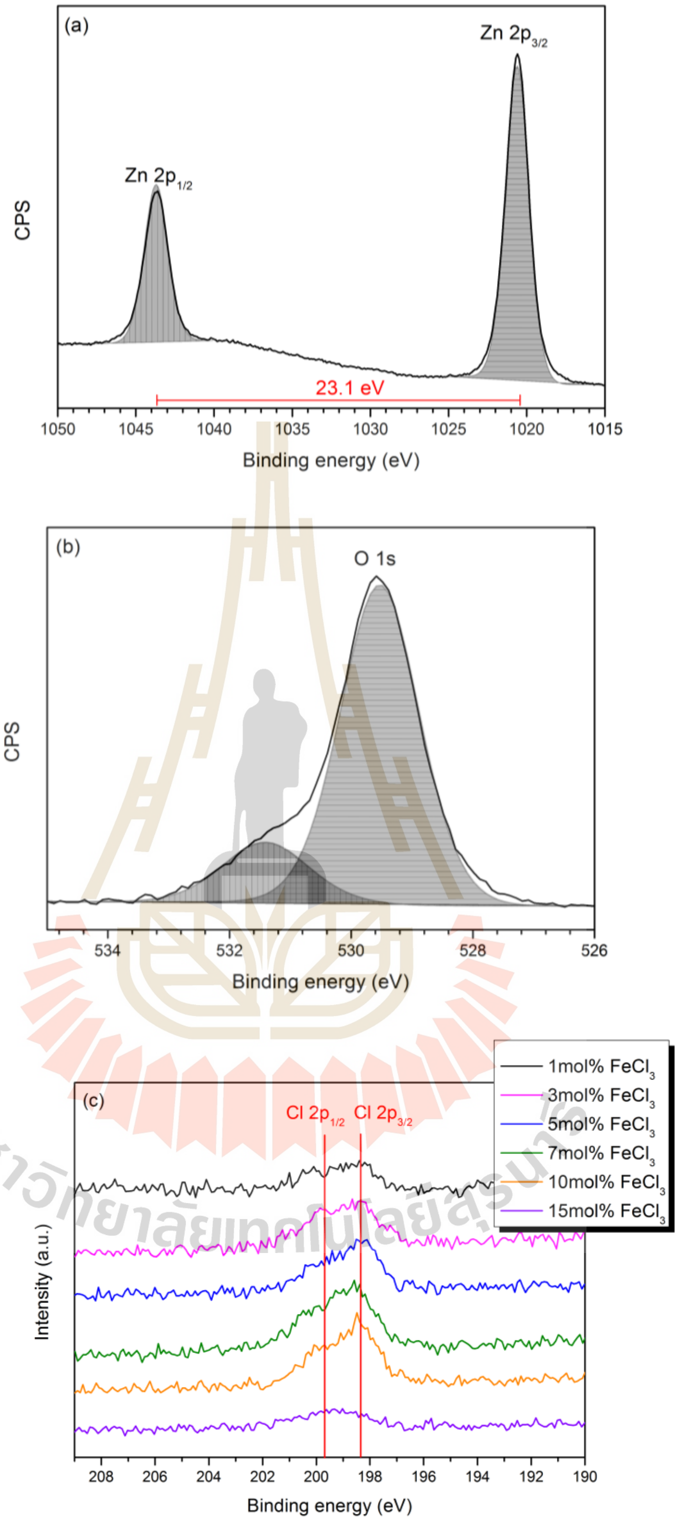

Figure 5.4 High-resolution XPS spectra of (a) Zn 2p$_{3/2}$ (b) O 1s of the Cl-doped ZnO film formed from 10mol% FeCl$_3$ and (c) Cl 2p for all films.

The calculated at.% of Cl in the bulk by depth profile was lower than that at the surface (see appendix). This suggests that the Cl concentration in the bulk was considerably lower due to preferential sputtering of Cl during the etching process, when Ar^+ ion bombardment was performed, as it is light element similar to F (Ponja *et al.*, 2014), O (Simpson *et al.*, 2017) and S (Baker *et al.*, 1999).

5.4.3 Crystal structure

XRD patterns of all films (Figure 5.5) can be indexed as the single phase of hexagonal Wurtzite ZnO (space group: $P6_3mc$). The preferred orientation illustrates itself through differences in peak intensity from sample to sample. This generally occurs during the film growth in order to minimise the internal stress and surface energy (Bao *et al.*, 1998). ZnO films have the preferred orientation of (002) plane along the *c*-axis which is normally observed in ZnO films as a result of film growth mechanism resulting in the most densely-packed and thermodynamically-favourable plane in the wurtzite structure (Ko Park and Lee, 2004). The preferred orientation changed to the (101) plane for the Cl-doped ZnO films formed using 1-5 mol% $FeCl_3$ and then back to the (002) on increasing the amount of $FeCl_3$ (7-15 mol%). It is worth noting that the (101) plane preferred orientation was observed in the case of Cl-doped ZnO films prepared by atomic layer deposition (Choi *et al.*, 2015) and Cl-doped ZnO nanospheres (Tao *et al.*, 2008) and microdisks (Yousefi and Jamali-Sheini, 2012) whereas the (002) plane was observed for Cl-doped ZnO nanodisks (Yousefi *et al.*, 2011) and nanowires (Fan *et al.*, 2011). This suggests that the preparation methods and form of sample influences the preferred orientation. Cell parameters *a*, *c* and cell volume (Figure 5.6), which were obtained from Le Bail refinement, increased from undoped to Cl-doped ZnO films. This is expected for incorporation of Cl into the ZnO structure, since a comparison of ionic radii indicates that O^{2-} (r_i = 1.40 Å) is substituted by the bigger anion Cl^- (r_i = 1.81 Å) (Shannon, 1976).

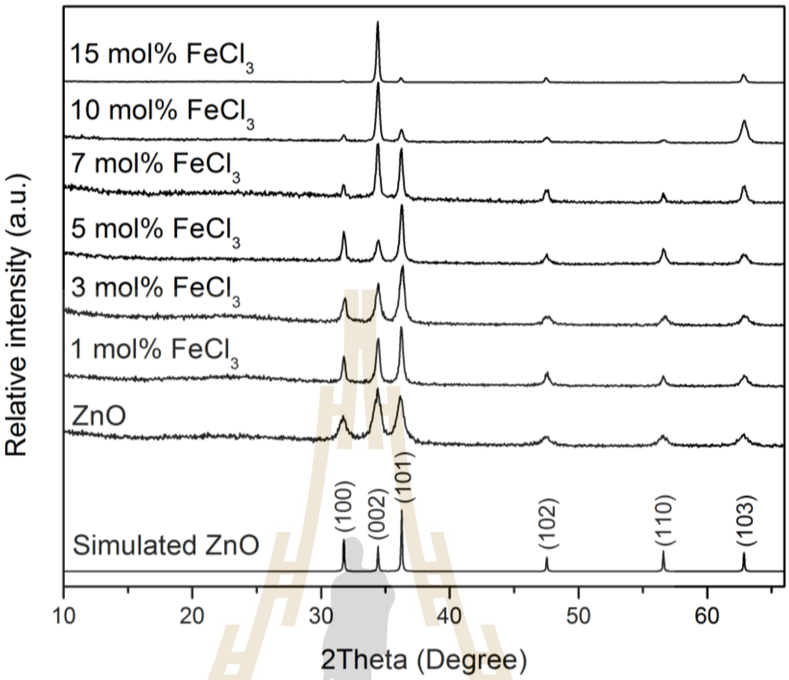

Figure 5.5 XRD patterns of simulated bulk ZnO (ICSD #82028), undoped and Cl-doped ZnO thin films.

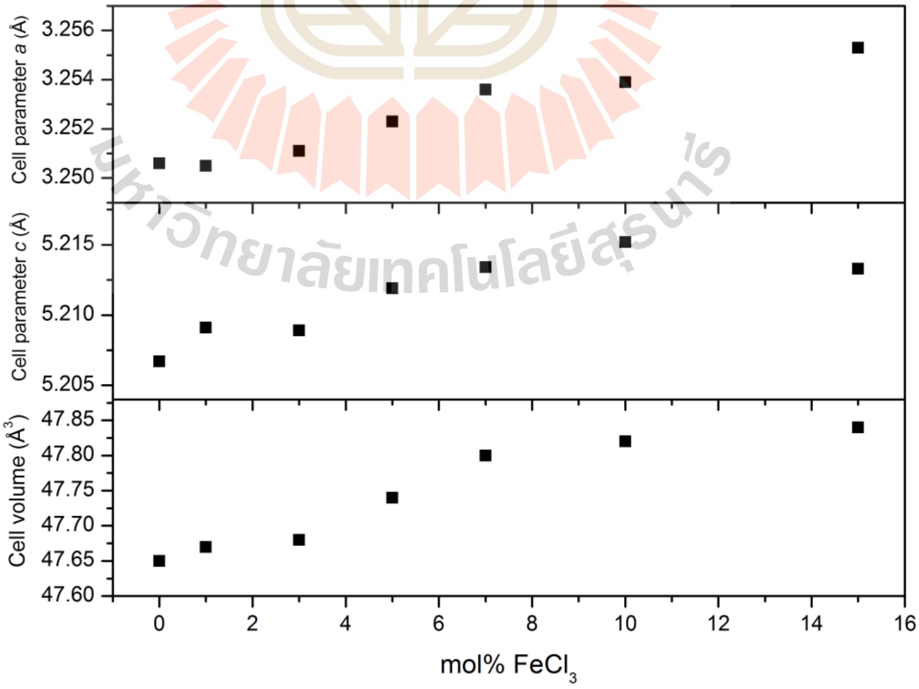

Figure 5.6 Variation of cell parameters *a*, *c* and cell volume of the films with a change of mol% $FeCl_3$ added to the precursor solution.

5.4.4 Surface morphology

SEM images (Figure 5.7) illustrate that the morphology of the ZnO films can be affected by Cl doping. This can be rationalised from the preferred orientation change, which can be seen from XRD patterns (Figure 5.5). The inclusion of Cl into the ZnO lattice had a significant effect on the surface morphology, such that even low levels of Cl in solution caused a change in the grain shape, as can be seen in the film formed using 5 mol% $FeCl_3$. It was also observed that the average grain size increased with the increase of mol% $FeCl_3$; this corresponds to the increase in crystallite size determined from Scherrer analysis (Table 5.1).

The morphology present in the samples was different to Cl-doped ZnO films prepared *via* ALD, which was expected due to the effect of the different deposition techniques (Choi *et al.*, 2015) However, the morphology changed to hexagonal for the film formed using 15 mol% $FeCl_3$, this was also observed in ZnO thin films formed with acetic acid added to the precursor solution (Chen *et al.*, 2015). Side-on SEM images (Figure 5.7, inset) were used to gain the thickness of the films, which are given in Table 5.1.

Table 5.1 Cell parameters *a*, *c*, cell volume *V*, crystallite size and film thickness.

mol%	*a* (Å)	*c* (Å)	*V* (Å^3)	Crystallite size (Å)	Thickness (nm)
0	3.2506(11)	5.2067(11)	47.65(3)	207.23±0.25	930
1	3.2505(7)	5.2091(12)	47.67(3)	297.07±0.50	470
3	3.2511(4)	5.2089(8)	47.68(1)	276.80±3.82	450
5	3.2523(2)	5.2119(5)	47.74(1)	328.83±2.94	460
7	3.2536(4)	5.2134(5)	47.80(1)	406.97±7.71	570
10	3.2539(4)	5.2152(4)	47.82(1)	377.27±1.31	580
15	3.2553(2)	5.2133(1)	47.84(1)	518.97±4.14	-

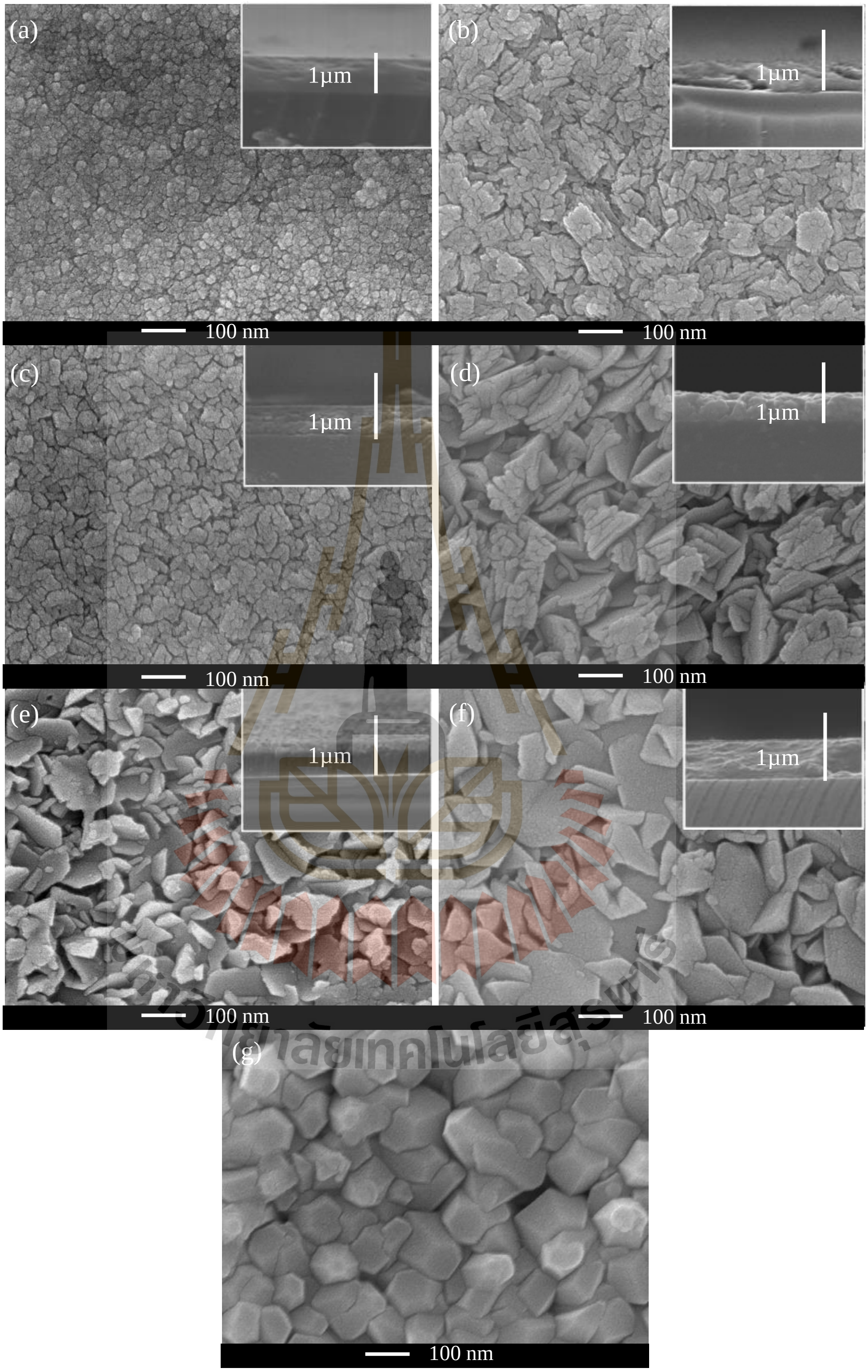

Figure 5.7 Top-down and side-on (inset) SEM images of ZnO and Cl-doped ZnO films with mol% $FeCl_3$ loading of (a) 0, (b) 1, (c) 3, (d) 5, (e) 7, (f) 10 and (g) 15.

5.4.5 Surface topology

AFM images (Figure 5.8) show the topology of the films and give information about the film roughness, which is reported as the root mean squared (rms) roughness value. The undoped ZnO film had a rms of 12.9±2.2 nm while the Cl-doped ZnO formed from 10 mol% $FeCl_3$ had a similar rms of 15.4±2.0 nm. Interestingly, the surface area difference of the undoped ZnO film and the Cl-doped ZnO formed from 10 mol% $FeCl_3$ were not significantly different.

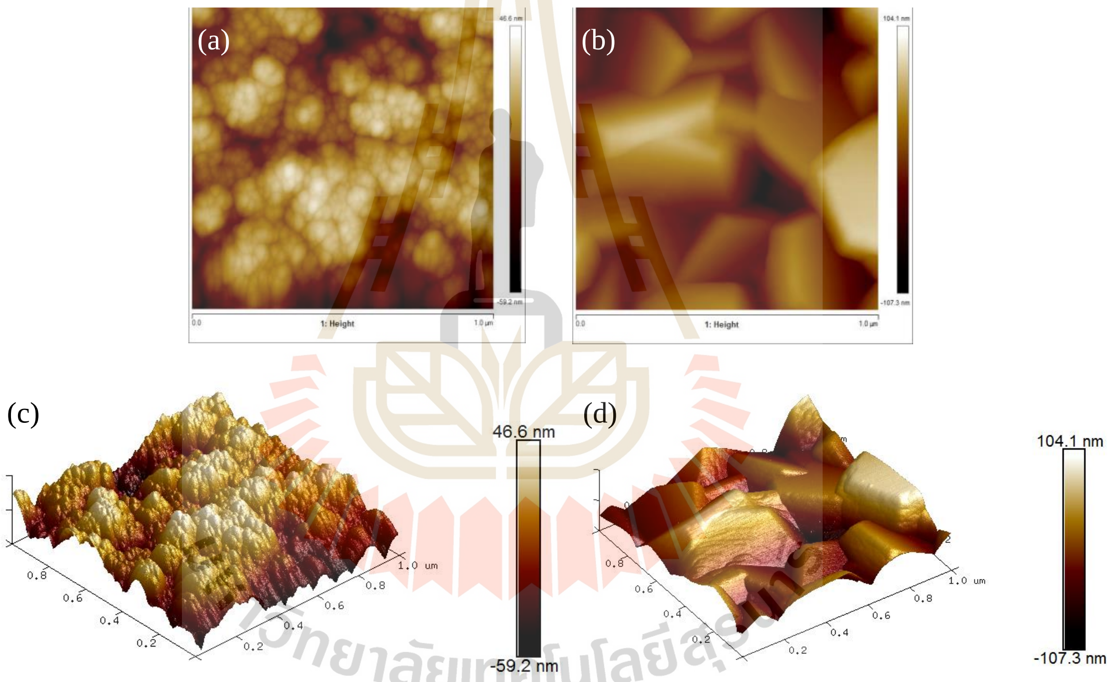

Figure 5.8 AFM images of (a) undoped ZnO, (b) 10 mol% $FeCl_3$ doped ZnO films as well as their 3D images of the same area (c) and (d).

5.4.6 Functional properties

5.4.6.1 Photocatalytic properties

The photocatalytic properties of the films were investigated during degradation of stearic acid under UVA irradiation. The photocatalytic reaction can be described as: $CH_3(CH_2)_{16}CO_2H + 26O_2 \xrightarrow{ZnO(h\nu \geq Eg)} 18CO_2 + 18H_2$ (1)

The results of the photocatalytic testing are conveniently expressed in terms of formal quantum efficiency (ξ), which indicates the number of stearic acid molecules degraded per incident photon. It can be seen in Figure 5.9 that the activity of the pure ZnO film was extremely poor whilst addition of small amounts of Cl precursor had a dramatic effect on photocatalytic performance. The best activities were recorded for the film deposited from 10 mol% $FeCl_3$ with the highest ξ of $3.0 \pm 0.1 \times 10^{-4}$ molecule/photon, which was about 18 times greater than that of undoped ZnO film.

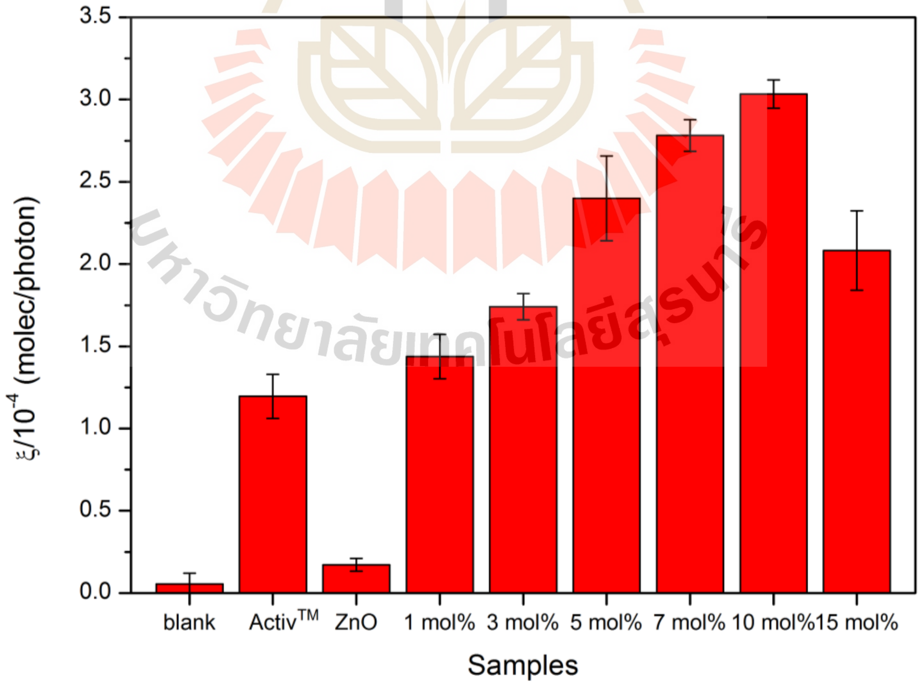

Figure 5.9 The formal quantum efficiency (FQE) for the degradation of stearic acid on undoped and Cl-doped ZnO films under UVA illumination. Pilkington *Activ* glass is used as reference.

The improved photocatalytic efficiencies of Cl-doped ZnO thin films compared with undoped ZnO thin films were likely due to changes in morphology, as shown in the SEM images (Figure 5.7). Morphology is reported to be one of the most important factors affecting photocatalytic activity (Pan *et al*., 2012). The changes in morphology come from the defect point in crystalline structure after Cl incorporation into the ZnO lattice, this allows us to believe that more reactive centres are produced and therefore causes the enhanced photocatalytic process (Wang *et al*., 2017). Moreover, crystal face exposure is also an important factor (Pung *et al*., 2012; Yu *et al*., 2013) since it was reported that the (101) plane showed higher photocatalytic activity than that of (001) in ZnO (Byzynski *et al*., 2017). This agrees with our work where (101) is the preferred orientation in some films. However, many factors need to be taken into consideration for the enhancement in photocatalytic efficiency, which cannot be concluded by a sole factor.

5.4.6.2 Transparent conducting oxide (TCO) properties

Optical properties

Figure 5.10 shows the transmittance spectrum of all the films. The glass used as the substrate showed a $\%T_{\lambda 400\text{-}700}$ of 89%. The undoped ZnO films displayed relatively low transmittance in the visible region, 68% (λ = 400-700 nm), as previously discussed this is attributed to carbon contamination. The Cl-doped ZnO films all displayed higher transparency; the films deposited using 5-10 mol% $FeCl_3$ have $\%T_{\lambda 400\text{-}700}$ greater than 80% with 7 mol% displaying the highest visible light transmission of 85%. This suggests that Cl-doping is an effective method to increase the optical transparency of ZnO thin films while electrical conductivity is preserved, this has also been described previously (Rousset *et al*., 2009; Lee *et al*., 2013; Chikoidze *et al*., 2008; Choi *et al*., 2015; Lee *et al*., 2012). It is interesting to note that attempts to use $ZnCl_2$ in place of $FeCl_3$ to form Cl-doped ZnO films resulted in the formation of grey films, hazy and poorly adhered films with very low Cl incorporation.

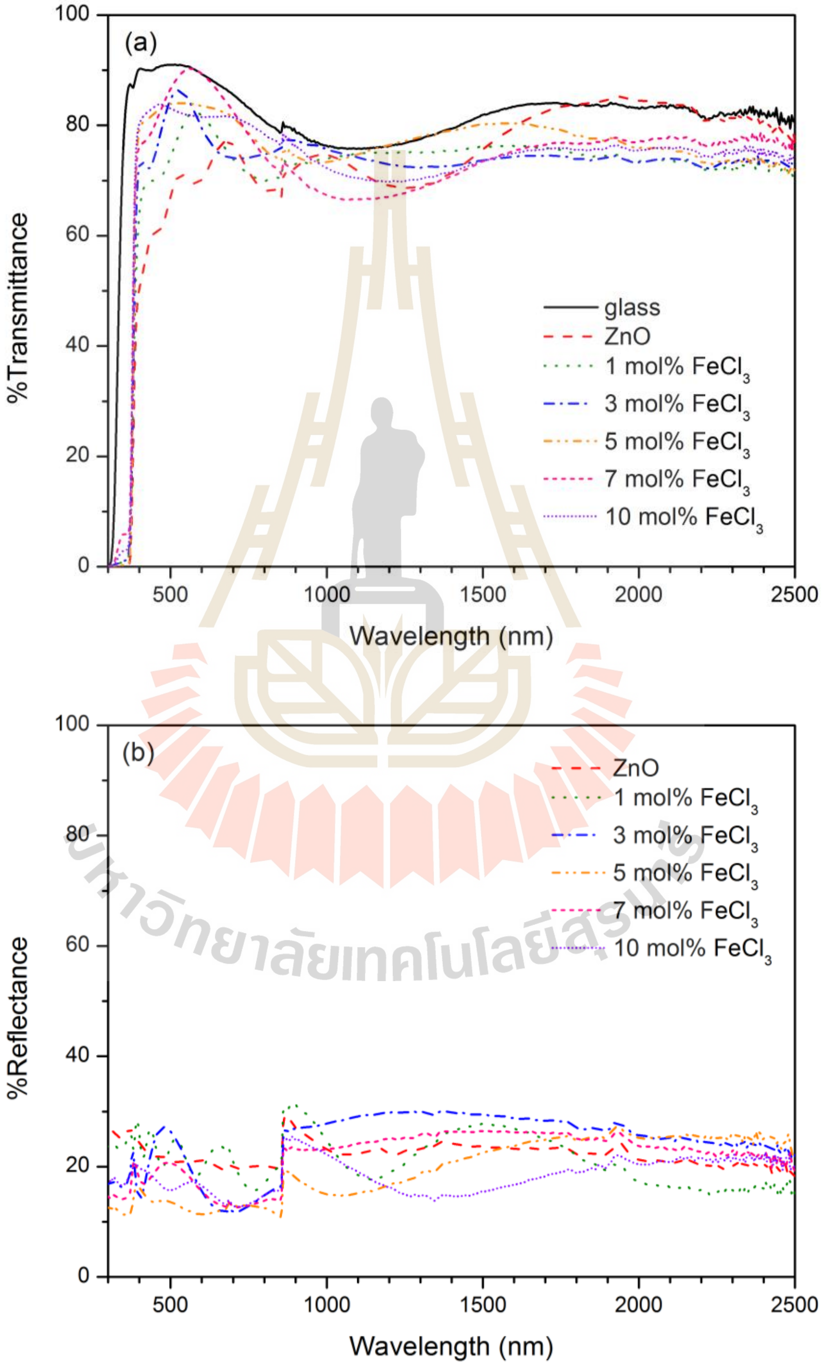

Figure 5.10 Transmittance (a) and reflectance spectra (b) of all films and the spectrum of bare glass was collected as reference.

To obtain the band gap energy, the optical properties of the films have been measured. The Tauc plot (Figure 5.11), which is the plot of $(\alpha h\nu)^2$ vs. $h\nu$ was utilised to estimate the band gap energy for ZnO. The absorption coefficient (α) was obtained from Lambert's equation: α = 1/t[2-log(%T)] where t and %T are the film thickness and %transmittance, respectively. The band gap energy of ZnO was 3.31±0.01 eV, which agrees with other works (Choi *et al*., 2015; Thomas, 1960; Hengehold *et al*., 1970; Liang and Yoffe, 1968; Gupta, 1990). In the case of Cl-doped ZnO films, which are degenerated semiconducting films, the band gap was estimated from the corrected Tauc plot to amend the underestimation when the Tauc method is used (Dixon *et al*., 2017). The band gap of Cl-doped ZnO films increases from that of undoped films (Table 5.2). Previously DFT calculations have shown for Cl-doped ZnO that the substitution of O by Cl introduces a shallow donor state derived mainly from Cl 3s states. The Fermi level shifts to the CB, resulting in an increase in optical band gap energy according to the Burstein-Moss effect (Slassi, 2015). However, the variation in Cl content does not significantly affect the band gap energy.

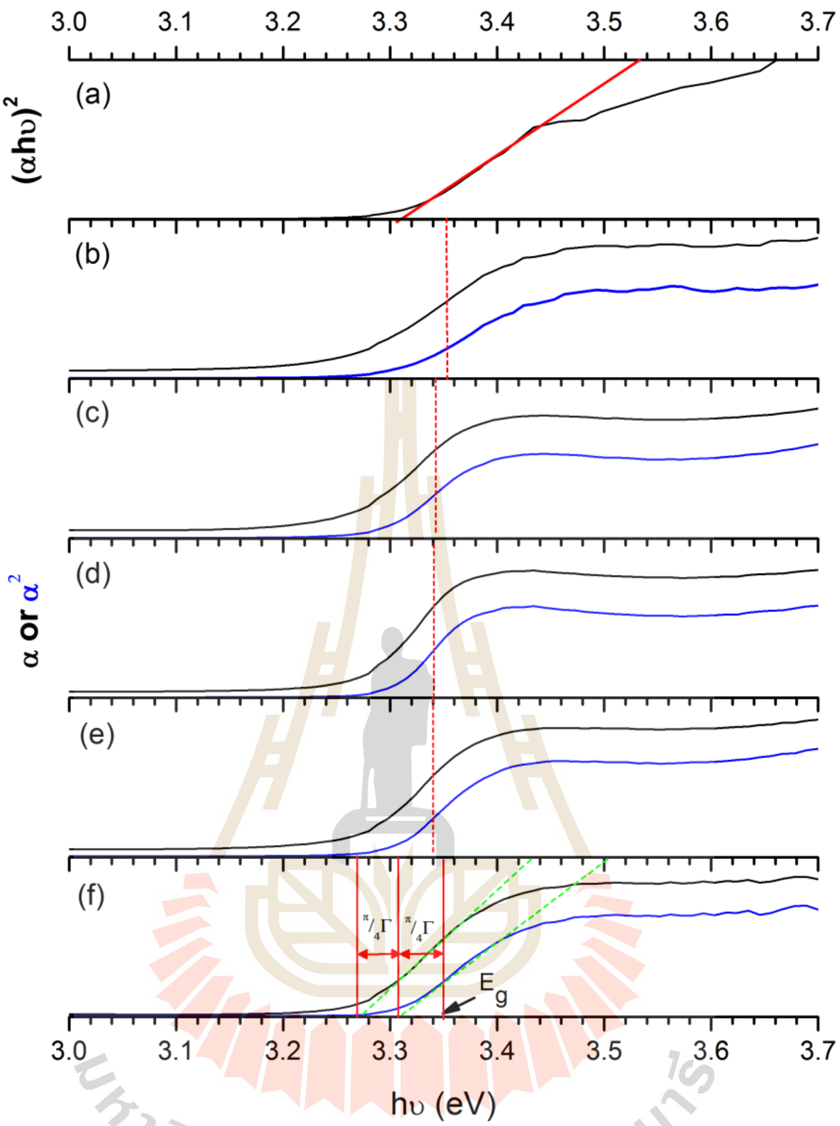

Figure 5.11 Tauc plots of ZnO films (a) and the corrected Tauc plot of ZnO:Cl films with 1 mol% (b), 3 mol% (c), 5 mol% (d), 7 mol% (e) and 10 mol% FeCl$_3$ (f). A broadening parameter $^{\pi}/_{4}\Gamma$ is obtained from the separation of extrapolations along the edge of α (black) and α^2 (blue) plots against $h\nu$, then the parameter is added to the uncorrected band gap to obtain a corrected estimate, as discussed by Dolgonos *et al*. (2016). The extrapolated lines on x-axis show band gap energy (E$_g$).

Electrical properties

Hall effect data was obtained for the samples, as shown in Table 5.2. The resistivity of the undoped ZnO films prepared in this work (1.4×10^{-1} Ω.cm) were similar to that reported previously (1.3×10^{-1} Ω.cm) for films deposited using Zn acetate dihydrate in methanol *via* AACVD (Dixon *et al*., 2017).

It can be seen that on substitution of Cl in ZnO films lower resistivity were obtained from that of undoped ZnO film, which can be rationalised from the donor electrons generated from Cl. As mentioned earlier, the DFT calculation shows that the substitution of O by Cl introduces a shallow donor state derived mainly from Cl 3s states. The Fermi level shifts to the CB, thus results in *n*-type semiconducting behavior (Slassi, 2015). This is also confirmed with negative value of carrier concentration. The film from 5 mol% $FeCl_3$ exhibited the lowest electrical resistivity of $4.28 \pm 0.41 \times 10^{-2}$ Ω.cm, the carrier concentration of $1.76 \pm 0.13 \times 10^{19}$ cm^{-3} and the carrier mobility of 8.66 ± 1.47 cm^{2} V^{-1} s^{-1}.

The Cl-doped ZnO films prepared in this work have electrical resistivity in the same order of magnitude comparing to those obtained using atomic layer deposition (0.55 at.% Cl-doped ZnO films: $\rho = 1.215 \times 10^{-2}$ Ω.cm, $n = 5.901 \times 10^{19}$ cm^{-3} and $\mu = 31.81$ cm^{2} V^{-1} s^{-1}) (Choi *et al*., 2015) and metal-organic CVD ($\rho = 3.6 \times 10^{-2}$ Ω.cm, $n \sim 10^{20}$ cm^{-3} and $\mu = 9\text{-}14$ cm^{2} V^{-1} s^{-1}) (Chikoidze *et al*., 2008; Chikoidze *et al*., 2008), but higher than that prepared by physical layer deposition (2.4 at.% Cl-doped ZnO films: $\rho = 6.344 \times 10^{-4}$ Ω.cm, $n = 4.04 \times 10^{20}$ cm^{-3} and $\mu = 23.75$ cm^{2} V^{-1} s^{-1}) (Lee *et al*., 2013; Lee *et al*., 2012). Computational studies have previously revealed that oxygen vacancy is the donor-type defect which show the lowest formation energy under *n*-type conditions; therefore it may also be valuable to take oxygen deficiency into an account for the conductivity in ZnO film prepared under as inert atmosphere like N_2 (Oba *et al*., 2001). It is also interesting to mention that the thermodynamic study using Kröger method proposed the possible defect impurities in Cl-doped ZnO, which are Zn vacancy (V_{Zn}), Zn interstitial (Z_i), oxygen vacancy (V_O) and chlorine donor (Cl_O) (Tchelidze *et al*., 2007). The defect in ZnO system is well known to be strongly correlated to preparation condition including temperature and atmosphere. This suggests that the film deposition route is an important factor affecting the electrical properties of synthesised films.

Table 5.2 Functional properties: photocatalytic properties and TCO properties, which includes electrical properties and optical properties.

mol% $FeCl_3$	Photocatalytic properties	TCO properties					
		Optical properties		Electrical properties			
	ξ (× 10^{-4} molec/photon)	%$T_{\lambda 400-700}$	E_g (eV)	n (× 10^{19} cm^{-3})	μ ($cm^2V^{-1}s^{-1}$)	ρ (× 10^{-2} Ω.cm)	R_{sh} (Ω□$^{-1}$)
0	0.17±0.04	68	3.31±0.01	0.10±0.01	4.34±0.12	1400.00±44.97	15053.8±483.6
1	1.44±0.14	76	3.35±0.01	0.86±0.11	6.35±0.84	11.91±0.01	2532.9±0.8
3	1.74±0.08	79	3.34±0.01	0.97±0.23	11.79±1.38	5.99±0.75	1331.9±167.4
5	2.40±0.26	83	3.34±0.01	1.76±0.13	8.66±1.47	4.28±0.41	929.8±89.46
7	2.78±0.10	85	3.34±0.01	1.11±0.30	9.90±1.04	6.41±1.13	1124.6±198.8
10	3.03±0.09	82	3.35±0.01	3.24±1.13	4.00±1.22	6.18±0.33	1064.8±57.2
15	2.08±0.24	-	-	-	-	-	-

n: charge carrier concentration; $\boldsymbol{\mu}$: charge carrier mobility; $\boldsymbol{\rho}$: bulk resistivity; $\boldsymbol{R_{sh}}$: sheet resistance; **ξ**: formal quantum yield efficiency.

These results show that deposition of electrically conductive and transparent Cl-doped ZnO films onto inexpensive glass substrates can be achieved via a one-step AACVD method without the requirement for post-deposition annealing or expensive vacuum apparatus. We have shown that the properties of the resulting Cl-doped ZnO thin films can be tailored to a specific application via altering the electronic, crystal and surface texture properties of the films. Thus, the Cl-doped ZnO films deposited *via* this simple AACVD route combine three functional properties (optical transparency, electrical conductivity and photocatalysis) within the same film making it a promising alternative to conventional TCO or photocatalytic materials. Furthermore, AACVD technique shows the potential to provide multifunctional properties by tuning some parameters, e.g., morphology, preferred orientation and surface roughness.

5.5 Conclusions

Cl-doped ZnO films have been successfully prepared via aerosol-assisted CVD for the first time from Zn acetate dihydrate and $FeCl_3$ in methanol. The substitution of Cl at O site into the ZnO lattice was confirmed by the obtained pure phase of wurtzite ZnO for all films and the increase in cell parameters *a*, *c* and cell volume, as well as the presence of Cl 1s XPS spectra. Fe was not found in the films, which might be due to side reactions of Fe compounds as some red precipitates were observed in the bubbler after deposition. The Cl-doping significantly affected the morphology of the synthesised thin films. TCO properties were achieved from Cl substitution as high transmittance above 80% and low electrical resistivity in the order of 10^{-2} Ω.cm were observed. The highest transmittance (%T) of 85% was obtained when using 7 mol% $FeCl_3$ in the precursor and the lowest resistivity of $4.28 \pm 0.41 \times 10^{-2}$ Ω.cm was obtained for 5 mol% $FeCl_3$. In contrast, the use of 10 mol% $FeCl_3$ doping resulted in Cl-doped ZnO thin films which exhibited the best photocatalytic activity of stearic acid degradation under UVA irradiation with the highest formal quantum efficiency (ξ) of $3.0 \pm 0.1 \times 10^{-4}$ molecule/photon. AFM images implied that the improvement in photocatalytic activity results from surface morphology and exposed crystal faces since the specific surface area of Cl-doped ZnO films from 10 mol% $FeCl_3$ were not significantly different from that of plain ZnO films. The surface morphology, optoelectronic properties and crystallinity have been shown to be dependent on the amount of $FeCl_3$ present in the precursor solution. These films showed potential application as both TCOs and photocatalysts; these multifunctional characteristics expand the scope of applications such as self-cleaning flat panel displays. Furthermore, the AACVD methodology could be utilised to tailor the functional properties of the films towards specific applications, such as for photocatalytic materials or TCOs for photovoltaic devices.

5.6 References

Ariyakkani, P., Suganya, L. and Sundaresan, B. (2017). Investigation of the structural, optical and magnetic properties of Fe doped ZnO thin films coated on glass by sol-gel spin coating method. **Journal of Alloys and Compounds**. 695: 3467–3475.

Baker, M. A., Gilmore, R., Lenardi, C. and Gissler, W. (1999). XPS investigation of preferential sputtering of S from MoS_2 and determination of MoS_x stoichiometry from Mo and S peak positions. **Applied Surface Science**. 150: 255–262.

Bao, D., Gu, H. and Kuang, A. (1998). Sol-gel-derived c-axis oriented Z, qO thin films. **Thin Solid Films**. 312: 37–39.

Bhachu, D. S., Sathasivam, S., Sankar, G., Scanlon, D. O., Cibin, G., Carmalt, C. J., Parkin, I. P., Watson, G. W., Bawaked, S. M., Obaid, A. Y., Al-Thabaiti, S. and Basahel, S. N. (2014). Solution processing route to multifunctional titania thin films: Highly conductive and photcatalytically active Nb:TiO_2. **Advanced Functional Materials**. 24: 5075–5085.

Bhachu, D. S., Waugh, M. R., Zeissler, K., Branford, W. R. and Parkin, I. P. (2011). Textured fluorine-doped tin dioxide films formed by chemical vapour deposition. **Chemistry - A European Journal**. 17: 11613–11621.

Byzynski, G., Melo, C., Volanti, D. P., Ferrer, M. M., Gouveia, A. F., Ribeiro, C., Andrés, J. and Longo, E. (2017). The interplay between morphology and photocatalytic activity in ZnO and N-doped ZnO crystals. **Materials and Design**. 120: 363–375.

Chen, A. J., Wu, X. M., Sha, Z. D., Zhuge, L. J. and Meng, Y. D. (2006). Structure and photoluminescence properties of Fe-doped ZnO thin films. **Journal of Physics D: Applied Physics**. 39: 4762–4765.

Chen, M., Wang, X., Yu, Y. H., Pei, Z. L., Bai, X. D., Sun, C., Huang, R. F. and Wen, L. S. (2000). X-ray photoelectron spectroscopy and auger electron spectroscopy studies of Al-doped ZnO films. **Applied Surface Science**. 158: 134–140.

Chen, S., Wilson, R. M. and Binions, R. (2015). Synthesis of highly surface-textured ZnO thin films by aerosol assisted chemical vapour deposition. **Journal of Material Chemistry A**. 3: 5794–5797.

Chikoidze, E., Modreanu, M., Sallet, V., Gorochov, O. and Galtier, P. (2008). Electrical properties of chlorine-doped ZnO thin films grown by MOCVD. **Physica Status Solidi A-applications and Materials Science**. 205: 1575–1579.

Chikoidze, E., Nolan, M., Modreanu, M., Sallet, V. and Galtier, P. (2008). Effect of chlorine doping on electrical and optical properties of ZnO thin films. **Thin Solid Films**. 516: 8146–8149.

Choi, Y. -J., Kang, K. -M., Lee, H. -S. and Park, H. -H. (2015). Non-laminated growth of chlorine-doped zinc oxide films by atomic layer deposition at low temperatures. **Journal of Materials Chemistry C**. 3: 8336–8343.

Deroubaix, G. and Marcus, P. (1992). X-ray photoelectron spectroscopy analysis of copper and zinc oxides and sulphides. **Surface and Interface Analysis**. 18: 39–46.

Dixon, S. C., Sathasivam, S., Williamson, B. A. D., Scanlon, D. O., Carmalt, C. J. and Parkin, I. P. (2017). Transparent conducting n-type ZnO:Sc – synthesis, optoelectronic properties and theoretical insight. **Journal of Material Chemistry C**. 5: 7585–7597.

Dixon, S. C., Scanlon, D. O., Carmalt, C. J. and Parkin, I. P. (2016). n-Type doped transparent conducting binary oxides: an overview. **Journal of Material Chemistry C**. 4: 6946–6961.

Dolgonos, A., Mason, T. O. and Poeppelmeier, K. R. (2016). Direct optical band gap measurement in polycrystalline semiconductors: A critical look at the Tauc method. **Journal of Solid State Chemistry**. 240: 43–48.

Fan, J., Shavel, A., Zamani, R., Fábrega, C., Rousset, J., Haller, S., Güell, F., Carrete, A., Andreu, T., Arbiol, J., Morante, J. R. and Cabot, A. (2011). Control of the doping concentration, morphology and optoelectronic properties of vertically aligned chlorine-doped ZnO nanowires. **Acta Materialia**. 59: 6790–6800.

Ghandhi, S. K., Field, R. J. and Shealy, J. R. (1980). Highly oriented zinc oxide films grown by the oxidation of diethylzinc. **Applied Physics Letters**. 37: 449–451.

Ginley, D. S. and Perkins, J. D. (2011). Transparent Conductors. In **Handbook of transparent conductors**.

Gordon, R. G. (2000). Criteria for Choosing Transparent Conductors. **MRS Bulletin**. 25: 52–57.

Gorzkowska-Sobas, A., Galeckas, A., Sunding, M. F., Diplas, S. and Kuznetsov, A. Y. (2010). An investigation of Fe-doped ZnO thin films grown by magnetron sputtering. **Physica Scripta**. T141: 14004.

Granqvist, C. G. and Hultåker, A. (2002). Transparent and conducting ITO films: new developments and applications. **Thin Solid Films**. 411: 1–5.

Gupta, T. K. (1990). Application of Zinc Oxide Varistors. **Journal of the American Ceramic Society**. 73: 1817–1840.

Hengehold, R. L., Almassy, R. J. and Pedrotti, F. L. (1970). Electron energy-loss and ultraviolet-reflectivity spectra of crystalline ZnO. **Physical Review B**. 1: 4784–4791.

Hollingsworth, N., Johnson, A. L., Kingsley, A., Kociok-Köhn, G. and Molloy, K. C. (2010). Structural study of the reaction of methylzinc amino alcoholates with oxygen. **Organometallics**. 29: 3318–3326.

Howard, D. P., Marchand, P., Carmalt, C. J., Parkin, I. P. and Darr, J. A. (2017). Si-doped zinc oxide transparent conducting oxides; nanoparticle optimisation, scale-up and thin film deposition. **Journal of Material Chemistry C**. 5: 8796–8801.

Howard, D. P., Marchand, P., Johnson, I. D., Carmalt, C. J., Parkin, I. P. and Darr, J. A. (2016). Conducting Al and Ga-doped zinc oxides; rapid optimisation and scale-up. **Journal of Material Chemistry A**. 4: 12774–12780.

Howard, D. P., Marchand, P., McCafferty, L., Carmalt, C. J., Parkin, I. P. and Darr, J. A. (2017). High-Throughput Continuous Hydrothermal Synthesis of Transparent Conducting Aluminum and Gallium Co-doped Zinc Oxides. **ACS Combinatorial Science**. 19: 239–245.

Hu, J. and Gordon, R. G. (1991). Textured fluorine-doped ZnO films by atmospheric pressure chemical vapor deposition and their use in amorphous silicon solar cells. **Solar Cells**. 30: 437–450.

Hu, J. and Gordon, R. G. (1992). Textured aluminum-doped zinc oxide thin films from atmospheric pressure chemical-vapor deposition. **Journal of Applied Physics**. 71:

880–890.

Islam, M. N., Ghosh, T. B., Chopra, K. L. and Acharya, H. N. (1996). XPS and X-ray diffraction studies of aluminum-doped zinc oxide transparent conducting films. **Thin Solid Films**. 280: 20–25.

Kafizas, A., Noor, N., Carmichael, P., Scanlon, D. O., Carmalt, C. J. and Parkin, I. P. (2014). Combinatorial atmospheric pressure chemical vapor deposition of F:TiO_2; The relationship between photocatalysis and transparent conducting oxide properties. **Advanced Functional Materials**. 24: 1758–1771.

Kafle, B. P., Acharya, S., Thapa, S. and Poudel, S. (2016). Structural and optical properties of Fe-doped ZnO transparent thin films. **Ceramics International**. 42: 1133–1139.

Ko Park, S. -H. and Lee, Y. E. (2004). Controlling preferred orientation of ZnO thin films by atomic layer deposition. **Journal of Materials Science**. 39: 2195–2197.

Kuprenaite, S., Murauskas, T., Abrutis, A., Kubilius, V., Saltyte, Z. and Plausinaitiene, V. (2015). Properties of In-, Ga-, and Al-doped ZnO films grown by aerosol-assisted MOCVD: Influence of deposition temperature, doping level and annealing. **Surface and Coatings Technology**. 271: 156–164.

Larson, A. C. and Von Dreele, R. B. (2004). General Structure Analysis System (GSAS). **Structure**. 748: 86–748.

Laurikenas, A., Barkauskas, J., Reklaitis, J., Niaura, G., Baltrunas, D. and Kareiva, A. (2016). Formation Peculiarities of Iron (III) Acetate: Potential Precursor for Iron Metal-Organic Frameworks (MOFs). **Lithuanian Journal of Physics**. 56: 35–41.

Lee, J., Park, E., Subramaniam, N. G., Lee, J., Lee, J., Lee, J. and Kang, T. (2012). Non-metallic element (chlorine) doped Zinc oxide grown by pulsed laser deposition for application in transparent electrode. **Current Applied Physics**. 12: S80–S84.

Lee, J. C., Subramaniam, N. G., Lee, J. W., Lee, J. C. and Kang, T. W. (2013). Evaluation of optimal chlorine doping concentration in zinc oxide on glass for application as new transparent conductive oxide. **Physica Status Solidi (A) Applications and Materials Science**. 210: 2638–2643.

Liang, W. Y. and Yoffe, A. D. (1968). Transmission spectra of ZnO single crystals. **Physical Review Letters**. 20: 59–62.

Lin, C. -C., Chiang, M. -C. and Chen, Y. -W. (2009). Temperature dependence of Fluorine-doped tin oxide films produced by ultrasonic spray pyrolysis. **Thin Solid Films**. 518: 1241–1244.

Manzi, J. A., Knapp, C. E., Parkin, I. P. and Carmalt, C. J. (2016). Aerosol assisted chemical vapour deposition of transparent conductive aluminum-doped zinc oxide thin films from a zinc triflate precursor. **Thin Solid Films**. 616: 477–481.

Mar, L. G., Timbrell, P. Y. and Lamb, R. N. (1993). An XPS Study of Zinc-Oxide Thin-Film Growth on Copper Using Zinc Acetate as a Precursor. **Thin Solid Films**. 223: 341–347.

Marchand, P., Hassan, I. A., Parkin, I. P. and Carmalt, C. J. (2013). Aerosol-assisted delivery of precursors for chemical vapour deposition: expanding the scope of CVD for materials fabrication. **Dalton Transactions**. 42: 9406.

McNally, C. S., Turner, D. P., Kulak, A. N., Meldrum, F. C. and Hyett, G. (2012). The use of cationic surfactants to control the structure of zinc oxide films prepared by chemical vapour deposition. **Chemical communications (Cambridge, England)**. 48: 1490-1492.

Mills, A. and Wang, J. (2006). Simultaneous monitoring of the destruction of stearic acid and generation of carbon dioxide by self-cleaning semiconductor photocatalytic films. **Journal of Photochemistry and Photobiology A:**

Chemistry. 182: 181–186.

Mohri, S., Hirose, Y., Nakao, S., Yamada, N., Shimada, T. and Hasegawa, T. (2012). Transparent conductivity of fluorine-doped anatase TiO_2 epitaxial thin films. **Journal of Applied Physics**. 111: 93528.

Oba, F., Nishitani, S. R., Isotani, S., Adachi, H. and Tanaka, I. (2001). Energetics of native defects in ZnO. **Journal of Applied Physics**. 90: 824–828.

Pan, L., Zou, J. -J., Wang, S., Liu, X. -Y., Zhang, X. and Wang, L. (2012). Morphology Evolution of TiO_2 Facets and Vital Influences on Photocatalytic Activity. **ACS Applied Materials and Interfaces**. 4: 1650–1655.

Park, J. -W., So, H. S., Lee, H. -M., Kim, H. -J., Kim, H. -K. and Lee, H. (2015). Transition from a nanocrystalline phase to an amorphous phase in In-Si-O thin films: The correlation between the microstructure and the optical properties. **Journal of Applied Physics**. 117: 155305.

Paul, R. C., Narula, R. C. and Vasisht, S. K. (1978). Iron(III) acetates. **Transition Metal Chemistry**. 3: 35–38.

Ponja, S. D., Sathasivam, S., Parkin, I. P. and Carmalt, C. J. (2014). Transparent conductive aluminium and fluorine co-doped zinc oxide films via aerosol assisted chemical vapour deposition. **RSC Advances.** 4: 49723–49728.

Potter, D. B., Bhachu, D. S., Powell, M. J., Darr, J. A., Parkin, I. P. and Carmalt, C. J. (2016). Al-, Ga-, and In-doped ZnO thin films via aerosol assisted CVD for use as transparent conducting oxides. **Physica Status Solidi (A) Applications and Materials Science**. 213: 1346–1352.

Potter, D. B., Powell, M. J., Darr, J. A., Parkin, I. P. and Carmalt, C. J. (2017). Transparent conducting oxide thin films of Si-doped ZnO prepared by aerosol assisted CVD. **RSC Advances.** 7: 10806–10814.

Potter, D. B., Powell, M. J., Parkin, I. P. and Carmalt, C. J. (2018). Aluminium/gallium, indium/gallium, and aluminium/indium co-doped ZnO thin films deposited *via* aerosol assisted CVD. **Journal of Materials Chemistry C**. 6: 588–597.

Powell, M. J. and Carmalt, C. J. (2017). Aerosols: A Sustainable Route to Functional Materials. **Chemistry - A European Journal**. 23: 15543–15552.

Pung, S. -Y., Lee, W. -P. and Aziz, A. (2012). Kinetic Study of Organic Dye Degradation Using ZnO Particles with Different Morphologies as a Photocatalyst. **International Journal of Inorganic Chemistry**. 2012: 1–9.

Rambu, A. P., Nica, V. and Dobromir, M. (2013). Influence of Fe-doping on the optical and electrical properties of ZnO films. **Superlattices and Microstructures**. 59: 87–96.

Rousset, J., Saucedo, E., Herz, K. and Lincot, D. (2011). High efficiency CIGS-based solar cells with electrodeposited ZnO: Cl as transparent conducting oxide front contact. **Progress in Photovoltaics: Research and Applications**. 19: 537–546.

Rousset, J., Saucedo, E. and Lincot, D. (2009). Extrinsic Doping of Electrodeposited Zinc Oxide Films by Chlorine for Transparent Conductive Oxide Applications Extrinsic Doping of Electrodeposited Zinc Oxide Films by Chlorine for Transparent Conductive Oxide Applications. **Chemistry of Materials**. 21: 534–540.

Saha, S., Tomar, M. and Gupta, V. (2012). Fe doped ZnO thin film for mediator-less biosensing application. **Journal of Applied Physics**. 111: 102804.

Santhosh, V. S., Rajendra Babu, K. and Deepa, M. (2014). Influence of Fe dopant concentration and annealing temperature on the structural and optical properties of ZnO thin films deposited by sol–gel method. **Journal of Materials Science: Materials in Electronics**. 25: 224–232.

Sathasivam, S., Bhachu, D. S., Lu, Y., Chadwick, N., Althabaiti, S. A., Alyoubi, A. O., Basahel, S. N., Carmalt, C. J. and Parkin, I. P. (2015). Tungsten Doped TiO_2 with Enhanced Photocatalytic and Optoelectrical Properties via Aerosol Assisted Chemical Vapor Deposition. **Scientific Reports**. 5: 10952.

Shannon, R. D. (1976). Revised effective ionic radii and systematic studies of interatomic distances in halides and chalcogenides. **Acta Crystallographica Section A**. 32: 751–767.

Simpson, R., White, R. G., Watts, J. F. and Baker, M. A. (2017). XPS investigation of monatomic and cluster argon ion sputtering of tantalum pentoxide. **Applied Surface Science**. 405: 79–87.

Singh, K., Devi, V., Dhar, R. and Mohan, D. (2015). Structural, optical and electronic properties of Fe doped ZnO thin films. **Superlattices and Microstructures**. 85: 433–437.

Slassi, A. (2015). First-principles and Boltzmann equation studies of the Cl-doped ZnO transparent conducting oxide. **Optik**. 126: 4751–4756.

Sotelo-Vazquez, C., Noor, N., Kafizas, A., Quesada-Cabrera, R., Scanlon, D. O., Taylor, A., Durrant, J. R. and Parkin, I. P. (2015). Multifunctional P-doped TiO_2 Films: A new approach to self-cleaning, transparent conducting oxide materials. **Chemistry of Materials**. 27: 3234–3242.

Tao, Z., Yu, X., Fei, X., Liu, J., Yang, G., Zhao, Y., Yang, S. and Yang, L. (2008). Synthesis and photoluminescence of Cl-doped ZnO nanospheres. **Optical Materials**. 31: 1–5.

Tchelidze, T., Chikoidze, E., Gorochov, O. and Galtier, P. (2007). Perspectives of chlorine doping of ZnO. **Thin Solid Films**. 515: 8744–8747.

Thomas, D. G. (1960). The exciton spectrum of zinc oxide. **Journal of Physics and Chemistry of Solids**. 15: 86–96.

Toby, B. H. (2001). EXPGUI, a graphical user interface for GSAS. **Journal of Applied Crystallography**. 34: 210–213.

U.S. Department of the Interior and U.S. Geological Survey. (2017). *Mineral commodity summaries 2017: U.S. Geological Survey*. **Mineral Commodity Summaries 2017**. (Vol. 1).

Walters, G. and Parkin, I. P. (2009). Aerosol assisted chemical vapour deposition of ZnO films on glass with noble metal and p-type dopants; use of dopants to influence preferred orientation. **Applied Surface Science**. 255: 6555–6560.

Wang, W., Ai, T. and Yu, Q. (2017). Electrical and photocatalytic properties of boron-doped ZnO nanostructure grown on PET–ITO flexible substrates by hydrothermal method. **Scientific Reports**. 7: 42615.

Waugh, M. R., Hyett, G. and Parkin, I. P. (2008). Zinc oxide thin films grown by aerosol assisted CVD. **Chemical Vapor Deposition**. 14: 369–372.

Xu, H. Y., Liu, Y. C., Mu, R., Shao, C. L., Lu, Y. M., Shen, D. Z. and Fan, X. W. (2005). F-doping effects on electrical and optical properties of ZnO nanocrystalline films. **Applied Physics Letters**. 86: 1–3.

Xue, H., Chen, Y., Xu, X. L., Zhang, G. H., Zhang, H. and Ma, S. Y. (2009). X-ray diffraction spectroscopy and X-ray photoelectron spectroscopy studies of Cu-doped ZnO films. **Physica E: Low-dimensional Systems and Nanostructures**. 41: 788–791.

Yadav, A. K., Haque, S. M., Tripathi, S., Shukla, D., Ahmed, M. A., Phase, D. M., Bandyopadhyay, S., Jha, S. N. and Bhattacharyya, D. (2016). Investigation of Fe doped ZnO thin films by X-ray absorption spectroscopy. **RSC Advances**. 6: 74982–74990.

Yan, X. -T. and Xu, Y. (2010). Chemical Vapour Deposition. In **An Integrated**

Engineering Design for Advanced Materials.

Yang, X., Wolcott, A., Wang, G., Sobo, A., Fitzmorris, R. C., Qian, F., Zhang, J. Z. and Li, Y. (2009). Nitrogen-doped ZnO nanowire arrays for photoelectrochemical water splitting. **Nano Letters**. 9: 2331–2336.

Yates, H. M., Gaskell, J. M., Thomson, M. E., Sheel, D. W., Delaup, B. and Morales-Masis, M. (2015). APCVD of dual layer transparent conductive oxides for photovoltaic applications. **Thin Solid Films**. 590: 260–265.

Yousefi, R. and Jamali-Sheini, F. (2012). Effect of chlorine ion concentration on morphology and optical properties of Cl-doped ZnO nanostructures. **Ceramics International**. 38: 5821–5825.

Yousefi, R., Zak, A. K. and Mahmoudian, M. R. (2011). Growth and characterization of Cl-doped ZnO hexagonal nanodisks. **Journal of Solid State Chemistry**. 184: 2678–2682.

Yu, C., Cao, F., Li, X., Li, G., Xie, Y., Yu, J. C., Shu, Q., Fan, Q. and Chen, J. (2013). Hydrothermal synthesis and characterization of novel $PbWO_4$ microspheres with hierarchical nanostructures and enhanced photocatalytic performance in dye degradation. **Chemical Engineering Journal**. 219: 86–95.

CHAPTER VI

CONCLUSIONS

In this thesis, many oxides have been synthesised and investigated in an attempt to produce transparent conducting oxides

As Sn-doped In_2O_3 (ITO) is the most widely used TCOs, the investigation started with indium-based oxide. In_2TeO_6 was an interesting choice because the theoretical study derived from DFT calculation suggested that it can be a good n-type TCO considering its low effective mass, which results in high carrier mobility. In addition, some doped In_2TeO_6 have been reported to show semiconducting behaviour. Combined with the relatively large band gap (~3 eV), it might be possible to design TCOs based on In_2TeO_6. Although attempt to doped In_2TeO_6 with heterovalent Bi^{5+} was not successful, investigation on Bi^{3+}, Ga^{3+} and La^{3+} substituted In_2TeO_6 has led to interesting information on both electronic and optical properties of the compounds. These homovalent substitutions do not create any extra charge carriers but they do affect the structure and optical properties. The systematic study of their crystal structures, optical properties and band structure calculation is present. This study reports, for the first time, that In_2TeO_6 has direct band gap transition.

$In_4Sn_3O_{12}$ was then chosen for further study because it has less indium composition compared to the famous ITO but still has good electrical conductivity. Some reports on this compound show its potential to be good TCOs; however, doping on this compound has not been extensively investigated. Thus, M-doped $In_4Sn_3O_{12}$ (M = Nb and Ta) is investigated. Although the electrical properties of the doped samples are not improved, the detail investigation has deepened the understanding of electrical and other relevant properties such as optical properties. Importantly, the origin of conductivity in $In_4Sn_3O_{12}$ and related compounds is proposed. Based on both experimental and theoretical results, it is concluded that the high conductivity in $In_4Sn_3O_{12}$ originates from the presence of oxygen vacancies.

The exploration then moved to ZnO based oxides. ZnO is a promising candidate for TCOs because it is well known as an intrinsic *n*-type semiconductor with a wide band gap (~3.37 eV). Furthermore, it has high thermal stability, is inexpensive, earth abundant and relatively nontoxic compared to ITO and F-doped SnO_2 (FTO). Anion doping is considered to be a superior route to obtain high carrier concentration and mobility while maintaining high transparency. Cl doping for ZnO was studied because it shows the potential on some properties such as electrical properties but has not been comprehensively studied. Aerosol-assisted chemical vapour deposition was used to fabricate Cl-doped ZnO thin film. The obtained films exhibited TCO properties with good electrical and optical properties. Additionally, they showed self-cleaning properties, which were determined by photocatalytic degradation of stearic acid under UVA (365 nm) irradiation. Interestingly, Cl-doped ZnO thin films with multifunctional properties are promising materials to expand the scope for sustainable applications.

APPENDICES

APPENDIX A

XPS ANALYSIS OF Cl-DOPED ZnO FILMS

A1 XPS Depth profile and calculation of at.% Cl in films

To obtain the at.% Cl, the fitting analysis of Cl $2p_{3/2}$ and Zn $2p_{3/2}$ were performed and the obtained peak areas of both peaks were used for the calculation as:

$$\text{at.\% Cl} = \left[\frac{\text{corrected area of Cl } 2p_{3/2}}{(\text{corrected area of Cl } 2p_{3/2} + \text{corrected area of Zn } 2p_{3/2})}\right] x\ 100$$

where corrected peak area = peak area × R.S.F. (relative sensitivity factor).

Table A1 shows the at.% Cl both at surface and in the bulk from depth profile XPS (500-2500 s). Note that the signal to noise ratio in the film with 1 mol% $FeCl_3$ added is weak which are not allowed to make a proper fitting. Figure A1 shows the Cl 2p XPS spectra of all films from the surface and depth profiling. The absence of Fe was detected in doped samples at both surface and depth profiling. Figure A2 is shown as a representative for Fe 2p XPS spectra of the film prepared using 10 mol% $FeCl_3$.

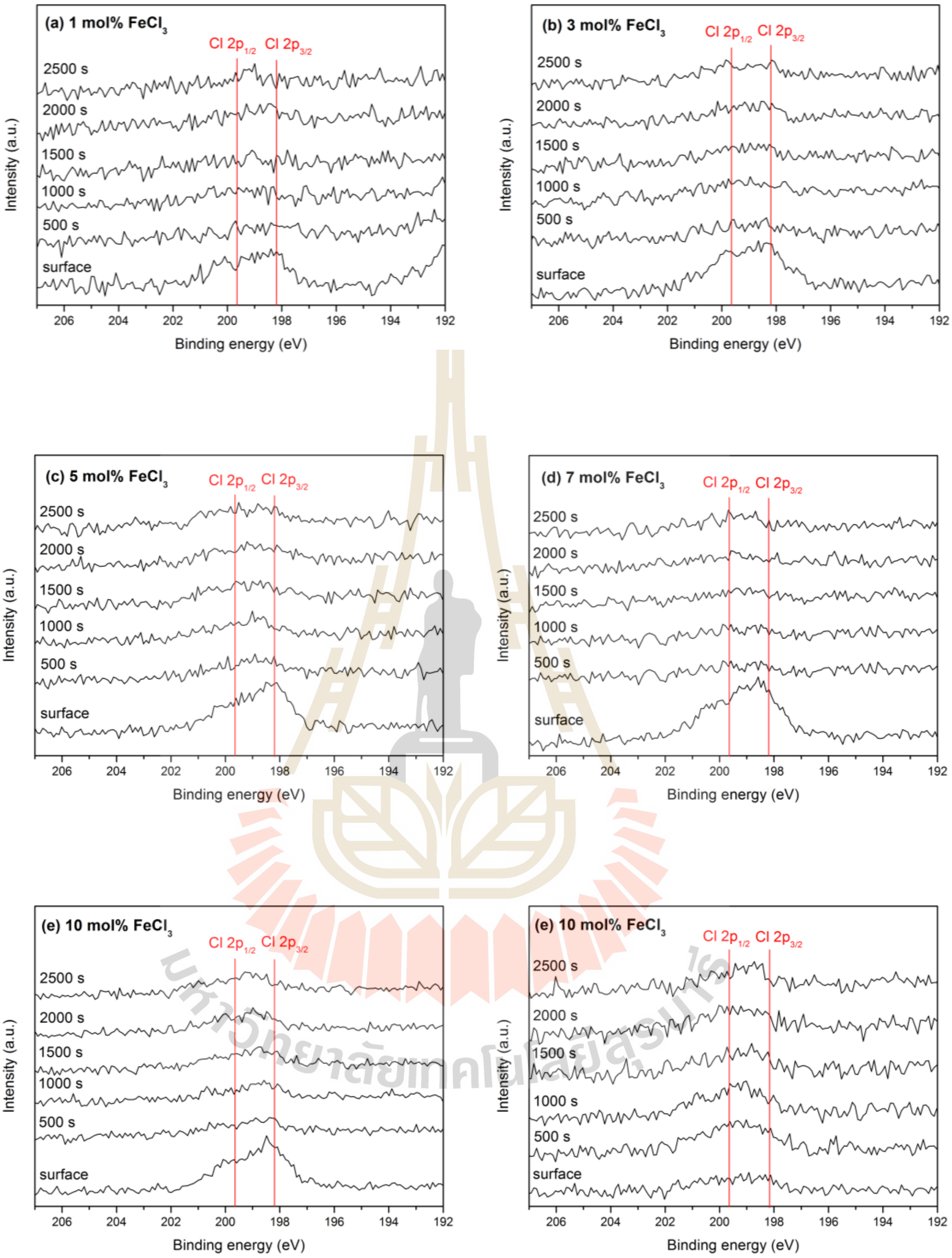

Figure A1 Surface and depth-profile Cl 2p XPS spectra of ZnO:Cl films prepared using $FeCl_3$ (a) 1 mol%, (b) 3 mol%, (c) 5 mol%, (d) 7 mol% and (e) 10 mol%.

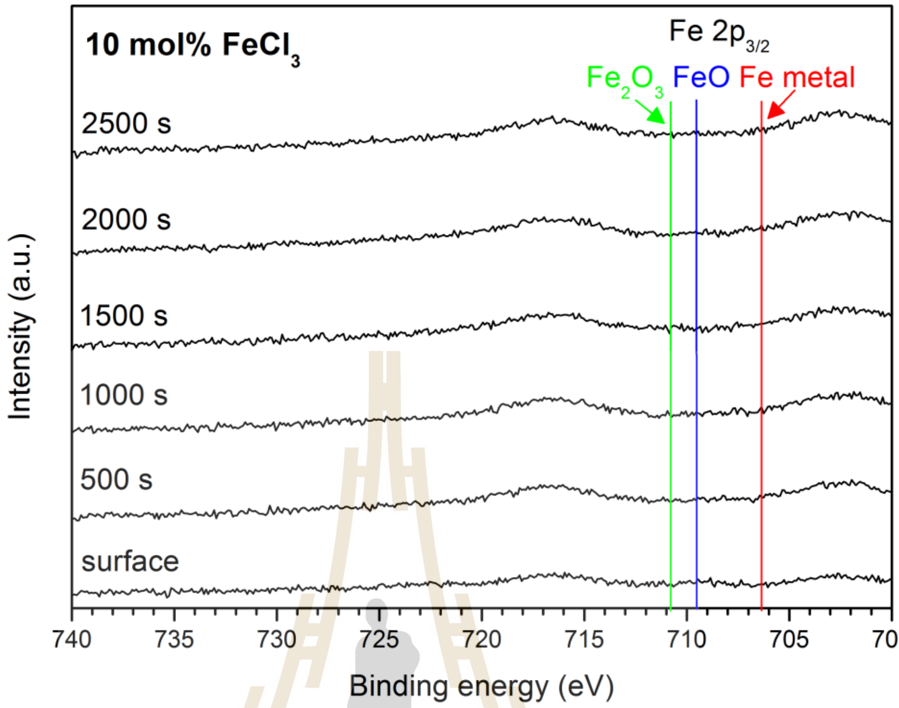

Figure A2 Surface and depth-profile Fe 2p XPS spectra of ZnO:Cl films prepared using 10 mol% $FeCl_3$. The lines refer to the expected peak position according to each form of Fe at Fe $2p_{3/2}$ region.

Table A1 at.% Cl in Cl-doped ZnO films considered at surface and in the bulk from depth profile XPS.

mol%	at.% at surface	Average at.% in the bulk	Average at.% in the whole film
1 mol%	4.32	N/A	N/A
3 mol%	3.36	0.60	1.32
5 mol%	4.61	0.63	1.30
7 mol%	3.03	0.35	0.79
10 mol%	4.47	0.84	1.45
15 mol%	12.61	1.07	2.99

APPENDIX B

STEARIC ACID DEGRADATION TEST

B1 Stearic acid degradation test

The degradation of stearic acid was determined from the change in the corrected area under FTIR absorbance spectra. The spectra in the range of 2700-3000 cm^{-1} were collected (Figure B1). Formal quantum efficiency (FQE) value is used to present the photocatalytic efficiency. In order to get the value accordingly, the linear regression of the initial 30-40% degradation steps (zero-order kinetics) was performed. A conversion factor (1 cm^{-1} $\approx$ 9.7 x 10^{15} molecule of stearic acid/cm^{2}) (Mills and Wang, 2006) was utilized to get the number of stearic acid molecule. Finally, FQE value is calculated from stearic acid molecules divided by photons.

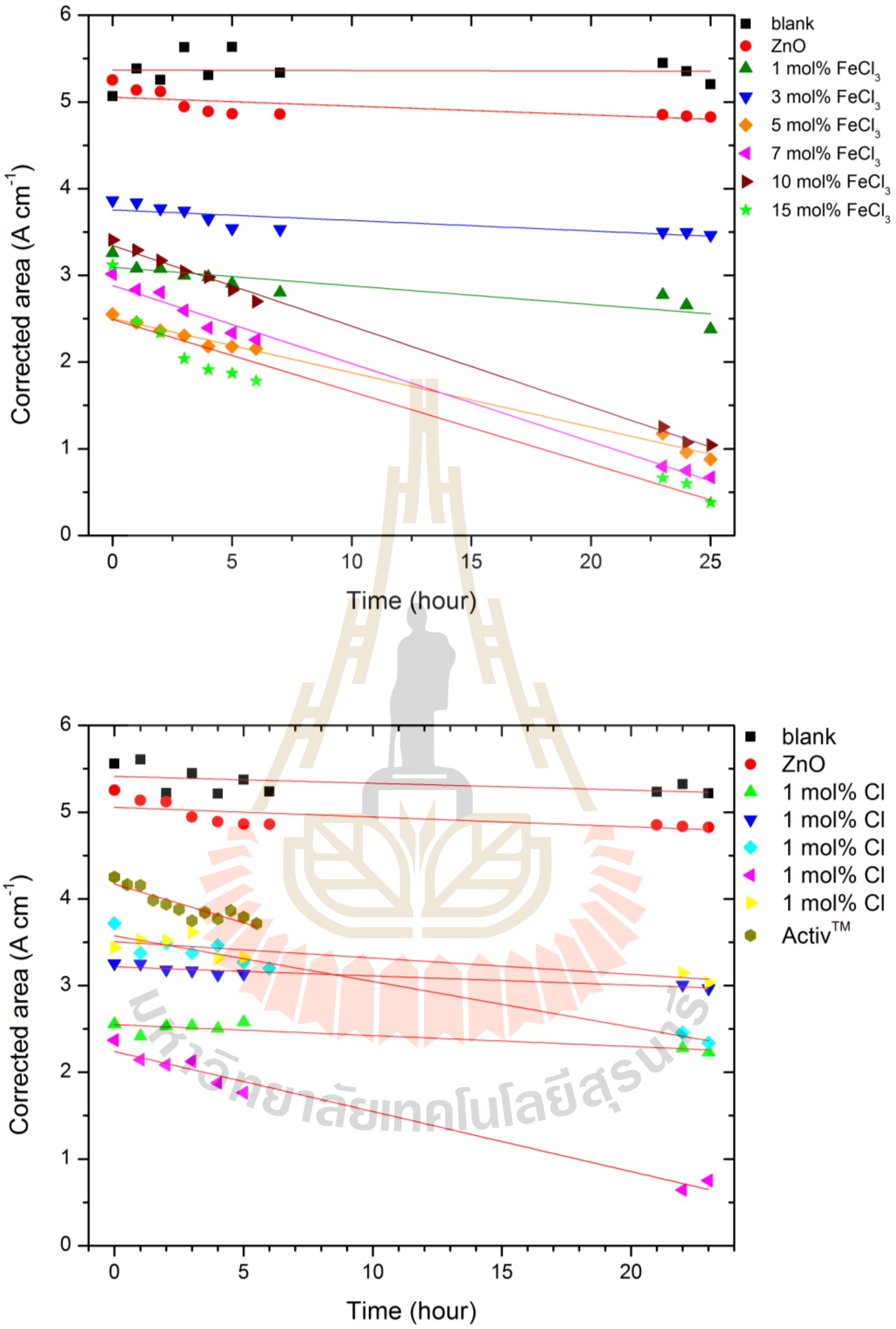

Figure B1 Plot of corrected area under FTIR spectra vs. time.

Reference

Mills, A. and Wang, J. (2006). Simultaneous monitoring of the destruction of stearic acid and generation of carbon dioxide by self-cleaning semiconductor photocatalytic films. **Journal of Photochemistry and Photobiology A: Chemistry**. 182: 181–186.

CURRICULUM VITAE

Name Miss Arreerat Jiamprasertboon **(E-mail** arreerat_j@hotmail.com)

Education

2007-2010	B.Sc. (First Class Honors) (Chemistry), Khon Kaen University
2011-2013	M.Sc. (Chemistry), Suranaree University of Technology
2014-2017	Ph.D. candidate (Chemistry), Suranaree University of Technology

Scholarship Development and Promotion of Science and Technology Talents Project (DPST)

Publications

Jiamprasertboon, A., *et al.* (2017). Investigation on Crystal Structures, Optical Properties and Band Structure Calculations of $In_{2-x}M_xTeO_6$ (M = Ga, Bi, La). **J. Alloys Compd.** 702: 601-610. (IF(2017) = 3.133)

Jiamprasertboon, A. *et al.* (2018). Photocatalytic and Electrically Conductive Transparent Cl-doped ZnO thin films *via* Aerosol Assisted Chemical Vapour Deposition. **J. Mater. Chem. A.** 6: 12682-12692. (IF(2017) = 9.931)

Awards

2017	"Structure-Property Relationships in M-doped In_2TeO_6 (M = Ga, Bi, La), Poster presentation at 16th European Conference on Solid State Chemistry, University of Strathcylde, UK (awarded a Journal of Materials Chemistry C Poster Prize)

Research experience

2017-2018	Department of Chemistry, University College London, UK (1 year)